

# Thermal Spray Coating of Carbon Reinforcement Composites for Wear and Erosion Resistance Applications

Sina Mirzai Tavana

A Thesis

In the Department

of

Mechanical Industrial and Aerospace Engineering

Presented in Partial Fulfillment of the Requirements

for the Degree of

Master of Applied Science (Mechanical Engineering)

at Concordia University

Montreal, Quebec, Canada

December 2020

© Sina Mirzai Tavana, 2020

**CONCORDIA UNIVERSITY**  
**School of Graduate Studies**

This is to certify that the thesis prepared

By: Sina Mirzai Tavana

Entitled: Thermal Spray Coating of Carbon Reinforcement Composites for Wear and Erosion  
Resistance Applications

and submitted in partial fulfilment of the requirements for the degree of

**Master of Applied Science (Mechanical Engineering)**

complies with the regulations of the University and meets the accepted standards with respect to originality and quality.

Signed by the final Examining Committee:

\_\_\_\_\_ Chair

Dr. Ali Dolatabadi

\_\_\_\_\_ Internal Examiner

Dr. Ali Dolatabadi

\_\_\_\_\_ External Examiner

Dr. Sana Jahanshahi Anbuhi

\_\_\_\_\_ Thesis Co-Supervisor

Dr. Mehdi Hojjati

\_\_\_\_\_ Thesis Co-Supervisor

Dr. Christian Moreau

Approved by: \_\_\_\_\_

Dr. Mamoun Medraj, Graduate Program Director

December 9, 2020

\_\_\_\_\_ Dr. Mourad Debbabi

Dean of Gina Cody School of Engineering & Computer Science

## ABSTRACT

### Thermal Spray Coating of Carbon Reinforcement Composites for Wear and Erosion Resistance Applications

Sina Mirzai Tavana

Polymeric composite materials have been used to manufacture both jet engine fan blades and wind turbine blades. The main considerations in the blades design are efficiency, weight, and durability. The blades must be capable of withstanding solid particles impact with no damage. Polymeric composite does not have a good erosion resistance. In this thesis, application of thermal spray coatings on polymeric composite materials has been investigated to improve their erosion resistance. Three different coating materials namely, tungsten carbide-cobalt, martensitic chromium stainless steel, and alumina-titania are chosen because of their excellent abrasion and erosion resistant, good mechanical properties, and relatively low cost. Atmospheric plasma spray is used to deposit the coating on the composite. Composite panels are manufactured using carbon fiber reinforced polymer CFRP using hand layup and autoclave curing. During the layup, a stainless steel mesh is placed on the top of the panel. This metal mesh will protect the composite during coating deposition and serve as an anchor for keeping the coating in place. Different plasma spray processing conditions are tried to have a good coating on the panel. Flatwise tensile tests are performed to measure the adhesion between the composite substrate and coating. It is found that using stainless steel metal mesh makes uniform, high quality coatings with significant adhesion property between composite substrate and coat layer. The solid erosion testing was carried out using air-jet erosion testing (ASTM G76) by hard, angular alumina particles at 30°, 60° and 90° impact angle. Different impact angles were measured to demonstrate the erosion regime (ductile or brittle) of each material. In order to determine mechanical properties and microstructure effect, roughness and the hardness of each material have been studied. It is shown that the proposed method of manufacturing can improve significantly the erosion resistance of the polymeric composites.

**Keywords:** Thermal spray coating; Plasma spraying; Carbon fiber-reinforced polymer composite; Solid particle erosion

## **Acknowledgments**

It is a great pleasure for me to acknowledge Concordia University for supporting and providing me with the opportunity to pursue my post-graduate study at this amazing university.

First and foremost, I would like to express my special thanks to Prof. Mehdi Hojjati and Prof. Christian Moreau, my wonderful supervisors, for their guidance, wisdom, feedback, and financial support during my MASc program. Without their help, this work would not have been conducted. Also my sincere gratitude and appreciation to Mr. Alireza Rahimi whose helps and aid for my project cannot be compensate in any way.

Secondly, it is a pleasure to express my thanks to all my friends in thermal spray and composite groups, Concordia research staffs, especially, Dr. Daniel Rosca, Dr. Fadhel Ben Ettouil, Dr. Navid Sharifi, Stephen Brown and Mohammadhossein Ghayour. I deeply appreciate their helpfulness and willingness in providing useful information for this study.

Lastly, I wish to express my sincere gratitude to my family for their encouragement and moral support.

# Table of Contents

List of Figures .....	vii
List of Tables .....	x
Abbreviations .....	xi
1. Introduction .....	1
1.1. Fundamentals of tribology .....	1
1.2. Wear phenomena .....	2
1.3. Solid particle erosion mechanism .....	3
1.3.1. Ductile process of SPE .....	4
1.3.2. Brittle process of SPE .....	5
1.4. Erosion resistance of different surfaces .....	9
1.4.1. Erosion behavior of cermets .....	10
1.4.2. Erosion behavior of ceramic oxides .....	12
1.4.3. Erosion behavior of iron-base alloys .....	14
1.4.4. Erosion behavior of polymer matrix composites (PMC) .....	16
1.5. Thermal spray processes and surface engineering .....	18
1.5.1. Surface preparation .....	19
1.5.2. Cold spraying .....	22
1.5.3. Arc spraying .....	23
1.5.4. Plasma spraying .....	25
1.6. Objectives .....	27
2. Experimental method .....	29
2.1. Substrate fabrication .....	29
2.2. Substrate preparation .....	33

2.3. Coating process of composites .....	35
2.4. Image analysis and coating characterization .....	40
2.5. Solid particle erosion testing .....	41
2.6. Vickers hardness testing .....	43
2.7. Adhesion strength testing .....	45
3. Results and discussion.....	47
3.1. Analysis of CFRP substrate structure with wire mesh.....	48
3.2. Grit blasting operation .....	48
3.3. Microstructural characterization of plasma spraying coatings .....	51
3.3.1. Analysis of tungsten carbide 20 wt. % cobalt APS coating.....	51
3.3.2. Analysis of martensitic stainless steel APS coating .....	53
3.3.3. Analysis of alumina 3 wt. % titania APS coating.....	55
3.4. Solid particle erosion resistance of the different coatings and CFRP .....	57
3.4.1. Investigation of tungsten carbide 20 wt. % cobalt erosion mechanism.....	58
3.4.2. Investigation of martensitic stainless steel erosion mechanism.....	60
3.4.3. Investigation of alumina 3 wt. % titania erosion mechanism .....	62
3.4.4. Investigation of CFRP erosion mechanism.....	64
3.4.5. Comparison between the erosion resistance of different substrates .....	66
3.5. Results of hardness measurements .....	69
3.6. Adhesion strength.....	70
4. Conclusions, contributions, and future work .....	73
4.1. Conclusions and contributions.....	73
4.2. Future work.....	75
References .....	76

## List of Figures

<b>Figure 1.1:</b> Typical SPE behavior for ductile and brittle materials .....	4
<b>Figure 1.2:</b> Proposed mechanisms explaining the ductile behavior of materials.....	5
<b>Figure 1.3:</b> Models of fractures during indentation of brittle surfaces .....	6
<b>Figure 1.4:</b> Structure deformation; Al <sub>2</sub> O <sub>3</sub> erodent particles at an impact angle of 90°; (a) 30 m/s and (b) 64 m/s .....	6
<b>Figure 1.5:</b> Schematic representation of lateral cracking following solid particle impact .....	8
<b>Figure 1.6:</b> Designation of each grade based on the WC grain size .....	11
<b>Figure 1.7:</b> Mechanical performance of different graded cemented carbides. Left: hardness v.s. wt%Co; right: fracture toughness v.s. wt%Co.....	12
<b>Figure 1.8:</b> Fracture surface of alumina with (a) 0.2 wt. % and (b) 4.0 wt. % TiO <sub>2</sub> sintered at 1400 °C.....	13
<b>Figure 1.9:</b> Vickers hardness of different TiO <sub>2</sub> added to Al <sub>2</sub> O <sub>3</sub> samples sintered at 1600 °C.....	14
<b>Fig. 1.10:</b> Silicon carbide (SiC) erosion test at (30°, 45°, 60°, 90°) angles on 304,316 (austenitic) stainless steels and, 420(martensitic) stainless steel.....	15
<b>Figure1.11:</b> Schematic diagrams of the erosive process in unidirectional fiber-reinforced composites under (a) parallel and (b) perpendicular impact conditions .....	17
<b>Figure 1.12:</b> Schematic diagram of a thermal spray process .....	19
<b>Figure 1.13:</b> SEM image of a glass fiber-reinforced polymer GFRP substrate after Al <sub>2</sub> O <sub>3</sub> grit blasting for (a) 2, (b) 4, (c) 6 seconds .....	21
<b>Figure 1.14:</b> SEM images (a and b) and cross-section optical micrographs (c and d) of the CFRP after cold spray of spherical Cu powder (the bright particles in c are copper, and the clusters of bright dots in c and d are the carbon fibers perpendicular to the observation plane) .....	23
<b>Figure 1.15:</b> Schematic wire arc spraying process.....	24
<b>Figure 1.16:</b> Schematic of a plasma spray torch .....	25

<b>Figure 1.17:</b> Cross-sectional SEM images of the coating (bond coating and top coating), (a) coating on the PMC, (b) coating separated from PMC.....	27
<b>Figure 2.1:</b> Microscopic images of the 200-mesh stainless steel cloth.....	30
<b>Figure 2.2:</b> Schematic of a typical vacuum bagging lay-up.....	31
<b>Figure 2.3:</b> Recommended heating cycle for curing CYCOM® 977-2 prepregs .....	32
<b>Figure 2.4:</b> (a) 200 mesh plate in oven (b) 200 mesh plate in autoclave .....	33
<b>Figure 2.5:</b> (a) The structure of a 3MB plasma spray gun (b) feed injector 90° angle .....	36
<b>Figure 2.6:</b> Plasma spray process equipment.....	39
<b>Figure 2.7:</b> Samples after (A) WC20Co coating (B) Al <sub>2</sub> O <sub>3</sub> TiO <sub>2</sub> coating (C) Martensitic stainless steel coating .....	39
<b>Figure 2.8:</b> (a) SPE testing chamber with windows and a HEPA filter. (b) Sample and nozzle holder for SPE testing with retractable shutter .....	41
<b>Figure 2.9:</b> Wear scars from A) uncoated composite B) WC20Co coating, C) Martensitic stainless steel coating, D) Al <sub>2</sub> O <sub>3</sub> TiO <sub>2</sub> coating, eroded at 30° angle after 10 min. ....	43
<b>Figure 2.10:</b> a schematic diagram of the erosion rig.....	43
<b>Figure 2.11:</b> Geometrical description of a Vickers type indenter .....	44
<b>Figure 2.12:</b> Flatwise tensile test (a) sample alignment, (b) test equipment.....	46
<b>Figure 3.1:</b> 200 mesh substrate cross-section with a 5x and 20x magnification.....	48
<b>Figure 3.2:</b> Confocal images of a grit-blasted 200 mesh substrate (P= 42 psi and t= 150 s).....	50
<b>Figure 3.3:</b> Confocal images of a grit-blasted 200 mesh substrate (P= 73 psi and t= 150 s).....	50
<b>Figure 3.4:</b> Confocal images of a grit-blasted 200 mesh substrate (P= 53 psi and t= 150 s).....	50
<b>Figure 3.5:</b> Different types of coating failure a) the steel cloth and coating peeled off, b) cracking if the coating layer, c) entire destruction of the coating and steel mesh layer .....	52
<b>Figure 3.6:</b> Cross-section of WC20Co coating on a PMC sample a) optical image at low magnification b) SEM image at high magnification.....	53
<b>Figure 3.7:</b> Cross section images of a WC20Co coating sprayed on a) composite with metal mesh b) grit-blasted mild steel sample.....	53



<b>Figure 3.8:</b> Cross-sections of stainless steel coatings on composite substrate with (a) optical image at low magnification and (c) optical image at high magnification (b) SEM image at high magnification. (d) on grit-blasted mild steel sample .....	55
<b>Figure 3.9:</b> Cross-section of $Al_2O_3/3TiO_2$ coating on composite substrate with (a) low magnification and (b) high magnification (c) SEM image of the coating on a composite mesh sample (d) grit-blasted mild steel sample after coating at high magnification .....	57
<b>Figure 3.10:</b> Mass loss of CFRP samples coated with WC20Co tested at (a) $30^\circ$ and (b) $60^\circ$ ....	59
<b>Figure 3.11:</b> (a) Mass loss of CFRP samples coated with WC20Co tested at $90^\circ$ and (b) Erosion rate of WC20Co samples as a function of impingement angle.....	60
<b>Figure 3.12:</b> Mass loss of CFRP samples coated with martensitic stainless steel tested at (a) $30^\circ$ and (b) $60^\circ$ .....	61
<b>Figure 3.13:</b> (a) Mass loss of CFRP samples coated with martensitic stainless steel tested at $90^\circ$ and (b) Erosion rate of martensitic stainless steel samples as a function of impingement angle .....	62
<b>Figure 3.14:</b> Mass loss of CFRP samples coated with alumina 3 wt. % titania tested at (a) $30^\circ$ and (b) $60^\circ$ .....	63
<b>Figure 3.15:</b> (a) Mass loss of CFRP samples coated with alumina 3 wt. % titania tested at $90^\circ$ and (b) Erosion rate of alumina 3 wt. % titania samples as a function of the impingement angle. ....	64
<b>Figure 3.16:</b> Schematic diagram of the composite sample in perpendicular CFs orientation in the erosive wear tests .....	65
<b>Figure 3.17:</b> Mass loss of unidirectional CF/Epoxy samples tested at (a) $30^\circ$ and (b) $60^\circ$ (c) $90^\circ$ (d) Erosion rate of CF/Epoxy samples as a function of impingement angle .....	65
<b>Figure 3.18:</b> Erosion rates (mg/g) of test samples as a function of the impingement angle .....	68
<b>Figure 3.19:</b> Volumetric erosion rates ( $mm^3/g$ ) of test samples as a function of the impingement angle .....	69
<b>Figure 3.20:</b> Adhesion strength results of the coated samples .....	71

**Figure 3.21:** Failure mechanism of the coated samples, left) substrate failure, right) (a) adhesive failure (b) adhesive and cohesive combination..... 72

## List of Tables

**Table 2.1:** 200-mesh stainless steel cloth properties ..... 30

**Table 2.2:** Grit blasting parameters used for roughening the samples. .... 34

**Table 2.3:** Chemical composition and particle size distribution of the Metco 76F-NS powder (labelled WC20Co) ..... 36

**Table 2.4:** Chemical composition and particle size distribution of the Diamalloy 1002 powder 36

**Table 2.5:** Chemical composition and particle size distribution of the Metco 101NS powder (labelled Al<sub>2</sub>O<sub>3</sub>-TiO<sub>2</sub>)..... 37

**Table 2.6:** Grit blasting parameters used for the surface preparation. .... 37

**Table 2.7:** The plasma spray parameters used for the coating of the PMC substrates..... 38

**Table 3.1:** Surface free energy of different materials ..... 47

**Table 3.2:** Results of micro-hardness measurement of different samples..... 70

## Abbreviations

A	Cross-sectional area
APS	Atmospheric plasma spray
AS	Arc spray
CFRP	Carbon fiber reinforced polymer
E	Erosion rate
PMC	Polymer matrix composite
WC	Tungestan carbide
T	Time

## **1. Introduction**

Application of polymer matrix composites (PMC), and in particular carbon fiber reinforcement composites, in large variety of advanced engineering structures such as aero engines of airplanes and wind turbine blades has become an ongoing trend nowadays [1]. Many metallic parts are replaced by PMC to reduce the weight. However, polymer composites suffer from their poor erosion resistance when they are subjected to wind airborne particles like sand, dust, and volcanic ashes [2-3]. These abrasive particles impose momentum and energy transfers, which may damage the surface of the composites in significant ways. It is well established that the impingement of solid particles can cause unnecessary operation cost and early breakdown. Many different methods have been proposed to provide good damping effects and sufficient protection for PMCs during their whole lifetime. The purpose of this work is to develop an appropriate composite material structure with good tribological performance and high strength. (resistance against solid particle erosion). In advanced industrial structure, surface engineering is a proper way to introduce extra protection and effectively reduce the erosive wear. However, composites are limited to a low-temperature operation, which creates major challenges in surface modification and coating deposition on composite materials, and because of the impact of high-velocity particles to their vulnerable surface, only a few conventional methods are suitable to achieve high-performance surface metallization for PMCs. In this context, the viability and possible mechanism of the atmospheric plasma spray coating process and the right feedstock material between three wear resistance powders will be discussed, with respect to prior research [4].

### **1.1. Fundamentals of tribology**

The word tribology emphasizes the scientific study of relative motion between surfaces, which involves three different categories: friction, lubrication, and wear. Friction relates to the actual force opposing the movement of two surfaces in contact against each other. Lubrication is a process of easing the interaction of two moving surfaces by minimizing the friction. In the past, the formal definition of wear was a loss and removal process occurring by one surface by mechanical interaction with an opposing surface. Tribology processes cause property and geometrical changes in the surface of the moving materials. Many material and energy parameters affect these transformations in both surfaces, such as chemical composition, elasticity, shear strength of the

materials, normal load, velocity, tangential force and temperature. These parameters cause changes in the outcome of this tribological contact. These outcomes are friction, wear, velocity, temperature, sound, and dynamic behavior. A useable and successful approach to design a structure with multi-scale properties is to use an extra coating layer designed for the specific tribological and wear conditions, which improve the functional reliability and lifetime of different substrates [5].

## **1.2. Wear phenomena**

It is important to understand the phenomena of the wear concept and its mechanism. Nowadays, wear property does not necessarily apply to the removal of material from a surface in relative motion, but it refers to a mechanical act on a protected surface. Regarding corrosion, corrosive wear describes a mechanical interaction in a corrosive environment, not corrosion itself [6]. Wear, by another definition, is the destruction of the material structure, most likely at the surface or close to it. This description comprises much different material behavior such as plastic deformation, brittle fracture, fatigue, and adhesive and cohesive failures of bonding structure in the concept of wear mechanism. There is no general model or classification to categorize different mechanisms of wear, but in industrial applications, some of these mechanisms are frequently noticed. One of the common mechanisms in wear degradation is adhesive and cohesive wear, which indicates the material removal of each moving surface at when they are in contact and adhered to each other. Depending on how many cycles this motion happens, each surface may present various mechanical damage and deformation. Abrasive wear or abrasion is one of the other mechanisms which is based on forming several types of damage like grooving or scratching by sliding hard and rigid particles or a hard surface on a soft one. Debris can be generated from the contacting surfaces, which creates a three-body abrasion condition. In the case involving only the two surfaces, the wear is named two-body abrasion. The third type of wear is erosion, and it takes place when in-flight particles impact the surface of the material. The particles can be entrained by a flow of fluid or gas. Several parameters like velocity, impinging angles, time, shape and properties of the impacting particles are important on how the surface resists against the wear mechanism [7].

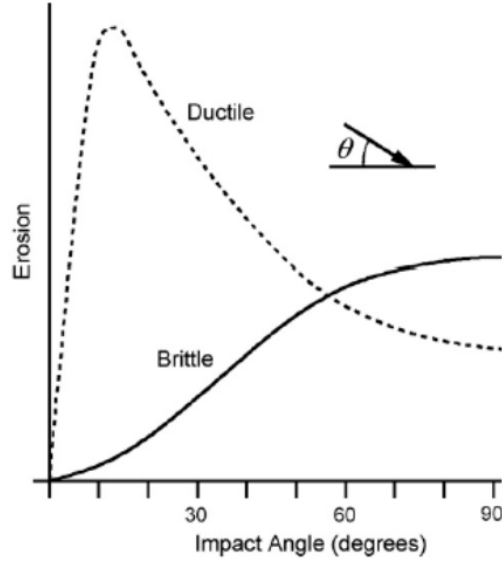
### **1.3. Solid particle erosion mechanism**

The solid particle erosion (SPE) test is a process that simulates the environmental condition for industrial parts and engines by propelling particles towards a surface and analyzing the failure mechanism and durability of the surface material. SPE experiment exists in four ways:

- 1) Solid particle erosion
- 2) Liquid impingement erosion
- 3) Hot gas erosion
- 4) Cavitation erosion

In each of these processes, the particles impact the surface with a different approach such as impact or cavitation, and in different flow phases like solid or liquid, which eventually cause material loss, surface deformation, or other changes in the appearance. In SPE, a nozzle ejects the particles with a high-speed gas or liquid flow. When the particles reach the target and hit the surface, their kinetic energy (KE) can alter the microstructure and properties of the material in a variety of mechanisms like heating, ductile deformation or fracturing. There are many factors involve in how the mechanisms and deformation occur, but overall they can be categorized according to characteristics of the particles (composition, shape, size, hardness), specimen characteristics (roughness, hardness, porosity, damping property, etc.), and test condition (particle flux, velocity (average), test duration, carrier gas composition, pressure, and temperature).

In SPE, like any other tests, when an object hits the surface, the impact angle determines in which way the material is going to deform and make a scar. Two types of erosion processes are used to indicate the material resistance against particle impingement: ductile and brittle. For better resistance against SPE, the substrate must exhibit ductile behavior at a high angle in which particles impact perpendicular to the surface, and on the contrary, the brittle behavior is needed when the angle is reduced and close to 20-40 degrees (Figure 1.1). The type of surface deformation in the ductile SPE mechanism is ploughing or cutting, and in the brittle mechanism, the stress of impact can cause the initiation and growth of multiple crack on the substrate surface.



**Figure 1.1:** Typical SPE behavior for ductile and brittle materials [8]

### 1.3.1. Ductile process of SPE

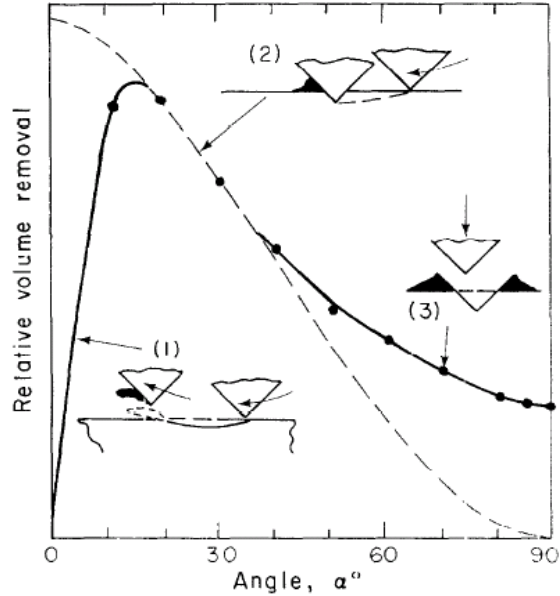
In general, the erosion rate is related to the kinetic energy of the impacting particles, which is proportional to the square of the velocity of the particles. Several research studies have been done to demonstrate the behavior of SPE at high angles. Among them, Finnie discovered many variable parameters interference in SPE, like interaction energy of the solid particles and the target surface. Considering the plastic characteristics of the materials, he reported that the volume removed ( $V_e$ ) by the impacting particles calculated from the following equations is close to experimental observations:

$$V_e = \frac{m_p V_p^2}{\sigma_y \chi K} \left( \sin 2\theta - \frac{6}{K} \sin^2 \theta \right) \text{ If } \tan \theta < \frac{K}{6} \quad (1.1)$$

$$V_e = \frac{m_p V_p^2}{\sigma_y \chi K} \left( \frac{K}{6} \cos^2 \theta \right) \text{ If } \tan \theta > \frac{K}{6} \quad (1.2)$$

Where  $\theta$  is the angle of incidence,  $m_p$  is the particle mass,  $V_p$  is the particle velocity,  $K$  is the ratio of the vertical and horizontal forces applied to the particle tip, and  $\chi$  is the ratio between the length and width of the cut. These formulas calculate the material removal using the particle force when they impact the surface [9]. In another study, Finnie's model was used to demonstrate the good fit between the calculated volume lost relative to experimental data at angles up to near  $45^\circ$ . This is

shown in Figure 2.11 where curves 1 & 2 show the modeled behavior, and curve 3 presents the typical experimental observations. The model predicted the behavior of the SPE very similar to maximum erosion rate ( $ER$ ) at cutting without particle immobilization and ploughing [10].

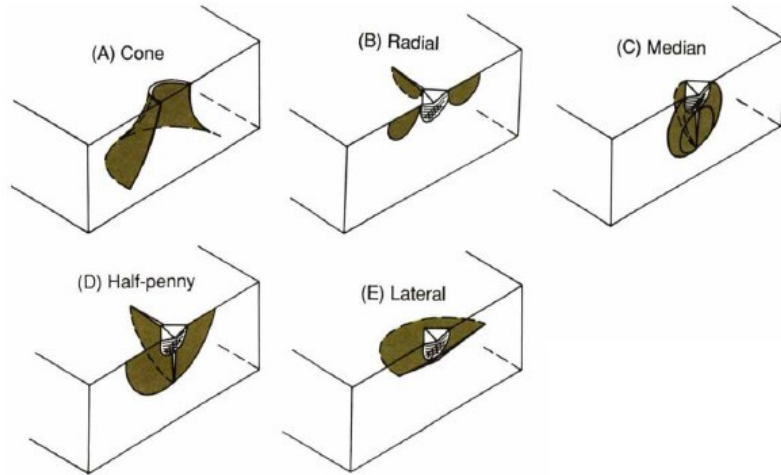


**Figure 1.2:** Proposed mechanisms explaining the ductile behavior of materials [10]

### 1.3.2. Brittle process of SPE

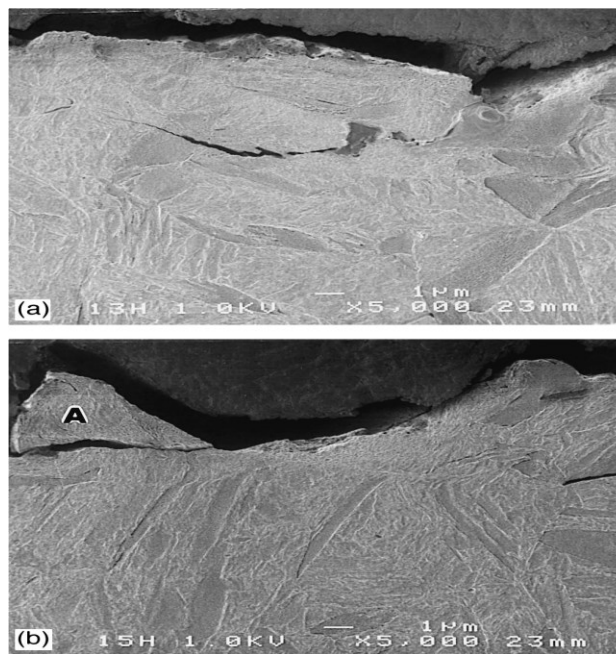
In the SPE process, particles approach the surface at different angles and speed and cause various types of damage. Others have indicated that the minimum erosion rate in materials with brittle property occurs at low angles and oblique impact [11]. The wear mechanism is originated by crack initiation and propagation and the progressive behavior of surface flaws towards each other. SPE process is carried out by particles with different characteristics (particle density, particle shape, particle size), which influence the process of surface chipping, the deformation construction, and crack formation as illustrated in Figure 1.3 [11]. Upon impact of large spherical particles, high tensile stress is applied on the surface and creates elastic deformation. In this case, crack propagation of the material initiates with surface flaws linking to each other and form circular cracks (Figure 1.3 (A)). On the contrary, small particles with high velocity deform the surface in a sharp pyramidal shape, which is frequently observed in brittle material structures (Figure 1.3 (B) to (E)).





**Figure 1.3:** Models of fractures during indentation of brittle surfaces [11]

Upon impact of small particles, plastic deformation continues until its maximum range penetration and makes median, and radial cracking (Figure 1.3 B and C), and aggregation of these cracks form half-penny cracking (Figure 1.3 D). Beneath any types of cracking, strain mismatch deforms the material structure and misshape it plastically and elastically in order to relax (Figure 1.4) [11].



**Figure 1.4:** Structure deformation;  $\text{Al}_2\text{O}_3$  erodent particles at an impact angle of  $90^\circ$ ; (a) 30 m/s and (b) 64 m/s [11].

In 1966, Finnie subsequently expanded his theories for brittle materials and assumed the erosion happens only due to crack propagation and chipping. He and Sheldon [12] suggested the preexisting flaws in the material help cracks to form and propagate and cause erosion, which they called Weibull statistics. Their research resulted in finding a relation between the influenced factors and the predicted erosion rate (Eq.3.1):

$$W = K_1 r^a V^b \quad (1.3)$$

where the exponents  $a$  and  $b$  are given by:

$$a = 3(m-0.67)/(m-2) \quad \text{for round particles}$$

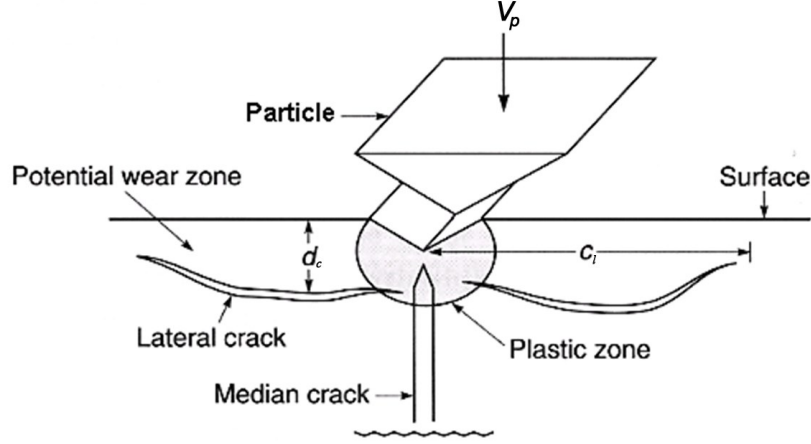
$$a = 3.6(m-0.67)/(m-2) \quad \text{for angular particles}$$

$$b = 3(m-0.67)/(m-2) \quad \text{for either shape}$$

and  $r$ ,  $V$ ,  $m$  and  $K_1$  are the particle size, particle velocity, Weibull constant, and material's fracture toughness (in tensile crack opening mode), respectively [12].

They observed that the experimental data fit well the theoretical results for different brittle materials (glass, MgO, Al<sub>2</sub>O<sub>3</sub>, graphite). However, on a physical basis, their assumption about, Hertzian crack formation being the main reason for material removal, was not accurate.

Wiederhorn and Lawn (1979) proposed a more developed theory that showed the elastic-plastic effects on erosion behavior of brittle material. Proportionating the lateral crack size to the radial crack size was one of the assumptions, and the depth of the lateral cracks is related to the maximum particle penetration was another assumption of this theory. Lawn realized that the radial crack length was proportional to lateral crack lengths, and Wiederhorn benefited from this theory to measure the lateral crack length and afterward the cylindrical volume loss caused by a single sharp particle impact. In elastic-plastic theories, the hardness and toughness of the target can alter the erosion rate, and it was presumed that velocity and particle size are not related to target and particle properties [12].



**Figure 1.5:** Schematic representation of lateral cracking following solid particle impact, adapted from [8]

In Figure 1.5, the elastic-plastic behavior was simulated as a quasi-static indentation process to demonstrate the formation of the lateral fracture in the target surface, which was a result of the plastic deformation caused by particle impact. To measure the cylindrical volume loss of the target, penetration of the particle should be calculated by:

$$W = \int_0^{Z^m} P(z) dz \quad (1.4)$$

where  $P$  is the load of the impacting particle, and  $Z$  is the depth of penetration.

In order to show the hardness in the indentation process, the load should be applied as a mean contact pressure:

$$P_0 = H = \frac{P}{A(z)} \quad (1.5)$$

where  $A(z)$  is the penetration area of the particle on the impacted surface.

For better estimation, particle shape was assumed to be angular, and its cone will be measured by:

$$A(z) = \pi z^2 \tan^2 \psi \quad (1.6)$$

where  $\psi$  is the cone half-angle. The combination of these three equations 1.4, 1.5, and 1.6 and integrating:

$$Z_m = \left( \frac{3*KE}{H\pi \tan \psi^2} \right)^{\frac{1}{3}} \quad (1.7)$$

and

$$P_m = H \pi \tan \psi^2 \cdot Z_m^2 \quad (1.8)$$

Using

$$KE = \frac{1}{2} m_p V_p^2 \propto D^3 \rho_p V_p^2 \quad (1.9)$$

Through understanding the role of all these factors and their effects, volume loss in elasto-plastic indentation Wiederhorn theory expressed by (the effects of all these parameters are going to be assessed in coming chapters):

$$V_e \propto V_p^{22/9} D^{11/3} \rho_p^{11/9} H^{1/9} K_{IC}^{-4/3} \quad (1.10)$$

#### 1.4. Erosion resistance of different surfaces

Around the world, the erosion phenomena occur on a large range of scales, whether on the moving rocks in the Amazon River or on the blades of airplane engine turbines, and this action mainly depends on two considerable factors. The first one is related to how hard and significant the erodent impact with the material and wrecks its structure. As an example, the force impact of droplets in the tranquil water pipe in houses or collision of heavy rocks in moving and dynamic water of a huge river. The second factor clearly depends on the resistance of the material itself having a brittle or hard behavior when they undergo the same erosional force. Some materials are resistant against erosion, which makes them desirable for manufacturing different structures or, in some cases, can be employed as an extra protective layer. Over hundreds of materials were tested by sand-blast erosive type procedure to demonstrate their erosion resistance. Most metals have low erosion resistances, and most likely, they are combined with each other as alloys like nickel or iron base alloys to show a higher property. Ceramics such as boron carbide (B4C), tungsten carbide

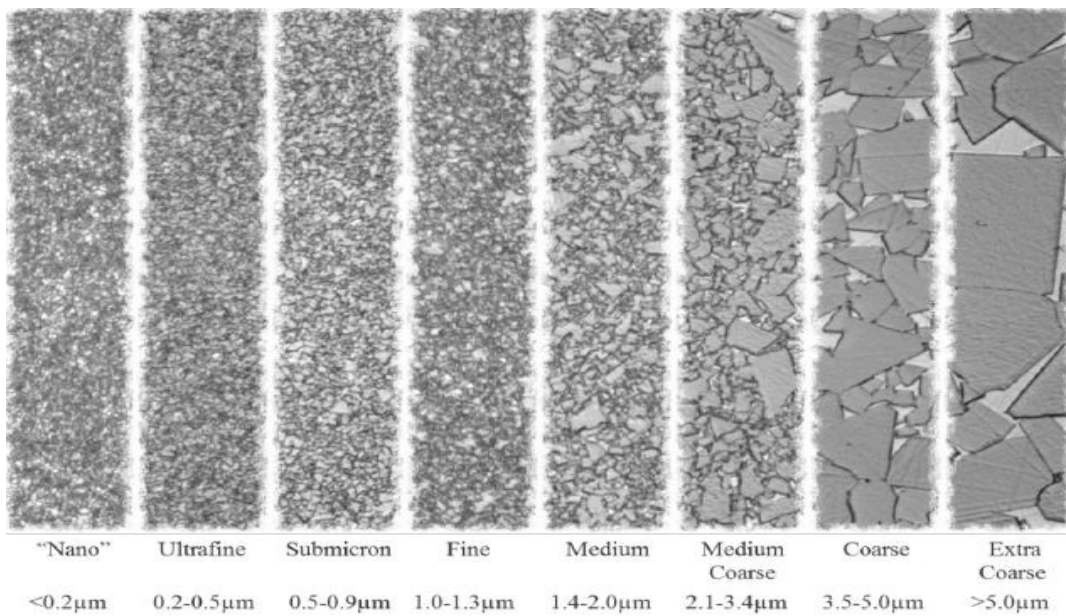
(WC), silicon carbide (SiC), silicon nitride (Si<sub>3</sub>N<sub>4</sub>), and titanium diboride (TiB<sub>2</sub>) with a low porosity structure, have higher erosion resistance more than four times compared to metals [13].

#### **1.4.1. Erosion behavior of cermets**

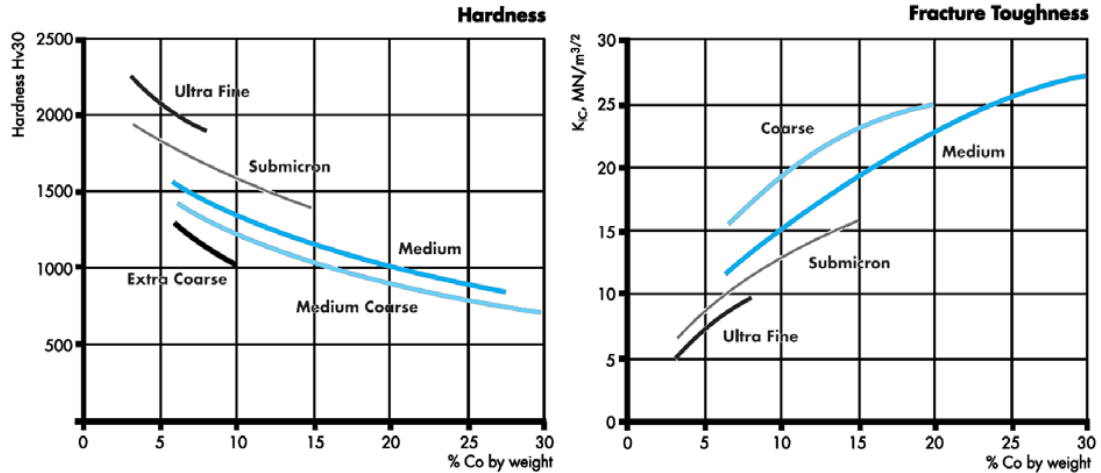
Structures of cermets (ceramic (cer) and metal (met)) are the combination of hard phase ceramics and metal or alloys. These composite materials combine two main preference of ceramics, high-temperature performance and wear resistance with the toughness, flexibility, plastic deformation, or electrical conductivity of a metal. In this type of composites, metal components are used as a binder for oxide, boride or carbide particles. The metal components generally are nickel, cobalt or molybdenum. The cermets contain several characteristics in their structure. The wettability between ceramics and metals is convincing, and this provides a continuous phase structure and greater properties in cermets. No chemical reaction occurs between the metal and ceramic phase, which indicates, there is no intense reaction at the interface between the two phases and this makes them more resistant to mechanical shock and thermal shock. The expansion coefficients of the two parts are similar to each other; therefore, the internal stress produced in any application is limited providing a greater thermal stability of the cermets. Cermets are classified into various categories like oxide-based, carbide-based, titanium nitride-based, and boride cermets. In carbide-based cermet, titanium carbide, silicon carbide, tungsten carbide are included in the metal matrix. On the other hand, cobalt, nickel, chromium, tungsten and molybdenum are chosen metals.

Every day, so many metal materials are massively used for different corrosion-erosion applications. However, among all those compounds, tungsten carbide is one of the few with properties like resistance to heat, rust, scratches, and pitting. Furthermore, merging the elements carbon and tungsten creates incredible hardness and resistance to wear and tear property in their structure and makes them a suitable material for cutting tools, mining bits, sandblasting nozzles, and for a variety of other wear-resistant applications. Cobalt is usually chosen as a tough metal binder phase. They have demonstrated outstanding wetting, adhesion properties with low corrosion resistance, which is vital for WCCo to become a desirable cermet [14]. In order to undermine the low corrosion property of the cobalt, Ni has been used as an alternative binder, and because of its FCC structure, WC-Ni has shown higher wear resistance. In comparison in hardness and strength, WC-Co is always the first choice. Occasionally, Fe is being applied as a binder in WC-based

composites, and its hardness and toughness properties are comparable to WCCo. However, the poor corrosion resistance of Fe is still a setback in this type of cermet. Also, Fe has high attachment towards carbon, which provides higher hardness in the structure. However, it can result in the formation of  $\eta$  phase (M<sub>6</sub>C) [15,16]. The value of the grain size and Co content modify the mechanical properties of the WCCo. Reducing the WC grain size can improve the hardness, compressive strength, and bending strength, of the cermet. However a reduction in WC grain size can reduce the impact strength, rupture strength, and fracture toughness (Figure 1.6). By increasing cobalt content, WCCo's hardness, the modulus of elasticity (Young's Modulus), and compressive strength decrease, but it helps with increasing strength and fracture toughness due to increasing the ductile phase of the structure (Figure 1.7) [17,18].



**Figure 1.6:** Designation of each grade based on the WC grain size [19]



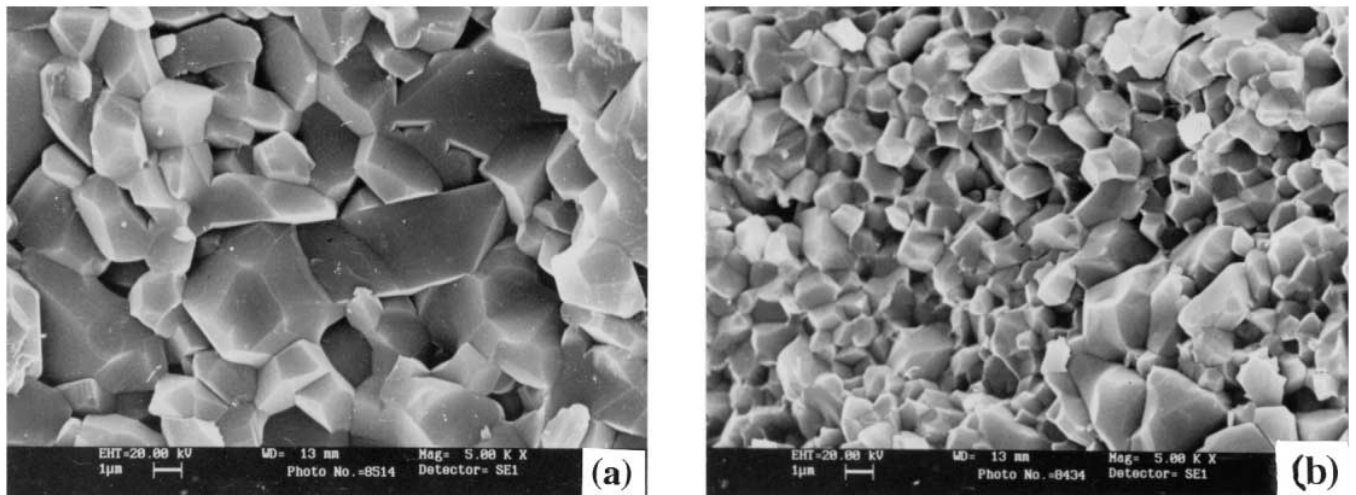
**Figure 1.7:** Mechanical performance of different graded cemented carbides. Left: hardness v.s. wt%Co; right: fracture toughness v.s. wt%Co [19]

### 1.4.2. Erosion behavior of ceramic oxides

Ceramics are known to be inorganic, nonmetallic solids used in industrial applications. They are made up of metal oxides (a combination of metallic elements and oxygen). This composition provides various universally recognized ceramic-like properties, including high hardness and strength (in spite of their brittleness), chemical reactivity resistance against both effects of oxygen and other chemicals like acids or organic solvents, considerable durability and wear resistance, low electrical conductivity and being a good insulator. One of the major issues in ceramic materials is their brittleness, and for better utilization, comprehension of flaw size and the fracture toughness of their structure is in order. In fact, for superior fracture toughness, the size and the number of the exciting flaws in the compound's microstructure is vital, and since the grain boundary inside the ceramics is considered to be a flaw and also many surface flaws are constructed during their application process, they are asserted to be brittle with low fracture toughness [20]. Grain size is another effective factor in assessing the wear property of ceramics. The erosion resistance of this class of materials is substantially reduced in the case of smaller grains in comparison to the size of the destruction created by the particle impact. Having said that, chipping grain ejection happens when the grain size is larger than impact damage. [21,22].

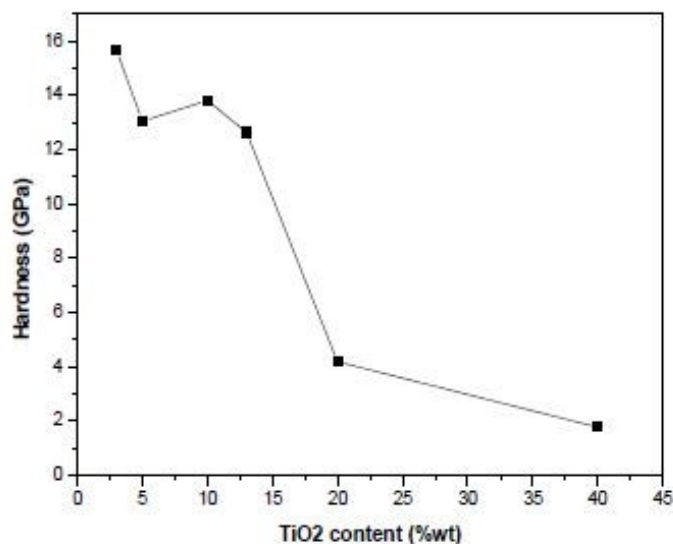
Industrial ceramics have proven to be an effective compound for achieving better mechanical and high-temperature properties of components and equipment performance. In fact, a layer of

ceramics on the top surface of different industrial parts enhance their wear resistance, high-temperature protection, and corrosion protection. There are large variety of ceramic materials that are able to fabricate these advantages, such as  $\text{Cr}_2\text{O}_3$ ,  $\text{Al}_2\text{O}_3$ , and  $\text{ZrO}_2$ . Each of these materials offers unique advantages, and among them, aluminum oxide provides high dielectric performance (using nearly-pure  $\text{AlO}_3$ ) as well as high corrosion or wear resistance property (using titanium oxide additives). Adding  $\text{TiO}_2$  changes the mechanical properties of alumina and improves flexural strength and Vickers hardness. However, the titania concentration determines the extent of the properties improvements. In sintered samples, the grain size of alumina decreases by enhancing the  $\text{TiO}_2$  content, and after a certain point large amount of secondary phase reduces the grain growth and flexural strength (Figure 1.8) [23]. According to previous research, 3% of  $\text{TiO}_2$  creates a structure with the highest flexural strength and Vickers hardness (in the presence of  $\text{Al}_2\text{TiO}_5$  phase) (Figure 1.9) [24].



**Figure 1.8:** Fracture surface of alumina with (a) 0.2 wt. % and (b) 4.0 wt. %  $\text{TiO}_2$  sintered at 1400 °C [23]






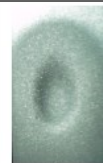
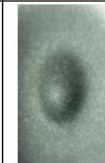
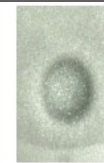


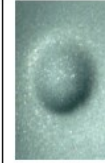





**Figure 1.9:** Vickers hardness of different TiO<sub>2</sub> added to Al<sub>2</sub>O<sub>3</sub> samples sintered at 1600 °C [24]

### 1.4.3. Erosion behavior of iron-base alloys

Another group of wear resistance materials is iron-based alloys. In the world, cast iron is known as a brittle material due to containing carbon (about 4-wt- %) in its structure. The carbon content of cast iron can be reduced if oxygen is blown into molten iron (fresh from the blast iron), which creates wrought iron. Wrought iron is the purest form of iron. It is soft and malleable, and it does not exhibit noticeable performance in industrial applications as much as iron Alloys. There are several different types of iron-based alloys around the world with variable properties making them suitable for different applications such as heat resistance, corrosion, and wear resistance.

Steel is an iron alloy, and it is a mixture of iron and carbon. Many steels with various strengths are manufactured, all depending on the percentage of carbon. Low carbon steel or mild steel contains less than 0.25-wt- % carbon. The inserted carbon atoms prevent iron atomic planes from sliding over one another when a force is applied and create a harder materials. A higher amount of carbon produces harder steel; however, it makes them more brittle. In fact, hard high carbon steel with 0.5-1.5-wt- % carbon can sometimes break due to the high amount of carbon. Low carbon and high carbon steel can rust when they are exposed to oxygen or moisture. The mixture of Fe, Cr, Ni, C is named stainless steel, and it improves the corrosive property of steel. This compound is a steel alloy with a minimum of 10.5-wt-% chromium content, which allows the formation of a passive chromium oxide layer on the material and protects steel from stain, corrode or rust.

Stainless steel is classified into five basic categories by their crystalline structure: austenitic, martensitic, ferritic, precipitation hardened, and duplex. Martensitic stainless steels are like ferritic steels. However, by including carbon in the structure and applying heat treatment, they can be hardened and strengthened. Chromium is the main element in their structure, usually up to 12-15% with molybdenum (0.2-1%), no nickel, except for two grades, and 0.1-1.2% carbon. They possess resistance against mild abrasive particles, fretting and particle erosion and are mainly employed in corrosion resistance applications. As discussed before, WC-Co offers extensively wear resistance property in several industries such as aviation aerospace, metallurgy, and electric power generation. However, due to low corrosion property and oxidation resistance and also high manufacturing cost of WC-Co other materials like austenitic and martensitic stainless steels are considered to be more comprehensive in some industrial applications. In comparison between these two main categories, austenitic stainless steels are highly recommended when corrosion resistance is vital. On the other hand, in an erosive environment, they erode and deform plastically. As for martensitic stainless steel, they are more resistant against erosive particles and more susceptible to corrosion (Figure 1.10) [25, 26].

Material	30°	45°	60°	90°
304 stainless steel	 205 mm <sup>2</sup>	 185 mm <sup>2</sup>	 160 mm <sup>2</sup>	 153 mm <sup>2</sup>
316 stainless steel	 230 mm <sup>2</sup>	 205 mm <sup>2</sup>	 186 mm <sup>2</sup>	 179 mm <sup>2</sup>
420 stainless steel	 240 mm <sup>2</sup>	 230 mm <sup>2</sup>	 225 mm <sup>2</sup>	 215 mm <sup>2</sup>

**Fig. 1.10:** Silicon carbide (SiC) erosion test at (30°, 45°, 60°, 90°) angles on 304,316 (austenitic) stainless steels and, 420(martensitic) stainless steel [27]

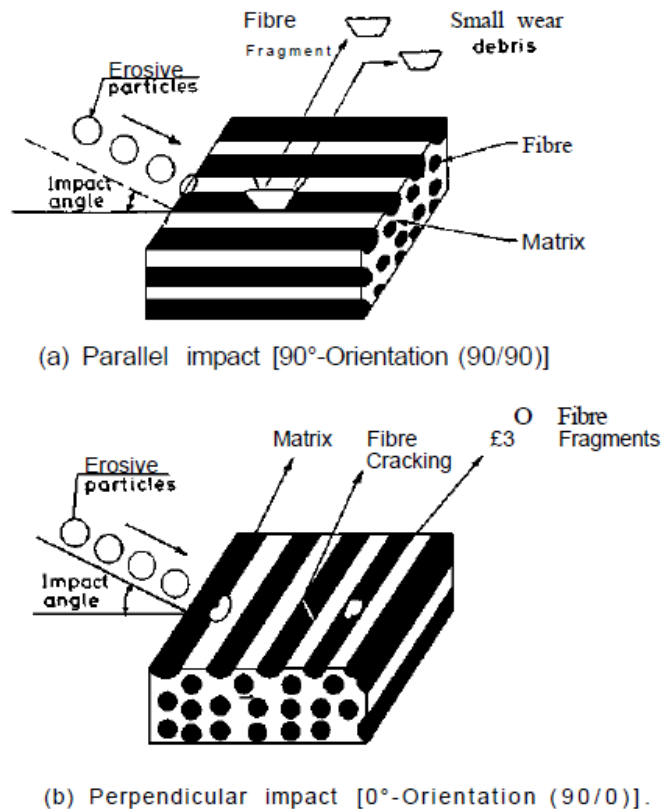
#### **1.4.4. Erosion behavior of polymer matrix composites (PMC)**

Nowadays, polymer-based composites have been used in aerospace and wind industry, in applications such as turbine blades of aircraft engines, helicopter blades and wind turbine blades. These materials have high specific strength and stiffness in their structure as compared to metal alloys. A critical issue in using PMC in various applications is the removal of the material surface by erosion induced by solid particle impingement, which reduces the lifetime of these types of material and cause degradation in their performance. Many research have been carried out to evaluate the tribology behavior of polymer matrix composites and extend the lifetime of these materials. In order to overcome this task, it is important to study the erosive wear behavior of (PMC).

It is more difficult to analyze the erosion behavior of PMC due to the large variety of matrix materials and the heterogeneity and the anisotropy of their structure. It was shown that by adding brittle fibers to the composite structure, the erosion resistance of the material reduces at lower angles in comparison with the resin matrix alone. When the resin is removed by the impact of the impinging particles because of its low-volume fraction compared to the reinforcement, the brittle fibers are completely exposed and can break due to micro-bending and fracture [28-30]. In one previous studies, unidirectional fiber-reinforced composites demonstrated less erosion resistance property compared to short-fiber reinforced composites [31]. And also, at normal angles, bi-directional glass fiber reinforced epoxy is less damaged by the eroding particles in comparison to unidirectional reinforced composites [31]. Earlier, researchers have indicated the connection between the erosion rate and fiber orientations and showed that in case 90/0 ( $0^\circ$  fiber orientation) as compared to 90/45 ( $45^\circ$  fiber orientation) and 90/90 ( $90^\circ$  fiber orientation), especially at  $60^\circ$  angle impact, erosion resistance drops [32,33]. It was also pointed out that in case of parallel impact, after the resin is removed, the erosive particles hit the fibers directly, and the interface of fiber and matrix becomes less supreme(Fig.1.10a). On the other hand, when the impact happens in a perpendicular direction, the resistance of the bundle of fibers is significantly lower, and fibers easily get broken. Therefore the erosion rate of the composite increases (Fig. 1.10b). Also, at  $45^\circ$  fiber orientation, the same behavior with fibers bending and breaking easily was observed [34]. Another conclusion from previous studies was that the carbon fiber reinforcement composites are better against erosion when they have interleaves in their structure. The essence of interleaves helps adjacent layers to stick better to the composite. This indicates that the number of interleaves

and their position can define the amount of material lost when they are exposed to solid particles impingement [35]. Between carbon fiber and glass fiber composite materials, carbon fiber reinforced structures have shown approximately three times more resistance to erosive wear [36].

Up until today, coatings was one of the many ways to protect any surface of materials against environmental damages. However, depending on the surface and compatibility and adhesion properties of the coating/substrate couple, coating of PMCs is quite a challenge. The protective layer on top of the composites must be thin and low weight and also enhance the erosion resistance of the compound. The fact that PMCs can be exposed to limited temperature reduces the number of coating processes and can affect the properties of the coated layer. In fact, maintaining the coating layer on the surface and produce good adhesion with the composite is more substantial. Furthermore, repairing damaged coatings and inconsistency between old and new coatings is another issue in the coating process of PMCs.

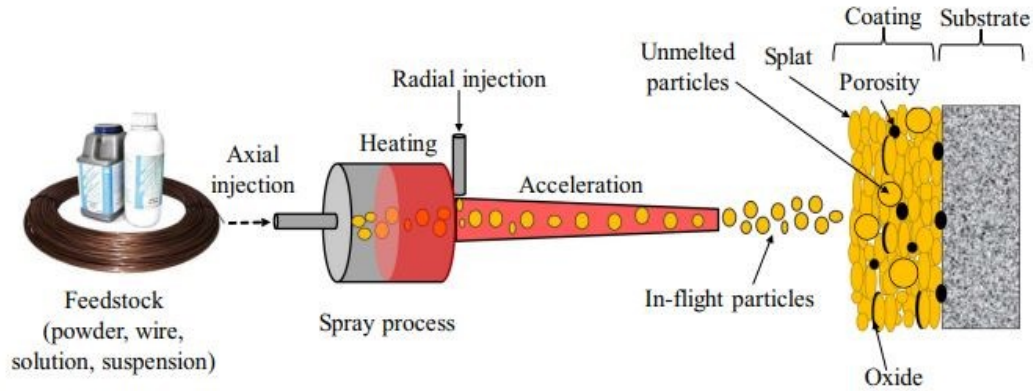


**Figure1.11:** Schematic diagrams of the erosive process in unidirectional fiber-reinforced composites under (a) parallel and (b) perpendicular impact conditions [34]

## **1.5. Thermal spray processes and surface engineering**

Thermal spray technology comprises a series of coating processes applied on top of different surfaces to enhance their properties and enlarge their applications. Engineers have used this technique in many industrial applications which includes wear prevention, dimensional restoration, thermal insulation and control, corrosion resistance, oxidation resistance, lubricity films, abrasive actions, seals, biomedical environments, electromagnetic properties, etc. In spray processes, the feed stock materials of different forms such as powder, wire, rod, liquid suspension or liquid precursor are introduced into a spray gun or torch to be heated up or close to their melting point and propelled to the substrate surface (Figure 1.12). This technology family comprises flame spray, electric arc spray, plasma spray, high-velocity oxyfuel spray, detonation gun deposition, and cold spray with their different specifications and characteristics. All the mentioned processes accelerate the coating particles (droplets) towards the substrate where they cool down and form thin lamellae called splats. These thin lamella adhere to the surface of the substrate, and the already deposited lamella until the layer of coating is built up. In addition to splats, different features are observed in thermal spray coatings such oxides or, in some cases, unmelted particles. Also, the coating structure may contain a different percentage of porosity, which can alter the coating properties and can be beneficial in some applications.

The coating thickness can vary between 50-500  $\mu\text{m}$ . In fact, it can be minimized to a few micrometers but can reach few micrometer. Each material depending on its property forms a different size of coating thickness. All materials that can be melt without decomposition are suitable for this type of process, which creates variable options for the coating process. Most of the thermal spray processes are able to produce an appropriate coated layer without a large increase of the substrate temperature during spraying, even when spraying materials with a high melting point like tungsten. Another interesting advantage about spray processes in general is their ability to deposit and remove coatings without affecting the substrate properties.



**Figure 1.12:** Schematic diagram of a thermal spray process [37]

Many different coating materials are currently used in thermal spray processes, including metals, intermetallics, ceramics, polymers and cermets. Thermally sprayed metallic alloys have the advantage of being high strength, corrosion, and wear resistant, and can be repaired. They are coated on automotive and diesel engine parts, turbine blades, bridges, mining and agricultural equipment. As for ceramics, they actually provide improved material properties for wear and corrosion resistance, thermal protection, electrical insulation applications. Ceramic coatings are mostly applied by plasma spraying. Cermets are mostly utilized in wear resistance applications and are easily sprayed on the substrate by the HVOF process. In the HVOF process of cermets, the ceramics part is usually deposited without melting while the metallic-matrix materials are partially or fully melted [38].

### 1.5.1. Surface preparation

To establish a suitable spray coating layer, some primary operations need to be applied to the substrate surface. These steps are vital and necessary to develop a desirable adhesion between the coating layer and substrate. There are various methods to perform a good surface preparation such as grit blasting, addition of granular material on the surface, using abrasive papers or chemical treatment. The procedure of surface preparation consists in cleaning and roughening the surface. In the first step, all the contamination like grease, oil, moisture, rust, scale, and paint on the surface is removed. The cleaning process is usually carried out by solution-based cleaners or perhaps by mechanical methods in order to make a good interface contact between the substrate and the coating. Using solvent cleaners like acetone, acid-based or alkaline-based cleaners is actually an economical, and efficient way for the first stage of the surface preparation process. In addition,

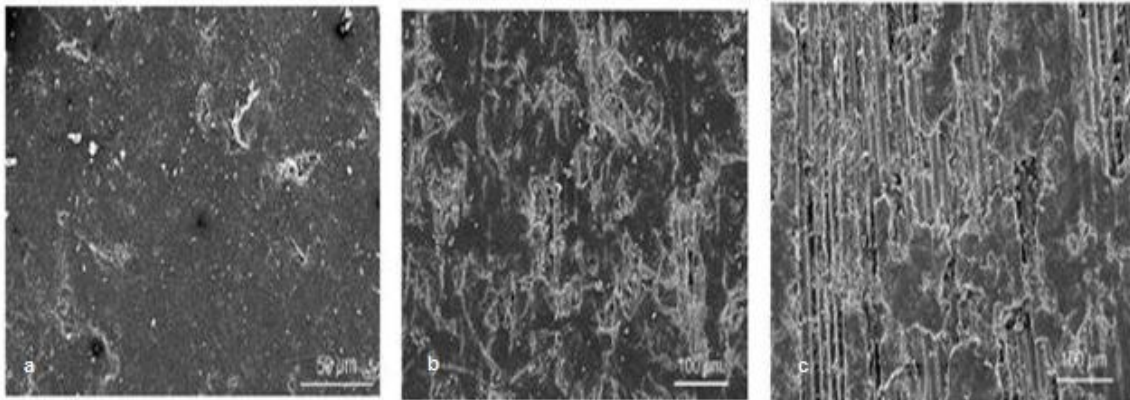
thermal cleaning and ultrasonic cleaning are other ways of cleaning the surface. Sometimes using solution-based cleaners is not conceivable and in order to remove the deeply penetrated oils, the substrate is heated to a temperature between 315-345 °C. In ultrasonic cleaning, the ultrasonic solution starts to vibrate at ultrasonic frequencies using transducers, and those transducers convert an electronic signal into a mechanical vibration and cavitation inside the ultrasonic bath, which enforces the cleaning process. This method is used for dislodging hidden contamination and also decontaminate some grit particles and dust. After proper surface preparation, the substrate to be coated needs to be dried before a roughening treatment like grit blasting is carried out. Therefore, in ultrasonic cleaning, possible contamination may leave on the substrate. For this reason, usually, this method is not recommended as coating cleaning technique [38].

In surface preparation, the most important and vital step is to roughen the surface. It is essential for the substrate to have enough roughness on its surface in order to build a good mechanical bond with the coating layer. Different methods have been used to roughen the surface effectively, and the most popular way is dry abrasive grit blasting. In this method, different sizes of abrasive granular particles like SiC or alumina are accelerated towards the surface at different angles to erode the surface and enhance its roughness. The abrasive particles cause compressive stress on the surface and induce the material to deform. However, in some sensitive substrates like PMC, the excessive applied force can weaken the properties of the polymer during the grit blasting or even damage the resin-fiber structure. For example, Liu et al. [39] and Guanhong et al. [40] utilized this method to roughen the top surface of carbon fiber-reinforced polymer composite substrate (CFRP) prior to plasma spray Al and Zn coatings. As seen in Fig 1.13, broken and damaged fibers were observed due to grit blasting of the surface. Grit blasting increases the roughness, which benefits in establishing better mechanical interlocking and metallurgical interactions between the molten particles and the substrate.

Many factors influence the roughness level in grit blasting and aid in preventing the sample from getting damaged. Important factors such as erodent particle angularity, size, density, and hardness, grit blasting carrier gas pressure, as well as particle impact angle and velocity are effective parameters in blasting the substrate. Sometimes abrasive papers are another approach to develop more effective surface areas for coating particles. However, in this method, the surface roughness is not uniform, and it requires typically more time to roughen the surface. For better

quality and further improved adhesion, another way is to apply an intermediate layer called bond coat before the topcoat. This bond coat layer prepares an ideal surface morphology for bonding with the coat layer. Also, bond coats like MCrAlY can provide improved properties of the coating structure, such as reinforcing the interlocking and reducing the oxidation of corrosion-resistance of the coated parts [40].

Recently a method called chemical treatment is being tested to create higher quality bonding between the coating and the substrate. In fact, in this method, by significantly increasing the surface energy, higher coating adhesion is achieved compared to mechanical treatment ways like grit blasting. In one trial, this procedure was evaluated for coating carbon fiber reinforcement polymer substrates. It was performed in three steps. First, the substrate surface was treated in a solution containing 25 vol.% 2-(2-butoxyethoxy)ethanol for 10 minutes. Afterward, the CFRP was treated by KMnO<sub>4</sub> for about 10 minutes, and finally, the composite was exposed to a 1 M solution of trichlorotriazine in toluene at 60 °C for about 24 hours, and the results showed better coating adhesion strength in comparison to the grit blasting method [41].



**Figure 1.13:** SEM image of a glass fiber-reinforced polymer GFRP substrate after Al<sub>2</sub>O<sub>3</sub> grit blasting for (a) 2, (b) 4, (c) 6 seconds

Lastly, the final step for surface preparation before spraying is to clean the surface with any of the mentioned ways in order to remove any grit or contamination caused in the roughening phase.

In the following sections, different processes for depositing thermal spray coatings on polymer-based composite substrates are discussed.

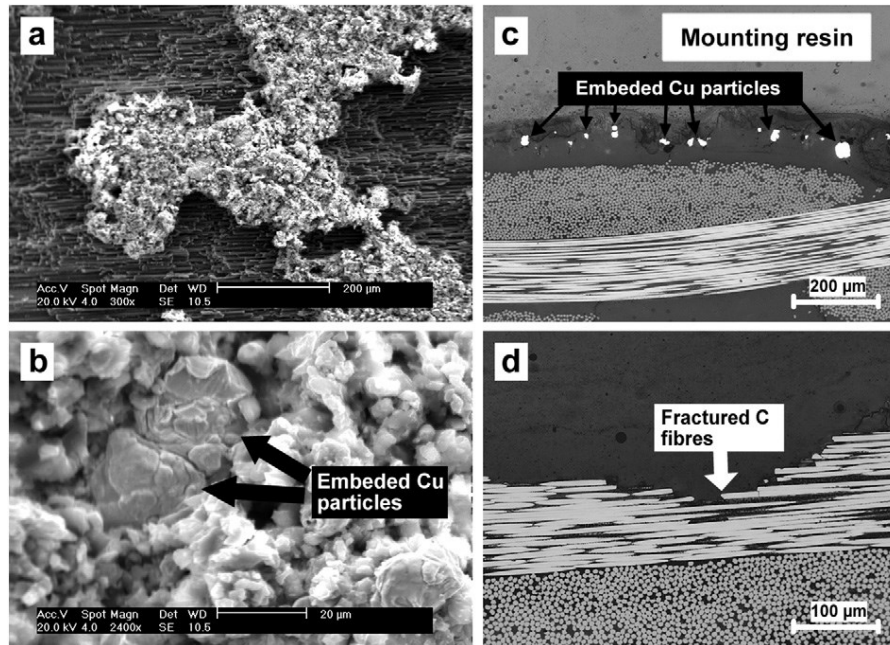


### 1.5.2. Cold spraying

One of the coating processes in the large family of thermal spray coating processes is cold spray. In this process, solid-state particles with sizes ranging from 5 to 100 [38]. The gas used in the cold spray process is nitrogen N<sub>2</sub>, helium He, or their mixtures, which is compressed up to 3.5 MPa. Nitrogen is usually chosen as spray gas due to its low cost but it limits the maximum speed the particle can reach. The gas is fed to a converging-diverging nozzle, called a Laval nozzle, to reach supersonic velocities. The powder is injected into the nozzle and heated below their melting point [43]. Very fine powders are preferred in this process as coating materials (the mean diameter size of the particles is in the range of 1-50 μm) [44]. In cold spray, the gas and particle velocities are higher while the gas and particle temperatures are lower compared to other thermal processes. When the particles are at the critical velocities upon impact with the substrate, instead of bouncing off or erode the surface, they deform and build up coating layers. The critical velocity is not constant and differs with the particle and substrate material. The mentioned velocity creates a high level of kinetic energy enough to soften the particle and force them to adhere to the surface and already deposited particles [45,46,47]. Previous studies have demonstrated that cold spraying ductile materials like metals is possible. On the contrary, it is not recommended for brittle materials like ceramics. The temperature of cold spray gas usually varies around 30 to 1000 °C to balance out the adiabatic cooling during the gas expansion. However, the temperature of the particles do not go over 200°C, and this benefits in manufacturing layers of coating with high velocity and low-temperature particles. In other words, the gas inside the jet is not for heating up or softening the particles but to enforce higher particle velocity. Additionally, this characteristic reduces the chance of high-temperature oxidation, debonding, recrystallization, tensile residual stresses, gas release or other concerns potentially encountered in other thermal spray processes.

The cold spray process has been divided into two main categories: low-pressure cold spray (LPCS) and high-pressure cold spray (HPCS). Depending on the kinetic energy of these two types, different coating deposition efficiency and structure are obtained. In the LPCS process, the particle impact velocity is between 300-600 m/s, and the gas pressure is less than 1 MPa. By contrast, the pressure of the HPCS process can rise up to 5 MPa, and the particle impact velocity is typically still higher reaching 800 to 1400 m/s. In the case of the high-pressure spraying process on polymers, the composite substrate may be damaged due to the high energy impact of the particles. Additionally, particles can penetrate into the composite structure as seen in Figure 1.14. However,

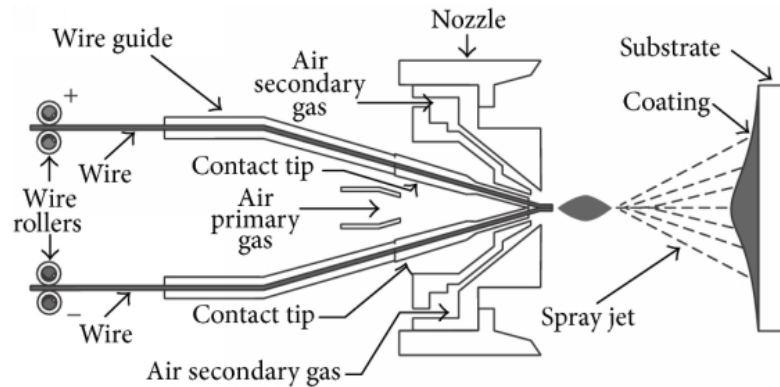
in low-pressure cold spray, the kinetic energy is lower and possibly not sufficient to form a uniform coating [48,49].



**Figure 1.14:** SEM images (a and b) and cross-section optical micrographs (c and d) of the CFRP after cold spray of spherical Cu powder (the bright particles in c are copper, and the clusters of bright dots in c and d are the carbon fibers perpendicular to the observation plane)[50].

### 1.5.3. Arc spraying

One of the other thermal spray processes is called arc spray, which is sometimes named twin wire arc or wire spray. In this method, the system of power supply and material feeding equipment is the same as other thermal spray processes. However, instead of using gas jets, an electric arc established between the two wire ends and melt them [38]. With the assist of compressed air, they the molten material is atomized and the resulting metal droplets are accelerated towards the substrate (Figure 1.15). The size and distribution of the particles made in the arc spray system are typically coarser than those in plasma or flame spray. Metallic or metal-based composite coatings can be produced with this process by using. Material feed rates in arc spray are high as compared to other thermal spray processes reaching several kilograms per hour.



**Figure 1.15:** Schematic wire arc spraying process [51].

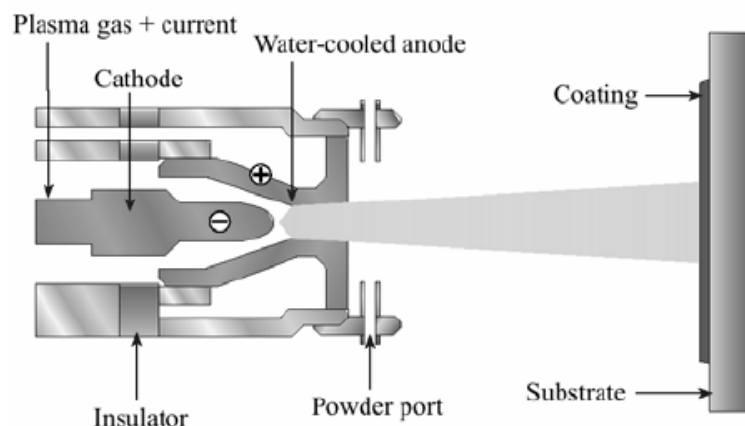
There are many factors such as increasing the current, reducing the voltage, rising the air pressure flow or decreasing the wire size that control the size of the molten particles in arc spraying. Some major differences exist in this type of thermal spray process, such as thermal efficiency and amount of particle oxidation. The thermal efficiency is much higher in arc spray. In fact, with the same amount of energy, less material can be deposited in plasma spray or other thermal spray processes. In comparison to flame or plasma spray, particle oxidation can occur on a larger scale due to the fact that in the arc spray system, the droplets are already molten when they leave the end of the wire and located in the gas jet; hence, they start to cool down faster and oxidize more. However, by reducing the standoff distance, the amount of oxidation can diminish. Furthermore, the utilization of inert gases can minimize the extent of oxidation. In the AS process, splats are thicker with different sizes, unlike plasma or flame spray coating. Actually, shortening the standoff distance or utilizing high-velocity air caps can reduce particle dwell time providing a more desirable coating microstructure. Other factors can enhance the properties of the arc spray microstructure, such as depositing at lower feed rate by utilizing smaller diameter wires and preventing overheating of droplets by reducing the arc voltage.

One of the main advantages of using the arc spray system is to deposit coatings with a lower heat consumption. Using arc spray instead of flame or plasma spray reduces the heat transfer to substrate per amount of material deposited. It means that the temperature of the substrate is reduced, which is beneficial for substrates vulnerable to excessive temperature like polymers, reinforced composites, wood, or paper products. In arc spray, less heat can create less stress

between the coating layer and the substrate (caused by the different mechanical properties of the two material), which avoids the coating from getting delaminated or cracked [38].

#### 1.5.4. Plasma spraying

Plasma Spray coating is one of the advantageous and accessible processes in the thermal spray coatings. In plasma, particles are heated and accelerated by an expanded hot gas jet and directed towards the substrate (Figure 1.16). The particles are deformed and solidified to generate a layer of coating. The hot gas jet is produced by a plasma arc gun, which comprises an axially aligned tungsten cathode, oxygen-free high-conductivity copper anode, and a segment to maintain the gas flow geometry in the arc chamber. Tungsten is chosen as a cathode material due to its high melting point and the ability to emit electrons at high temperature. The copper anode, on the other hand, is for stabilizing the arc and accelerating the heated gases. There are many different designs of plasma spray guns; some are for enhancing the particles' velocity, and some for reducing the speed of the plasma to have higher dwell time as well as more efficient particle heating. The plasma jet characteristics depend on several factors like the shapes of the anode and cathode, power, arc gas flow rate, and gas composition. Typically, a mixture of argon with helium or hydrogen as secondary gases are used as plasma gases. Due to its ionization potential and thermal heat capacity, argon has created low energy plasma. The mixture of the argon/hydrogen is generally used as plasma gas. 20 to 50% helium enhances the thermal conductivity and heating capacity of the plasma gas, and 5 to 15% hydrogen boost the enthalpy compared to Ar/He mixture because of the diatomic structure of the hydrogen and its capability to increase the life expectancy of the design gun [38].



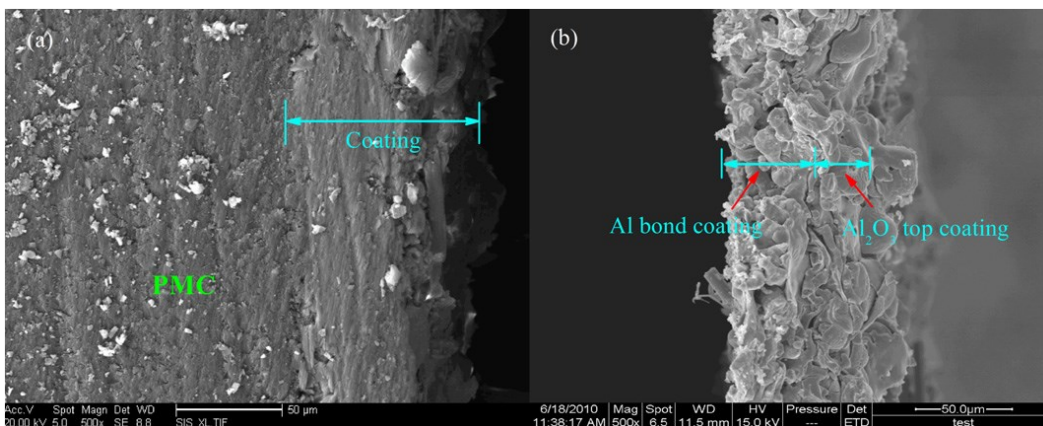
**Figure 1.16:** Schematic of a plasma spray torch [52]

The high-quality microstructure of plasma spray coatings is due to the high particle/droplet kinetic energy and high degree of heating/melting. Therefore, higher deposition densities and stronger adhesion bonds are obtained compared to most flame or arc spray coatings. The plasma spray coating porosity, which can range from 1 to 40%, is related to the characteristics of the powders, the deposition parameters, and the gun geometry. A strong adhesion between the substrate and the deposited layer is achieved in plasma spray coating: bonding strength usually exceeds 34 MP and can reach up to 70 MP. The inert gas of the plasma jet reduces the amount of oxidation by reducing the ambient air effects. However, in the atmospheric plasma spray process, the turbulent plasma jet is in contact with ambient air, which increases the amount of oxidation and creates an oxide phase in the coating. In some cases, oxidation can be an advantage, and in some others, it cannot, but for those applications in which the oxidation is a drawback, control of the standoff distance, particle velocity, and particle heating lessen the oxidation in the process [38].

Plasma spray is divided into three groups with different characteristics: a) Atmospheric plasma spraying (APS) in which the plasma jet proceeds directly into the ambient air, b) Controlled atmosphere plasma spraying (CPS), in which the plasma jet proceeds into a controlled atmosphere chamber and c) Low-pressure plasma spraying or vacuum plasma spraying (LPPS or VPS), in which the jet proceeds into a low-pressure chamber (i.e., 10-30 kPa) [53]. APS is usually employed in many different applications such as industrial sectors, including aeronautics, energy, automotive, mining, biomedical, and electronics. In APS, the microstructure is created from stacking the lamellae after impact, flattening, and solidification of the molten particles impinging on the substrate. One of the main advantages of using APS is its high deposition rate, for example, more than one kilogram per hour of raw powder can be deposited with plasma guns with no more than a few tens of kilowatts at a relatively low operating cost. The fact that this method is highly flexible in coating various materials and various substrates with different size, and shape makes plasma spray suitable for to deposit thick coatings [54].

One of the common ways to metalize polymer structures is to use a plasma spray coating. In previous studies, low melting point powders like Zn and Al were utilized as a coating material to coat PMC materials. As an example, Guanhong et al. [40] used atmospheric plasma spray in order to deposit Al as bond-coat and  $\text{Al}_2\text{O}_3$  as top-coat on PMC substrates for increasing their mechanical properties. This experiment took place to demonstrate the importance of plasma spray parameters

in coating thermal sensitive structures like polymer reinforcement composites. The effects of spray parameters were observed in the microstructure, phase composition, and mechanical properties of the coated samples. In addition, producing a desirable adhesion bonding between the substrate and the coated layer is reached by optimizing spray parameters, as was shown in Guanhong et al.'s work. The maximum shear adhesion strength achieved for the Al bond-coat was about 5.21 MPa. In another experiment, plasma spray alongside spray was used to deposit an aluminum coating layer onto CFRP substrates. A thin layer of aluminum coating (about 15  $\mu\text{m}$ ) first was plasma sprayed on the composite surface, and after, with cold spraying process, deposition of the second aluminum layer as a top-coat was carried out. The combination of two thermal processes in coating CFRP substrate in this study resulted in a microstructure with less oxidation and higher thickness.



**Figure 1.17:** Cross-sectional SEM images of the coating (bond coating and top coating), (a) coating on the PMC, (b) coating separated from PMC [40].

## 1.6. Objectives

The main purpose of this study is to develop a process to uniformly deposit of a high-quality tungsten carbide 20 wt. % cobalt, martensitic chromium stainless steel and alumina 3 wt. % titania coating onto a polymeric carbon fiber-reinforced composite (CFRP) by using a plasma spray technique for wear and erosion resistant applications in aircraft and wind turbines.

Other objectives of this study are also listed as follows:

- Identifying the challenges associated with the coating of polymeric materials and the factors that make the coating of PMCs different from metallic materials

- Using different preparation and surface modification methods for preparing the carbon fiber-reinforced polymer (CFRP) substrates prior to the coating deposition process.
- Depositing the three selected powders and analyzing the effects of spray parameters on the microstructure and quality of the coatings.
- Determining and comparing solid particle erosion resistance and the hardness of the coated samples with the three selected powders.
- Comparing the adhesion bonding strength of the coatings produced with the three selected powders coating.

## 2. Experimental method

This research project is performed through seven steps including:

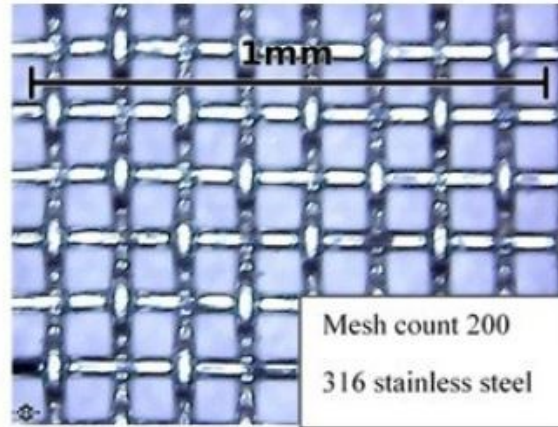
- 1) Fabrication of carbon fiber-reinforced polymer composites (CFRP) and cutting them into smaller samples,
- 2) Samples grit blasting and substrate preparation,
- 3) Deposition of three different coating powders by using plasma spraying,
- 4) Analysis of the microstructure of each coating,
- 5) Solid particle erosion resistance test of the coated samples,
- 6) Determination of the hardness of the coated composite samples,
- 7) Measurement of the coatings adhesion strength.

These steps will be detailed in the following sections.

### 2.1. Substrate fabrication

The first step is to fabricate a 30 x 30 cm<sup>2</sup> square plate by utilizing carbon fiber-reinforced polymer prepreg (CFRP) and stainless steel mesh cloth. Prepregs are flexible sheets which are made of fibers impregnated with partially cured epoxy resin [56]. The material used in this study is the carbon fiber-reinforced polymer prepregs CYCOM® 977-2, manufactured by Solvay Composite Materials. In the first step, the roll of prepreg was taken out of the freezer and held at the room conditions for about three hours, this resulted in rising the temperature of prepreg to room temperature, and reducing the viscosity so that cutting the prepregs into smaller shapes can be done without difficulty. After that, the prepregs were cut into 30 cm by 30 cm square sheets (laminas). Twenty unidirectional CFRP plies (i.e. [0<sub>20</sub>] composite) were cut to make a 3 mm thick composite plate. An aluminum flat plate was used as the tool. Before transferring the laminas to the tool for making the composite plates, the tool needs to be cleaned with acetone. Then the tool surface was covered with a layer of release agent to make it easier to detach the laminates from the tool. The 20 CFRP plies were aligned and stacked carefully to each other by hand for making the plate. Woven wire #200 stainless steel mesh cloth (type 316) was placed as an additional layer on top of the laminas. The image and properties of this steel mesh cloth are shown in in Figure 2.1 and Table 2.1, respectively. The reasons and purposes of incorporation and utilization of this cloth on top of the composite plate are going to be discussed and indicated in detail in the coming chapter.





**Figure 2.1:** Microscopic images of the 200-mesh stainless steel cloth [57].

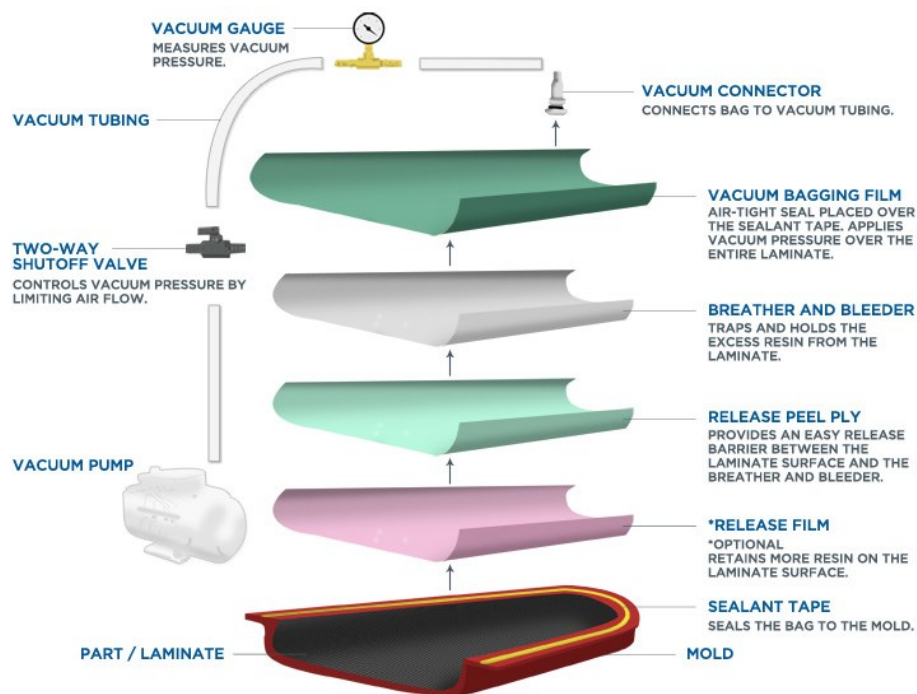
**Table 2.1:** 200-mesh stainless steel cloth properties [57]

Mesh Count	Nominal aperture	Wire diameter	Open area (%)	Weight kg/m <sup>2</sup>
200	75µm	60µm	34	0.28

Moving to the next phase, the tool and CFRP plates were vacuum-bagged in order to consolidate the composite plates inside autoclave. The process of vacuum bagging is an effective way to cure and manufacture the CFRP parts under autoclave pressure. This process is carried out by bundling up the composite plates and depressurizing air [58]. In fact, vacuum bagging is applied in the curing process of the composite to assist with the removal of the trapped air between the prepreg layers, which can cause delamination, and to have good compaction between the layers during the manufacturing process.

For vacuum bagging of the composite laminates and to prepare them for curing, five items were used which are plastic bagging film, peel ply or release film, breather and bleeder cloth, an aluminum caul plate, and a vacuum pump. Another vacuum bagging material is a sealant, which was also used for making the airtight seal and closing the bagging film to the tool (mold), which provides a perfect vacuum condition. The peel ply is located on the top of the laminate to have a good surface finish and to make it easier for detaching the bagging materials from the part after curing. One of the important parts of the vacuum bagging process is to use two layers called breather and bleeder cloths. They were placed exactly beneath the vacuum bagging film to serve two main purposes. These two layers are for absorbing and extracting excessive materials. Breather

aims to ease the airflow and direct it through the laminate. In fact, by placing the vacuum connector directly on top of the breather, the air, along with any gases released during the cycle, is pulled out from the part and through the cloth. Moreover, a bleeder is chosen to absorb excess epoxy by vacuum during the curing process. An aluminum caul plate was placed on top to have a flat and smooth surface at the end. A vacuum pump was connected to the vacuum bagging film using a hose and a vacuum connector. Different steps and schematic of the mentioned layers and components of a vacuum bag are illustrated in Figure 2.2.

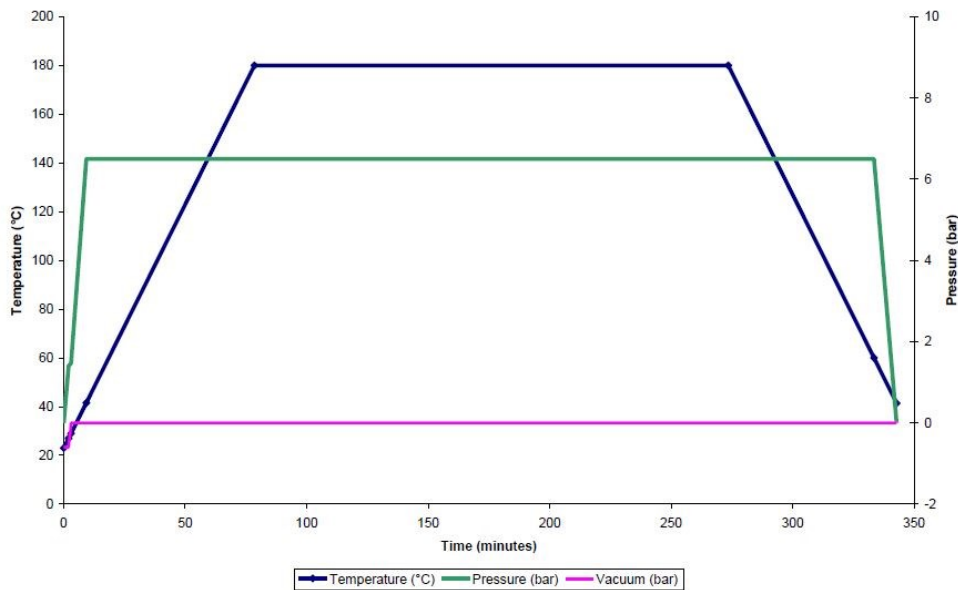


**Figure 2.2:** Schematic of a typical vacuum bagging lay-up [59].

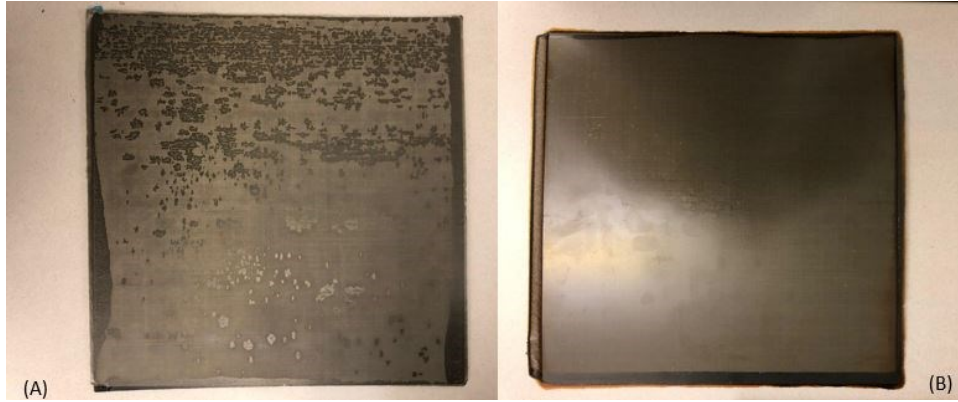
After preparing the preregs and vacuum bagging them, it is time to put them inside an oven or autoclave for curing. In oven, the material can be subjected to the heating cycle while in autoclave both heating and pressure cycles can be applied. Using oven is more economical but the quality of the final part might not be the best. The common ways to manufacture a strong composite structure is to use an autoclave where both temperature and pressure can be adjusted and applied. Figure 2.3 illustrates the curing cycle (heating and pressure cycle) recommended by the material supplier for the curing of the composite plates [60]. The cure cycle consists of three steps. First, the temperature of the autoclave increased from room temperature to 180 °C with the ramp of  $2 \pm$

1 °C/minute in about 75 minutes. At the same time, the autoclave pressure starts to increase up to 6 bars. Then, the temperature was kept constant in the range of  $180 \pm 5$  °C for about 180 - 210 minutes. Finally, the autoclave was cooled down with the rate of  $-2 \pm 1$  °C/minute for about 100 minutes when the autoclave pressure is released as well.

At the first attempt, an oven was used to make a panel. Once the curing cycle was completed, the vacuum bag was removed out of the oven, and all those extra layers on top of the plate in the vacuum bag film were detached from the composite plates. Since no external pressure was applied, the metal mesh on the top was not completely covered with the resin, as shown in Figure 2.4 a. One of the objectives of this research is to create a powerful bond between the stainless steel mesh cloth and CFRP, and to achieve this purpose, applying the necessary pressure to wet all parts of the woven cloth is essential. Therefore, the next panel was made inside autoclave. Metal mesh was completely covered by the resin, as shown in Figure 2.4 b.



**Figure 2.3:** Recommended heating cycle for curing CYCOM® 977-2 prepreps [60]



**Figure 2.4:** (a) 200 mesh plate in oven (b) 200 mesh plate in autoclave

## 2.2. Substrate preparation

In thermal spray coatings of polymer matrix composites, one vital element to create adequate bonding between the composite and coating is to prepare the substrate and enhance its surface roughness with one of the surface preparation techniques. As mentioned in the previous chapter, there are many ways to apply surface preparation. In this experiment, grit blasting was chosen for the preparation of the composite substrates. More than seventy 2.5 x 2.5 cm samples were grit-blasted. The various optimized parameters and right conditions for obtaining a suitable surface with enough roughness to bond perfectly with the coating layer were found after grit blasting of 15 samples. Each of these samples was grit blasted with parameters reported in Table 2.2 and then removed from the grit blasting machine to be observed carefully under the microscope. Table 2.2 shows the parameters and conditions in which these sample substrates were grit-blasted. The angle of the grit blasting gun as well as its distance with substrate were kept constant as 90 degrees and 6 cm, respectively, in the whole process. The moving pattern of the grit blasted gun in front of the samples must also remain unchanged for all samples. The grit used for the grit blasting process was alumina grit with a diameter of about 80  $\mu\text{m}$ . The two most important variables in grit blasting these types of substrates are the compressed air pressure and duration of grit blasting. Exceeding the optimized value will damage the metal mesh cloth and prevent desirable adhesion between two layers. Following the grit blasting, the surface of the samples was examined by confocal microscope and profilometer device for analyzing the surface topography and measuring the roughness.

**Table 2.2:** Grit blasting parameters used for roughening the samples.

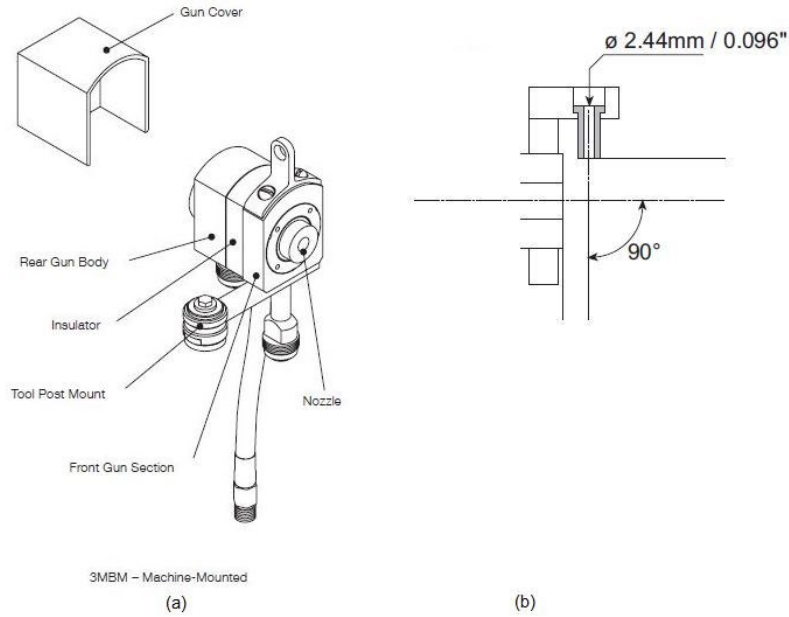
<b>Sample No</b>	<b>Pressure (psi)</b>	<b>Time (Sec)</b>	<b>Standoff distance (cm)</b>	<b>Roughness (<math>\mu\text{m}</math>)</b>
1	76	140	6	3
2	60	150	6	1.5
3	70	150	6	2
4	80	150	6	1.3
5	73	150	6	2.6
6	42	150	6	0.5
7	74	150	6	2.9
8	68	150	6	2.6
9	52	150	6	2.7
10	54	150	6	2.8
11	53	150	6	3
12	42	150	6	1.9
13	51	150	6	2.4
14	53	150	6	3.2
15	53	150	6	3.5
16	53	150	6	3.2
17	53	150	6	2.8
18	53	150	6	3.3
19	53	150	6	3.3
20	53	150	6	3.4
21	53	160	6	3.5
22	53	160	6	3.0
23	53	160	6	3.5
24	53	160	6	2.9
25	53	160	6	3.5
26	53	160	6	3
27	53	160	6	3.2
28	53	160	6	2.8

29	53	160	6	3.6
30	53	160	6	3.0
31	53	170	6	3.1
32	53	170	6	3.2
33	53	170	6	3.3
34	53	170	6	3.5
35	53	170	6	3.2
36	53	170	6	3.3
37	53	170	6	3.5
38	53	170	6	3.0
39	53	170	6	3.5
40	53	170	6	3.4

### 2.3. Coating process of composites

One of the thermal spray coating processes for coating composites is atmospheric plasma spray (APS). One of the advantages of using this type of coating is the ability to control the temperature of the substrate and avoid damaging the composite samples. As discussed in the previous chapter, in the plasma torch, an electrical arc is formed between the anode and cathode to ionize and heat the plasma gas. The plasma gas with high temperature and high velocity exits the torch and hits the powder coming out of the powder feeder, which results in the melting the powder particles and their acceleration towards the substrate surface [38].

In this experiment, three types of powders have been selected for coating the composite substrates. Each powder was deposited with different spray parameters and different thermal spray conditions. A 3MB plasma spray gun (Sulzer Metco, Westbury, NY) was used to spray the powders with a 90°-degree feed injector angle. The selected nozzle for tungsten carbide 20 wt. % cobalt and martensitic chromium stainless steel was GE and for alumina 3 wt. % titania was GH (Figure 2.5). As mentioned before, around seventy 2.5 cm by 2.5 cm samples were grit blasted, and close to fifty of them were coated. The chemical composition and particle size distribution of the spray powders are presented in Tables 2.3, 2.4, 2.5. The proper and nearly optimized surface preparation condition of all the composite substrates utilized to find a set of spray parameters and all the tribology test are shown in Table 2.6.



**Figure 2.5:** (a) The structure of a 3MB plasma spray gun (b) feed injector 90° angle [62].

**Table 2.3:** Chemical composition and particle size distribution of the Metco 76F-NS powder (labelled WC20Co) [61]

WC20Co	W	CO	C	Fe	Others
Weight percentage	Balance	19.0-23.0	5.0-6.0	1.0max	1.0max
Size distribution (µm)	-53 +11 Fine and coarse(bimodal)				

**Table 2.4:** Chemical composition and particle size distribution of the Diamalloy 1002 powder[61]

Martensitic stainless steel	Fe	Cr	Ni	Mn	C	Si	P	S
Weight percentage	Balance	12-14	-	1.0max	0.15min	1.0max	0.03max	0.03max
Size distribution (µm)	-45 +15 (Irregular)							

**Table 2.5:** Chemical composition and particle size distribution of the Metco 101NS powder (labelled Al<sub>2</sub>O<sub>3</sub>-TiO<sub>2</sub>) [61]

Al <sub>2</sub> O <sub>3</sub> -TiO <sub>2</sub>	Al <sub>2</sub> O <sub>3</sub>	TiO <sub>2</sub>	SiO <sub>2</sub>	Fe <sub>2</sub> O <sub>3</sub>
Weight percentage	94	2.5	2.0	1.0
Size distribution (µm)	-45 +11 (Angular / Blocky)			

**Table 2.6:** Grit blasting parameters used for the surface preparation.

Substrate	Pressure (psi)	Time (sec)	Standoff distance(cm)
CFRP with layer of mesh 200	53	170	6

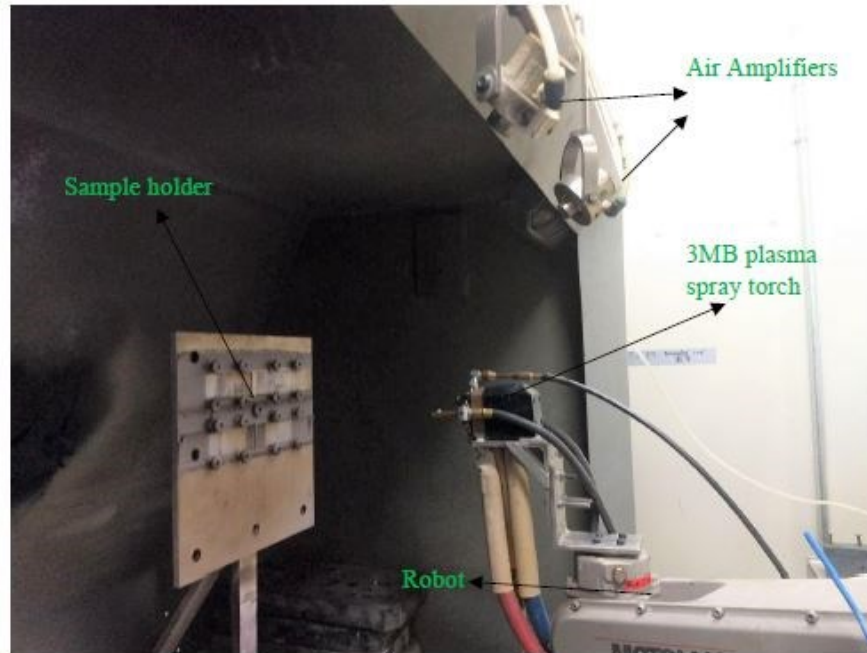
Two different patterns were employed to identify an applicable set of spray parameters for the composite substrates. First, using reference parameters which were provided by Oerlikon Metco [61]. Second, to prevent our vulnerable substrate from burning, we used the processing parameters reported in a previous study [4]. Most spray parameters used in this experiment are recommended by Oerlikon Metco company. However, the feed rates for tungsten carbide 20 wt. % cobalt, martensitic chromium stainless steel, and alumina 3 wt. % titania were reduced from 45, 53, 53 g/min to 30, 25, 21 g/min, respectively. The objective is to decrease the amount of power transferred to the substrate during spraying and protect it from burning [4]. Reducing the feed rate helps with reducing the surface temperature of the substrate during spraying. The spray parameters of these three powders are shown in Table 2.7.



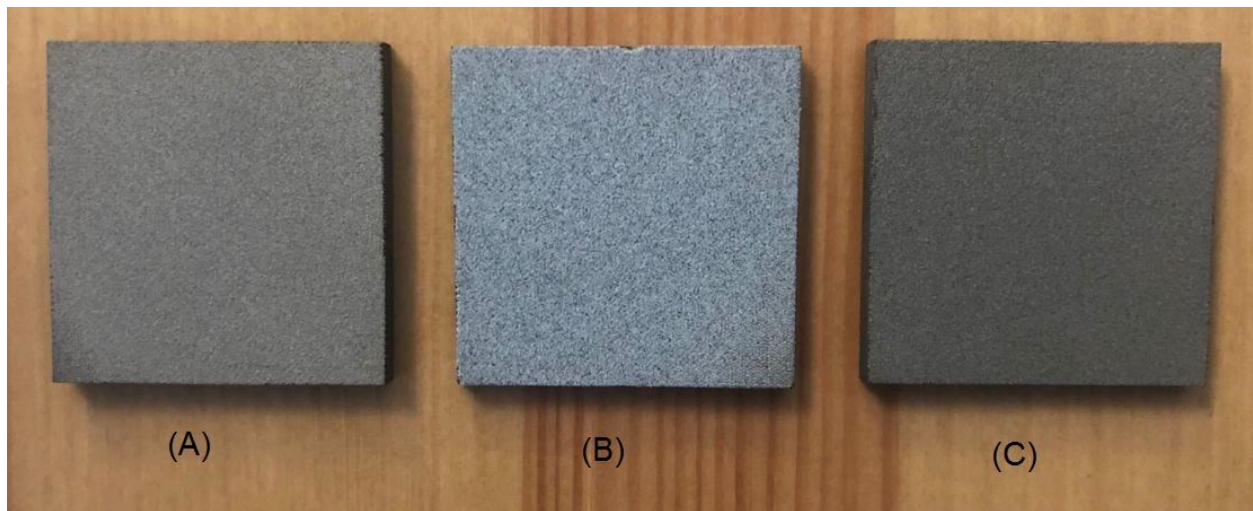
**Table 2.7:** The plasma spray parameters used for the coating of the PMC substrates

powder	Current (A)	Voltage (V)	Primary gas, Ar (nlpm)	Secondary gas, H2 (nlpm)	Powder feed rate (g/min)	Spray distance (mm)	Robot speed (m/s)	Number of passes	nozzle
WC20Co (Ref)	400	55	78	6.6	45	80	1	6	GE
WC20Co (Exp.)	400	55	78	3.5	30	80	1	6	GE
Martensitic stainless steel (Ref)	500	55	73.1	6.6	53	80	1	6	GE
Martensitic stainless steel(Exp.)	500	51	73	2.5	25	80	1	6	GE
Al <sub>2</sub> O <sub>3</sub> TiO <sub>2</sub> (Ref)	500	64	39.4	2.6	53	80	1	6	GH
Al <sub>2</sub> O <sub>3</sub> TiO <sub>2</sub> (Exp.)	500	55	40	5	21	80	1	6	GH

All equipment such as sample holder, 3MB plasma gun, robot, and air amplifiers used in thermal spray laboratory to coat the samples are illustrated in Figure 2.6. All samples were weighted, and their thickness was measured before and after the coating process in order to calculate the thickness and the deposition efficiency of each coating. In this study, preheating was not applied before each coating experiment. Furthermore, two air amplifiers and two air blowers were installed on top of the sample holder to reduce the temperature of the substrate during spraying as much as possible and under the composite maximum service temperature (about 180 °C). After finding accurate spray parameters, seventeen 2.5 cm by 2.5 cm samples for each set of coating material were prepared and used for characterization and tribology tests (Figure 2.7).



**Figure 2.6:** Plasma spray process equipment [4].



**Figure 2.7:** Samples after (A) WC<sub>20</sub>Co coating (B) Al<sub>2</sub>O<sub>3</sub>TiO<sub>2</sub> coating (C) Martensitic stainless steel coating.

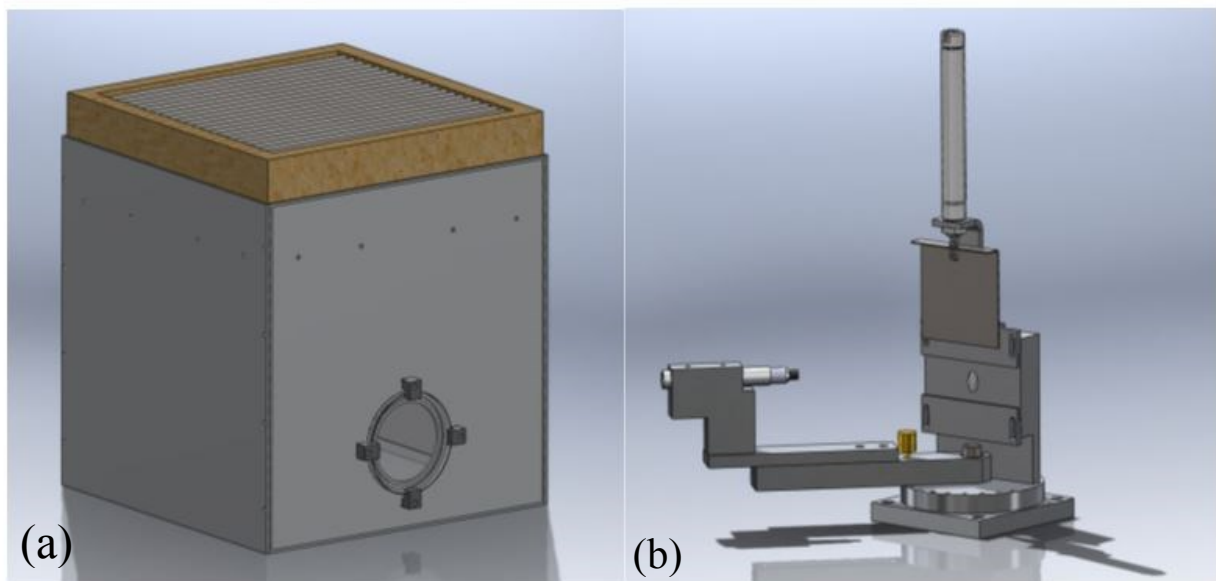
## 2.4. Image analysis and coating characterization

One way to evaluate the morphology of composite microstructure coating is to use the metallographic technique. The procedure of this process consists of four main steps: sectioning, mounting, grinding and polishing. The size of the coated samples is 2.5 cm by 2.5 cm, and they have to be cut into smaller segments with a size of (1.5-by-2.5 cm). First, the samples are cut in the middle by a cutting machine, so the coating structure assessment can be accomplished from the center of the samples. The next step is to mount the cut samples with the cold mounting method, which assists with analyzing the samples and enhances their protection during the subsequent metallographic preparation steps. The cold mounting method starts with mixing the epoxy and hardener together with the ratios of 89% and 11%, respectively. Then the mixture was poured into the sample cap and leave for 24 hours to solidify. All the caps were placed in the oven for 1 hour to guarantee the required solidification and curing. After the mounting process, the mounted samples were ground by using abrasive papers. The grinding process requires time and accuracy to avoid any mechanical surface damages. In fact, the process of grinding provides a mounted sample with less uneven and damaged surfaces resulting from the cutting and sectioning the samples. The samples were rotated and ground by the polishing machine with three different abrasive papers, first with 180, and then 300, and finally with 600 mesh silicon-carbide (SiC) papers, sequentially. The grinding process of each paper was for about two minutes. After finishing grinding, samples were washed with water or ethanol to clean any residue. The next step is polishing, which is vital for the samples in order to have a scratch-free, flat, and mirror-like surface. In polishing, three splashes of diamond suspension with a particle size of 6  $\mu\text{m}$  were put in a rotating disk with a moisturized hard cloth disk. The moisturization occurs with specific lubricants. After that, with the same method, another polishing process was applied with another diamond suspension with a particle size of 3  $\mu\text{m}$ . Finally, the samples were cleaned with ethanol for microscopic evaluation with an optical or scanning electron microscope.

Nowadays, scanning electron microscopy (SEM) has become one of the common surface imaging technique to analyze the topographical property of coating structure. In this research, both an optical and SEM microscopes were used to measure the thickness and observe the microstructure of deposited coatings.

## 2.5. Solid particle erosion testing

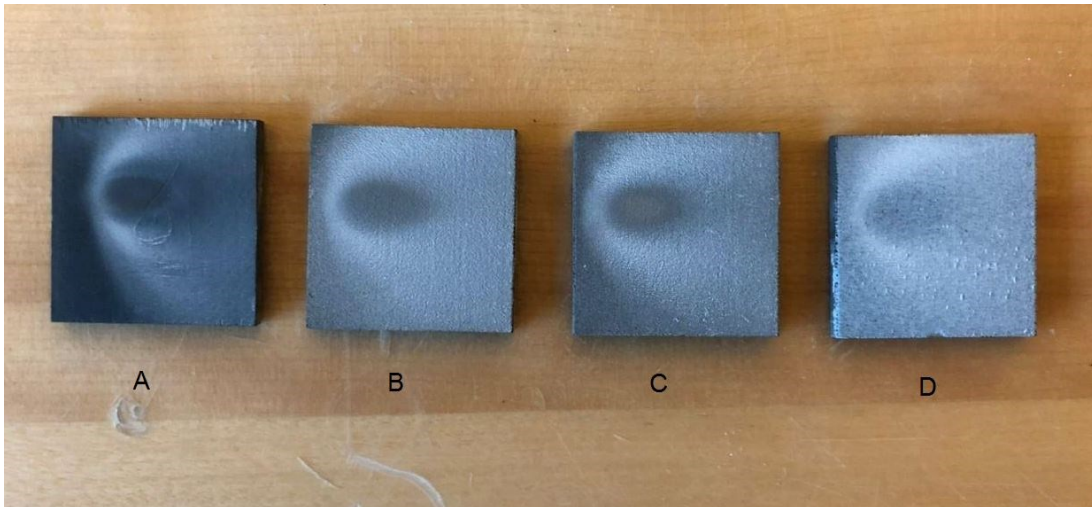
Solid particle erosion test was chosen to evaluate the erosion resistance properties of the CFRP coated samples. The procedure of this erosion test was based on accelerating erosive particles with a pressurized gas jet with respect to the specifications of the ASTM standard G76 [63]. In this test, an abrasive blasting unit was designed to establish the erosion rate and the mass loss of the eroded materials. This unit consists in a cubic box with an industrial dust collector, HEPA filter, two quartz windows, and sample-nozzle holder. A HEPA filter is located on top of the box to help gathering efficiently the used erodent particles and derive more accurate results. Two quartz windows are placed on both sides of the cube for better observation and control over the impact phenomena and material loss mechanisms (Figure 2.8(A)). The whole glove box is located on a high capacity balance to measure the mass of erodent particles during testing. A sample-nozzle holder is a carefully designed part located in the chamber to position the samples accurately and in line with the particle stream (Figure 2.8(B)). Behind the sample-nozzle holder, there is a vacuum tube line which sucks the air behind the sample and makes it stand in front of the nozzle.



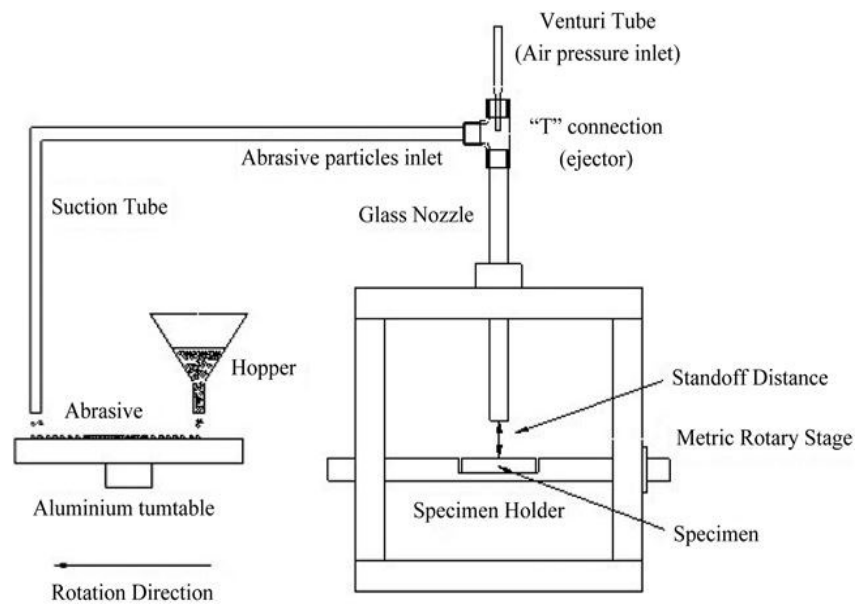
**Figure 2.8:** (a) SPE testing chamber with windows and a HEPA filter. (b) Sample and nozzle holder for SPE testing with retractable shutter [64].

The back pressure of the erosion test unit is adjustable permitting to control the particle velocity. In addition to the back pressure, the unit's shaker amplitude is another factor used to control the particle feed rate. In order to monitor the particle feed rate, the erosion test unit was located on a balance with a 30 kg capacity and precision of 0.1 g (Sartorius LE29000). The cylindrical nozzle used in this work is designed by ASTM G76 standard features, and it is made of tungsten carbide. The inner diameter of the nozzle is 1.14 mm, and its length is 36 mm. As indicated in Figure 2.8(B), the nozzle is constructed to carefully control the angle of the impact between the particle stream and the surface of samples by turning the arm on which the nozzle is placed. Also, the nozzle design assists in measuring the length between the tip of the nozzle and the sample surface, which is called the working distance. The working distance for this research in all angles is equal to 20 mm. Another important part of the nozzle-sample holder is called the shutter, and it is actually located in front of the sample holder. In the beginning, before the test starts, the shutter is closed to protect the sample from the particle stream while the system is on and is stabilizing to increase the test accuracy.

Before each experiment, all samples were cleaned with isopropanol and compressed air to remove all the contamination from the surface. After cleaning all the samples, each one was weighted three times with the Sartorius LE225D analytical balance, which has a precision of 0.01 mg. Then, they were placed on the sample holder in front of the nozzle with a closed shutter. It usually takes several minutes for the unit to stabilize, and then the shutter opens and stays open for a duration of 2 minutes. All samples were eroded with 50  $\mu\text{m}$   $\text{Al}_2\text{O}_3$  particles and stabilized feed rate of  $1 \pm 0.3$  g/min. The abrasive particle velocity is  $30 \pm 2$   $\text{m} \cdot \text{s}^{-1}$  measured at the location of the particles. After the shutter is closed, the samples were cleaned and weighted three times and placed in the chamber for another 2 minutes. This procedure was repeated 5 times (total amount of 10 minutes) for four different surfaces (WC20Co, martensitic stainless steel,  $\text{Al}_2\text{O}_3$ - $\text{TiO}_2$  coated composite, and uncoated composite substrate for three different angles ( $90^\circ$ ,  $60^\circ$ ,  $30^\circ$ ). There are different approaches to report the erosion rate. In this research, the total amount of volume and mass loss of each sample was measured after being subjected to 10 grams of erodent powder, and the erosion rate was calculated by measuring the slope of the mass loss-time graph.



**Figure 2.9:** Wear scars from A) uncoated composite B) WC20Co coating, C) Martensitic stainless steel coating, D) Al<sub>2</sub>O<sub>3</sub>TiO<sub>2</sub> coating, eroded at 30° angle after 10 min.



**Figure 2.10:** a schematic diagram of the erosion rig [63]

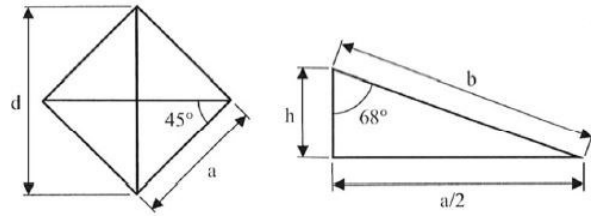
## 2.6. Vickers hardness testing

In every material erosion investigation, it is required to measure the hardness of the surface in order to have a better understanding of the erosion mechanism of the materials. One of the ways to measure the hardness is by indentation of the surface with at determined load and calculate the hardness by evaluating the dimensions of the remained mark of the tip of indenter in the tested coating. Lots of different indenters with a different geometry are utilized to measure the hardness.

However, in this work, for measuring four dissimilar surfaces, the Vickers tip geometry from the cross-section of the material has been chosen. The Vickers test was applied on the cross section of the coated samples with respect to the ASTM standard C1327 instructions [65]. The shape of the Vickers indenter is similar to a square base pyramidal diamond tip with an angle of  $136^\circ$  between faces (Figure 2.11). With this geometry, the hardness is going to be measured by using Equation 2.1:

$$H_v = \frac{P}{A} = 2 \cos 22^\circ \frac{P}{d^2} \quad (2.1)$$

where  $d$  is the diagonal of the residual trace and  $H_v$  is in GPa. The Vickers hardness is sometimes recognized by another name: Vickers hardness number (HVN), which is measured with the same formula but with  $P$  in kgf and  $d$  in mm.



**Figure 2.11:** Geometrical description of a Vickers type indenter [66].

A hardness measurement of coated samples through using Vickers indentation requires special considerations. During indenting a coated surface, the indenter may create the volume of plastic deformation greater than the coating thickness and place an overlap on the substrate. Consequently, the measurement will be significantly influenced by the hardness value of the substrate, which is usually smaller than the hardness of the tested coatings in the case of hard coatings deposited on metallic substrates. In such a condition, a solution was introduced to separate the substrate hardness ( $H_s$ ) and the coating hardness ( $H_f$ ) from the composite hardness ( $H_c$ ), measured with the Vickers tester. Using a geometrical approach, the relationship between these hardnesses can be expressed by:

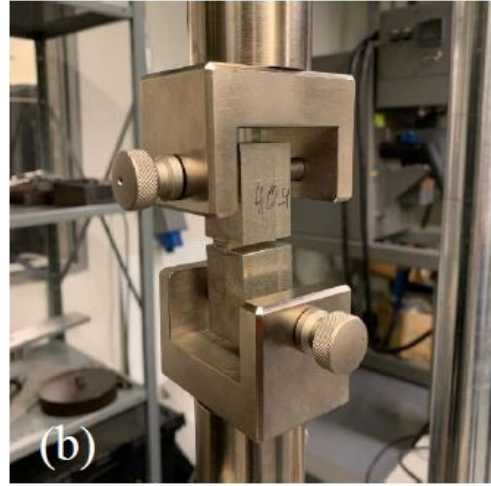
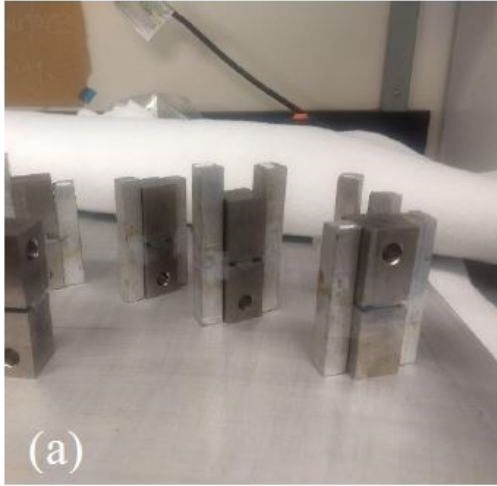
$$H_c = H_s + a(H_f - H_s) \quad (2.2)$$

where  $a$  is a model-based coefficient. Many experiments have been done to evaluate  $a$ , most common source proposed by Jonsson and Hogmark [68] and Chicot and Lesage [69]. The surface microhardness was measured using a square-based pyramid-shaped indenter (Mitutoyo SurfTest SJ-210) for testing in a Vickers tester. A nominal force of 500 gram-force (gf) and a loading time of 15 s were used for the tests. The average of five measurements was taken at the surface of each sample to accurately evaluate the variability of surface microhardness.

## **2.7. Adhesion strength testing**

The objective of this study is to provide a satisfying adhesion between the coating layer and composite substrate, which is evaluated by a flatwise tensile test to determine the bond strength of the coated samples. The flatwise tensile test was selected for the adhesion measurement between the substrate (composite) and coating. To do so, a two-component adhesive (Henkel Loctite Hysol EA 9392 AERO Epoxy Adhesive Gray, LOCTITE, Henkel Canada Corporation, Canada) including epoxy and hardener were mixed together with a weight ratio of 100: 32. After mixing the adhesive for 2 minutes and a half, both sides of the 2.5 cm by 2.5 cm coated sample and the top surface of the stainless steel fixture blocks were wetted by a thin and even layer of the mixture. The next step is to sandwich the samples between the steel blocks and aligning the samples and the blocks with the assistant of two metal pieces, as can be seen in Figure 2.12a. For the curing process of the adhesive, samples and blocks were then placed in an oven at a temperature of 85 °C for about 90 minutes. The curing process needs to be accomplished precisely to prevent any adhesive failure between blocks and the samples. After the curing process, the blocks were attached to two Wyoming flatwise tensile test fixtures by two pins (see Figure 2.12b), and they were held in a flatwise tensile machine (with the displacement rate of 0.50 mm/min) for applying tension and measuring the adhesion strength of the coatings. In the adhesion test, the detachment between the coating layer and the stainless steel mesh layer is considered to be the acceptable failure mode. After assessing the type of failure, in order to remove the adhesive and samples from the stainless steel blocks, they were heated in an oven to the temperature of 250 °C for about 60 minutes so that the adhesive could be removed easier by scraping the steel block cross-section.





**Figure 2.12:** Flatwise tensile test (a) sample alignment, (b) test equipment [4].

### 3. Results and discussion

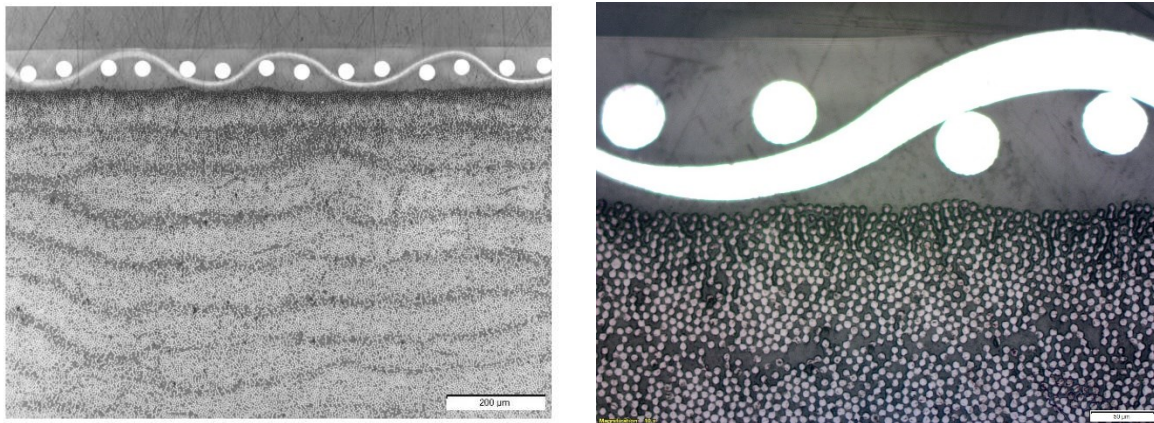
The first issue faced when coating polymer materials and, in particular, polymer matrix composites is to create a high strength bond between the coating layer and epoxy at the surface of the composite. Each surface has a certain amount of free energy, which affects the adhesive behavior of the material towards other compounds. In Table 3.1 Surface free energy of different materials is compared. Epoxy materials have a surface free energy of 43 dynes/cm, which is very small in comparison to stainless steel with a surface energy ranging between 700 and 1100 dynes/cm [70]. According to previous research results [4], placing an extra layer made of a metal mesh on top of the composite can conduct in higher surface roughness and a stronger bond with the coating. Composite plates with a woven stainless steel wire cloth 200 mesh as the top layer was selected to comply with that purpose as well as to create protect the composite fibers from the impact of high velocity and high-temperature particles during grit blasting and plasma spraying.

**Table 3.1:** Surface free energy of different materials [70]

Substrates	Surface Energy (Dynes/cm)
Copper	1103
Aluminum	840
Zinc	753
Tin	526
Lead	458
Stainless Steel	700-1100
Glass	250-500
Kapton® (Polyimide)	50
Phenolic	47
Nylon	46
Alkyd Enamel	45
Polyester	43
Epoxy Paint	43
Polyurethane Paint	43
ABS	42
Polycarbonate	42
PVC (Polyvinyl Chloride)	39
Noryl®	38
Acrylic	38
Polane® Paint	38
PVA	37
Polystyrene	36
Acetal	36
EVA	33
Polyethylene	31
Polypropylene	29
Tedlar®	28
Silicones	22-24
Teflon®	18

### 3.1. Analysis of CFRP substrate structure with wire mesh

In the first part of this work, we studied the structure of CFRP with a stainless steel 200 mesh as an extra layer on top. The idea of utilizing an extra layer of steel wire mesh in the structure of the composite materials has already been developed and applied for coating on the glass fiber composite materials for de-icing applications [4]. An optical microscope was used to inspect the cross-section of the structure and to observe the connection between the composite and the metal mesh after the curing process. Optical microscope images of the metal mesh on top of the laminate in two magnifications are shown in Figure 3.1. The epoxy wetted the mesh layer completely, penetrated into all the open areas between the mesh wires and formed a very thin and uniform resin layer on top of the mesh. After evaluating the cross-section of the composite substrate, the next step would be grit blasting the samples with the different parameters provided in Table 2.2. The effects of these factors are determined under the confocal microscope.



**Figure 3.1:** 200 mesh substrate cross-section with a 5x and 20x magnification.

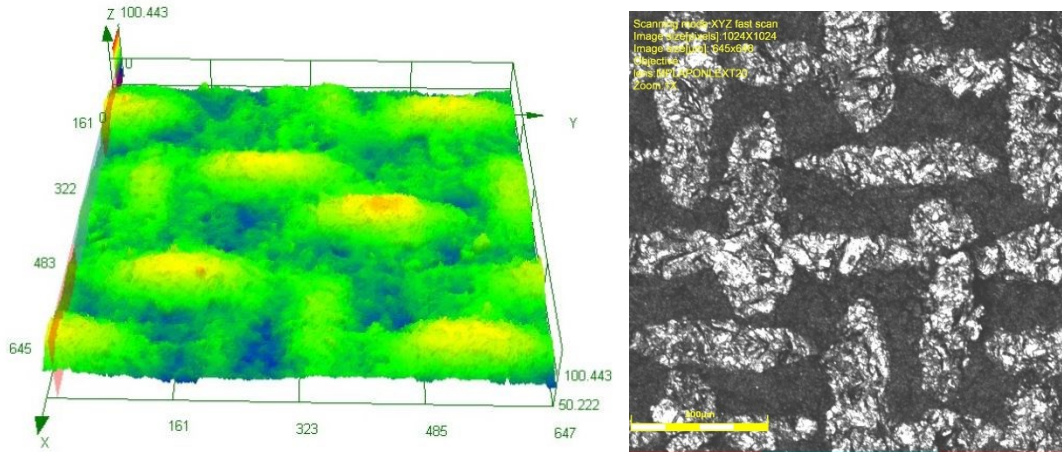
### 3.2. Grit blasting operation

Reinforced fiber polymers have demonstrated poor resistance and high vulnerability against erodent particle impacts, which can also be seen in the grit blasting process of the composite. Many factors have been taken into consideration to avoid damaging the fibers and roughening the composite surface simultaneously. In this study, the process of grit blasting has been done manually. Extra care has been taken to remove the extra resin and reach the surface of the mesh layer without damaging the wire mesh. There are some parameters that can be monitored, such as pressure, the distance between grit blasting gun and samples, the angle of the shooting, and also

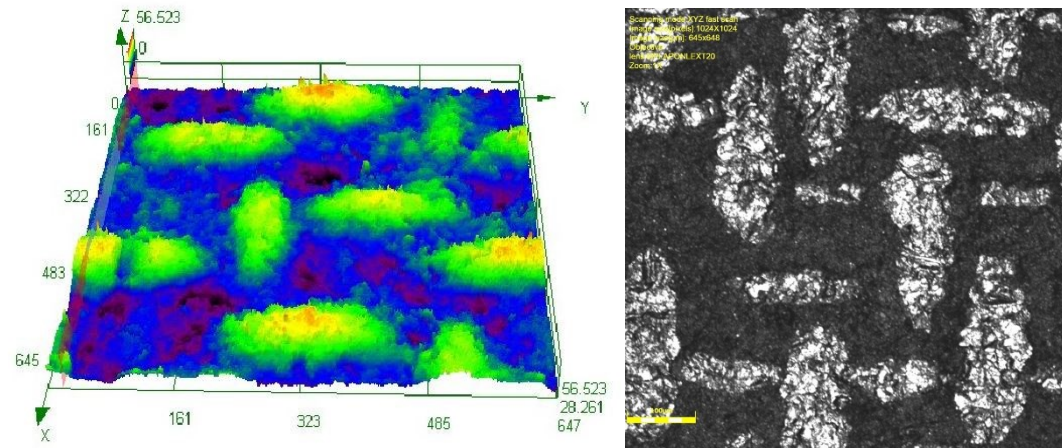
time. However, there are some other factors that can affect the process unintentionally. The fresh 80  $\mu\text{m}$  alumina grit with angular morphology was used in grit blasting, which can erode the surface strongly and promptly. The structure of the grit will change and become more spherical over a period of time of continuous usage. Considering this point, if the alumina grit is not fresh, the time and the pressure of grit blasting should increase to remove all the epoxy from the top of the surface of the mesh. This clarifies the reason why all samples were grit blasted on the same day and explains the difference between the optimized blasting parameters identified in this study and those identified in a previous study [4]. Furthermore, the process of grit blasting should be constant with the same pattern in the optimized time. Otherwise, some spots will be left with epoxy on top, and some other spots may get damaged due to an excessive number of alumina particles impacts.

Finding the optimized parameters for grit blasting requires a preliminary evaluation. Confocal images were taken to assess the influence of each parameter on the level of blasting. The influence of different grit blasting conditions and different parameters on condition of the composite surface has been studied. In Figure 3.2, a confocal image of a sample grit blasted with 42 psi for 150 s condition is shown. Clearly, there are extra epoxy still remains on the surface of the mesh. Therefore, the wires and the mesh are intact, and there will be low adhesion bonding between the mesh and coating layer. The time or the pressure of the grit blasting process was not sufficient enough to remove all the epoxy. In Figure 3.3, a confocal image of a sample grit blasted with 73 psi for 150 s condition is shown. In this situation, the epoxy was removed completely by the erodent particles. However, the strength of the particles' impact and high pressure damaged the mesh layer and destroyed some of the wires. Beyond this point, at higher pressure (like 80 psi), erodent particles will destroy the mesh layer completely and leave no wire. After grit blasting, the optimum point will be achieved when half of the metal mesh comes out of the epoxy, and the other half still remains well attached in the epoxy layer. At this point, the surface is rough enough to make good adhesion bonding between the coating layer, and the mesh is also firmly fixed to the composite. Therefore, the metal mesh creates a good surface for coating adhesion and also plays the role of anchor for the coating. Finally, the confocal image of grit blasted sample with 53 psi for 150 s condition indicates that steel wires are in good shape, and the epoxy is removed from the top of the wires perfectly without destruction of the wires, which is sufficient for coating deposition.

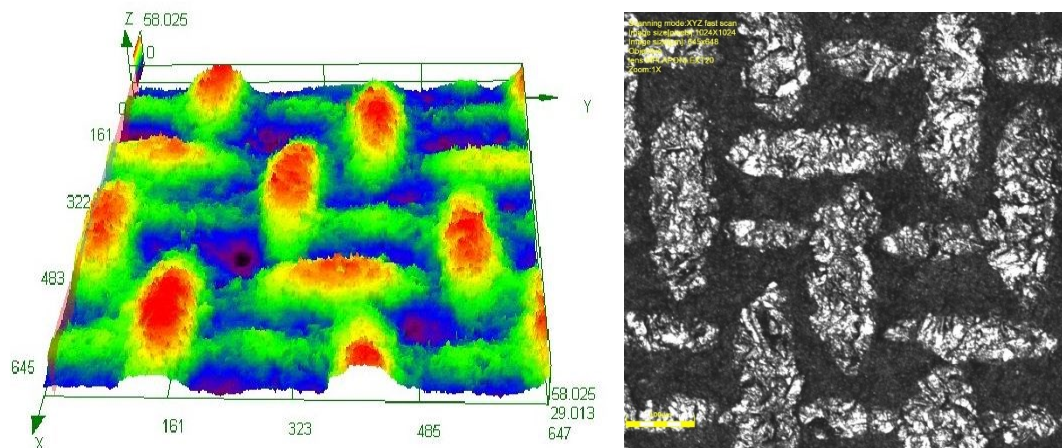




**Figure 3.2:** Confocal images of a grit-blasted 200 mesh substrate (P= 42 psi and t= 150 s).



**Figure 3.3:** Confocal images of a grit-blasted 200 mesh substrate (P= 73 psi and t= 150 s).



**Figure 3.4:** Confocal images of a grit-blasted 200 mesh substrate (P= 53 psi and t= 150 s).

### **3.3. Microstructural characterization of plasma spraying coatings**

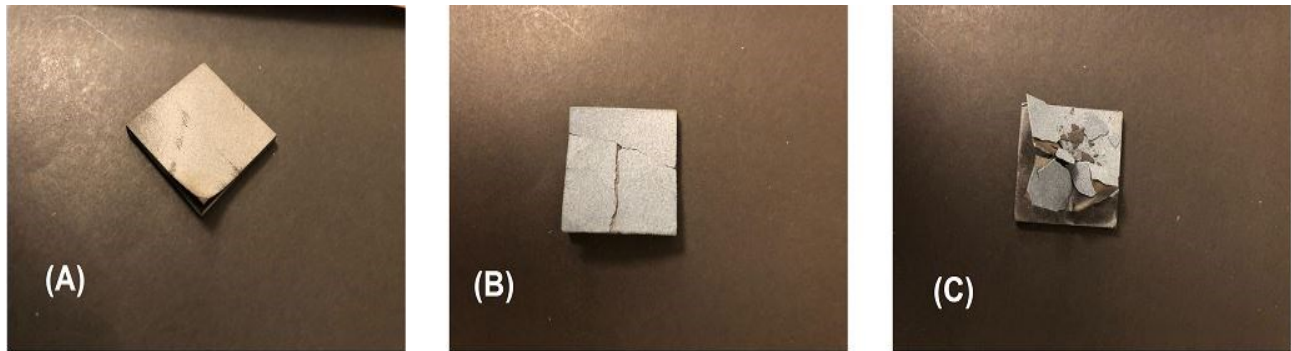
The primary objective of this work is to apply three wear resistance coatings on CFRP with atmospheric plasma spray without any substrate destruction.

#### **3.3.1. Analysis of tungsten carbide 20 wt. % cobalt APS coating**

The first powder is tungsten carbide 20 wt. % cobalt, which has a high cobalt matrix content. The particle size distributions of the three powders are in the same range to facilitate the adjustment between the results. Coatings produced by atmospheric plasma spray is expected to contain more oxide than those produced by HVOF with the same powder. The use of a larger particle size distribution contribute to decrease the amount of oxidation in the spray coatings. In the case of tungsten carbide 20 wt. % cobalt, a relatively large particle size distribution ( $-53 +11 \mu\text{m}$ ) was selected. Typically, thermal spray tungsten carbide coatings are produced by using the high-velocity oxygen fuel (HVOF) spray or detonation spray (DS) processes. In comparison to HVOF and or D-gun sprayed coatings, APS tungsten carbide coatings have a relatively high porosity and present a significantly higher carbide phase degradation leading to lower wear resistance properties [71]. Also, in the HVOF coatings, the porosity value is lower in contrast to the APS coatings due to the high speed of the impacting particles improving their cohesive strength within the coating and reducing the porosity [72]. However, due to the vulnerability of the PMC materials to high-speed particle impact, this coating process will not be effective. Atmospheric plasma spray was chosen to be the coating process of WC20Co because of its ability to produce lower particle velocity and reduce heat transfer to the substrate. However, the usual decomposition and decarburization of the tungsten carbide during the plasma spraying occur, which degrade the cermet properties. This transformation reduce the quantity of WC in coatings which results in forming of unfavorable phases like  $\text{W}_2\text{C}$ , W and amorphous or nanocrystalline Co-W-C phase. It has been well established that the extent of decarburization of WC-Co particles in APS coatings is much higher compare to HVOF or DS processes [73].

The APS process involves extreme plasma temperatures (up to 10,000 K) at the nozzle exit to which the particles are exposed [74]. In this research, it is vital to control the temperature of the composite surface in order to avoid any degradation in its structure. As seen in Figure 3.5, excessive heating of the steel mesh-composite substrate can be resulted in a) the steel cloth and coating peeling off, b) cracking the coating layer, c) entire destruction of the mesh layer and

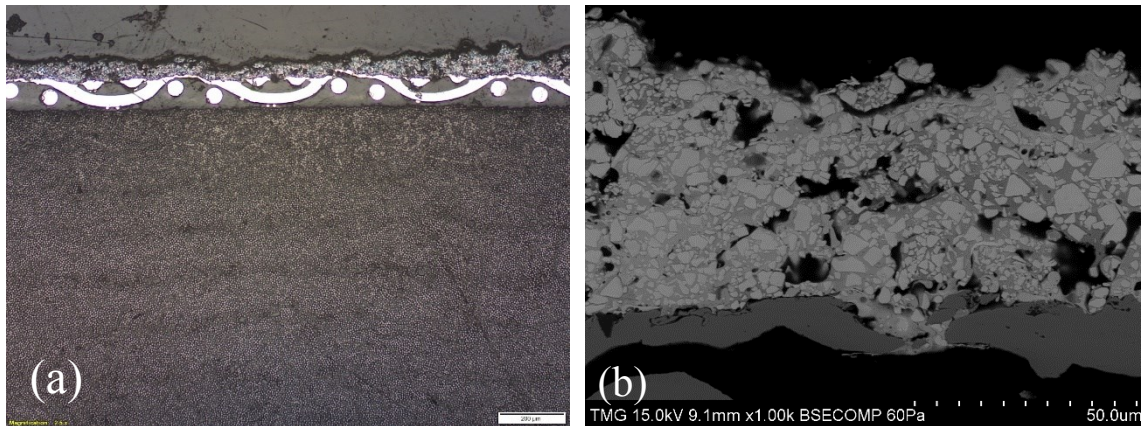
coating layer. There are many ways to control the input power of the plasma and reduce the surface temperature of the substrate, such as decreasing the powder feed rate, reducing the plasma current or increasing the spray distance. Considering the low resistance of the composite substrates to high temperatures, the spray parameters recommended by Metco Oerlikon, which were meant for producing dense, well-bonded coatings were changed, and the feed rate was decreased from 45 to 30 g/min. This reduction in the feed rate will prevent the samples from burning and destruction.



**Figure 3.5:** Different types of coating failure a) the steel cloth and coating peeled off, b) cracking in the coating layer, c) entire destruction of the coating and steel mesh layer.

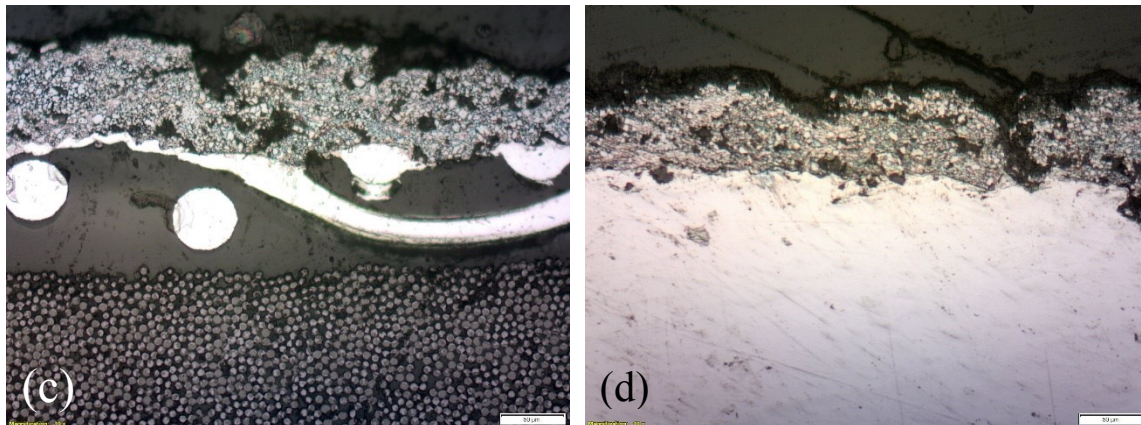
From the optical microscope images of the WC20Co coating in Figure 3.6 (a), it is clear that the mesh layer was able to create a surface with enough roughness for WC20Co coating to bond perfectly and produce a coating of acceptable quality. The steel mesh also protected the composite part, especially the fibers, from the impact of spray particles. Predictably, after optimizing surface preparation, the mesh layer was able to create a good anchorage in the epoxy part of the composite and improves the adhesion bonding between coating and substrate. As discussed before, the first step to building up a uniform coating layer is to remove all the epoxy from the top surface of the composite. Otherwise, a coating with less thickness and weak adhesion bond is produced. An average thickness of 76  $\mu\text{m}$  with a surface roughness of 9.7  $\mu\text{m}$  were obtained after six passes of WC20Co deposition.





**Figure 3.6:** Cross-section of WC20Co coating on a PMC sample a) optical image at low magnification b) SEM image at high magnification.

The same spray parameters were used to spray the WC20Co coating on a mild steel substrate to see the effectiveness of the mesh in producing the same coating with the same thickness. As illustrated Figure 3.7 (a) and (b), the results on both substrates are comparable with the same range of thickness. After applying EDS analysis on WC20Co coating shown in Figure 3.6(b), it was observed that the white areas are WC and gray areas are CO, and clearly, dark spots are pores.



**Figure 3.7:** Cross section images of a WC20Co coating sprayed on a) composite with metal mesh b) grit-blasted mild steel sample.

### 3.3.2. Analysis of martensitic stainless steel APS coating

In the next experiment, martensitic chromium stainless steel powder with  $-45 +15 \mu\text{m}$  size distribution and irregular morphology was coated on the composite substrate. Although the HVOF spray process of Diamalloy 1002 produces the highest hardness, with lower porosity and the best



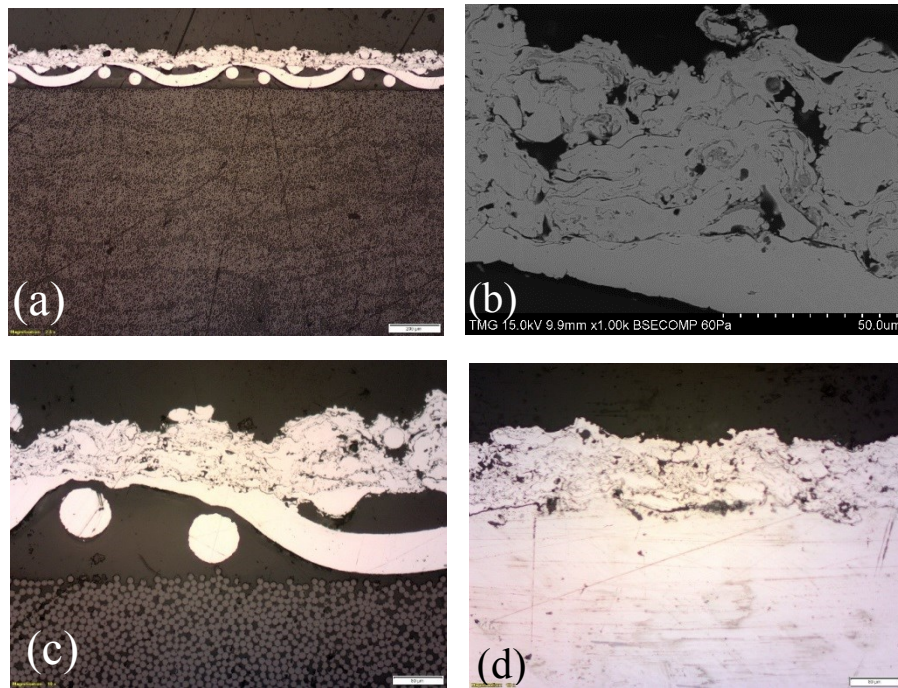
wear resistance, atmospheric plasma spray was used to spray this powder. The Diamalloy 1002 powder provides a combination of good wear and corrosion resistance properties, especially when a heavy coating build-up is required. By utilizing proper surface finish instruments like silicon carbide wheels, this type of coating can be ground to a very good surface finish with low surface roughness [61]. The recommended processes to deposit this stainless steel powder are HVOF or APS. In this work and considering the substrate sensibility to high temperatures, the APS process was utilized. The powder feed rate was reduced from 53 to 25 g/min to limit the temperature of the PMC surface as discussed before. The 25 g/min was sufficient enough to produce a coating with desirable deposition efficiency.

No sign of the steel cloth and coating peeling off, cracks, deformation or other sorts of damage to the coating or mesh was observed. The pre-heating of the substrate is also one step of the surface preparation before thermal spraying, which is exploited to burn and volatilize moisture or any retained liquid in the substrate. It also minimizes the influence of the coefficient of thermal expansion mismatch between the coating and substrate materials and may help improving the adhesion and cohesiveness of the coating layer [38]. However, in the case of carbon fiber reinforcement composites, preheating was not applied in order to prevent substrate temperature from reaching its glass transition temperature (180 °C) and curing temperatures (177 °C) during deposition. The composite begins to transit from a hard and glassy state into a soft and rubbery state when its temperature exceeds glass transition temperature, and the outcome will be the detachment of the steel wire from the composite part (Figure 3.5). Instead of preheating, the composite was cooled down during all coating depositions using two air blowers to reduce the substrate surface temperature as low as possible and under (177°C), which is the maximum composite service temperature.

An average 90 µm thickness coating was achieved by 6 passes of the spraying process. Figure 3.8(a) shows the microstructure of the APS martensitic stainless steel coating on steel mesh-composite substrate showing that the steel mesh layer has enough potential to create a strong bond between the coating layer and the substrate. This ability is related to the wire mesh type, wire mesh diameter, and open areas. The structure of the APS martensitic stainless steel coating cross-section on grit blasted mild steel is shown in Figure. 3.8 (c). Again, the coating microstructures on both substrates are similar to each other. The optimized surface preparation of the 200 steel mesh

increases the substrate surface roughness and helps the molten particles to lock into the mesh and completely adhere to the composite surface.

Repeatedly, the matter of the higher oxidation and porosity produced in the APS process is still relevant to the case of chromium stainless steel. In this case,  $\text{Cr}_2\text{O}_3$  can be formed during spraying [75]. It was also known that stainless steel coatings produced by arc spray and flame spray shows oxidation and porosity comparable to plasma spray and HVOF processes in their microstructures [76]. By assessing the SEM image of stainless steel coating in Figure 3.8 (b) through EDS analysis, different parts of the coatings were investigated where the white areas are the metallic phase, gray areas are the oxide phases, and black spots are pores. The coating appears to have a high percentage of oxide content and a high number of pores. The surface roughness of the produced stainless steel coating was measured at  $12.5 \mu\text{m}$ .



**Figure 3.8:** Cross-sections of stainless steel coatings on composite substrate with (a) optical image at low magnification and (c) optical image at high magnification (b) SEM image at high magnification. (d) on grit-blasted mild steel sample.

### 3.3.3. Analysis of alumina 3 wt. % titania APS coating

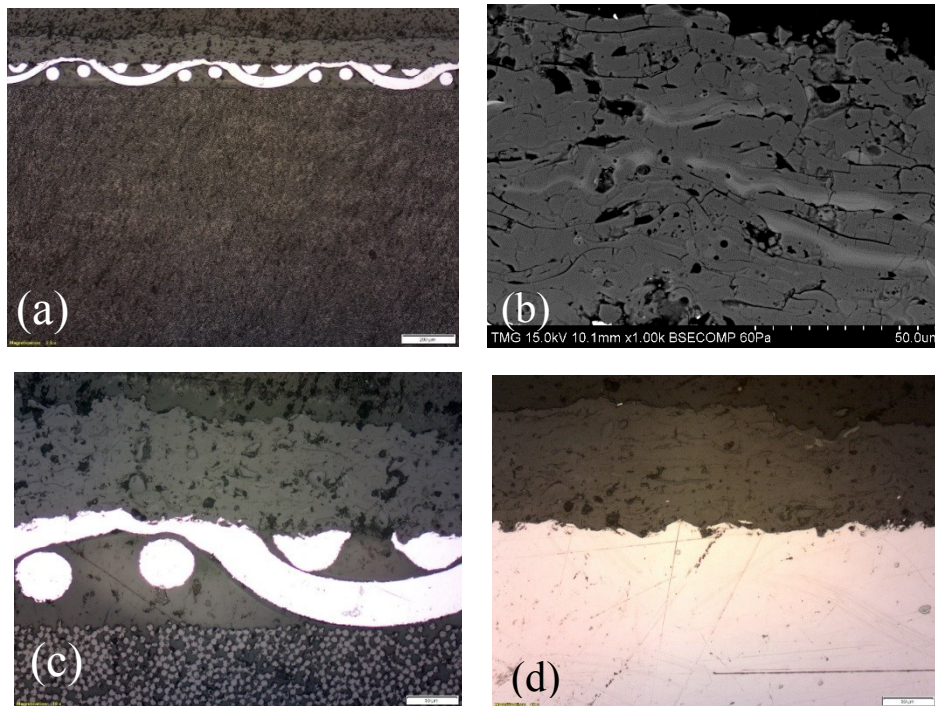
In the last coating experiment, alumina 3 wt. % titania ceramic powder with  $-45 +11 \mu\text{m}$  size distribution and angular-blocky morphology was plasma sprayed on the steel mesh composite

substrate. Since alumina is a metallic oxide powder and has already been oxidized, the matter of oxidation in atmospheric plasma spray will not occur, which will assist with producing dense, smooth coatings with good wear resistance, friction and abrasion properties. It also makes APS one of the suitable processes for coating this type of powder. In addition, compared to martensitic stainless steel and tungsten carbide 20 wt. % cobalt, Metco 101NS coating comes at a much lower price with the advantage of electrical insulation and dielectric properties [61]. Like the other two powders, the feed rate powder for  $\text{Al}_2\text{O}_3\text{3TiO}_2$  was decreased from 53 to 21 g/min, which resulted in a very uniform thickness deposition coating with no sign of damage to the composite matrix and fibers or peeled off of the coating or steel mesh cloth from the composite substrate. The feed rate of all three powders can have some tolerance in their coating process, which does not really affect their microstructure.

According to the previous study by Rahimi [4] related to the steel mesh layer, there are many types of mesh with different open areas and different wire diameters like steel mesh 400, which was found to provide lower bond strengths with the coating layer. As for steel mesh 200, the holes between the mesh wires were emerging at the surface after the grit blasting and provide an important effective open area on the surface for molten particles to bond well with the composite substrate. After six passes of spraying, an average thickness of 115  $\mu\text{m}$  with a surface roughness of 8.2  $\mu\text{m}$  was obtained.

In general, other factors like substrate roughness, substrate temperature, and coating thickness can alter the properties of the coating, which ultimately could change the erosion resistance of the coatings. The alumina coatings sprayed on the PMC substrates are significantly more porous than those sprayed on the mild steel samples as shown in Figure 3.9. Due to the presence of the mesh and the grit blasting process, the surface roughness of the PMC substrates is enhanced considerably, which resulted in an increase of the coating porosity. It has been reported that the highest hardness, the lowest porosity, and the lowest coating roughness values were achieved at substrate roughness of 3.28  $\mu\text{m}$  and a coating thickness of 100  $\mu\text{m}$ , which are close to our investigation results [77]. From the cross-section of alumina 3 wt. % titania microstructure in Figure 3.9(a), it can be seen that the coating layer has a lamellar solidified structure parallel to the interface of the mesh. This structure was formed as a result of the impact, deformation, and solidification of the melted particles on the surface. In plasma spraying of  $\text{Al}_2\text{O}_3\text{3TiO}_2$  coating,

TiO<sub>2</sub> will partially melt and help the Al<sub>2</sub>O<sub>3</sub> particles to adhere better to the surface [78]. The Al<sub>2</sub>O<sub>3</sub>3TiO<sub>2</sub> was also coated on mild steel for comparison which appears denser than the coating spray of the composite substrate (Figures 3.9 (c) and (d)). In EDS analysis of the coatings, the composition of the gray and white areas are not significantly different, and it seems that those white areas are partially molten particles in the structure (Figure 3.9 (b)).



**Figure 3.9:** Cross-section of Al<sub>2</sub>O<sub>3</sub>3TiO<sub>2</sub> coating on composite substrate with (a) low magnification and (b) high magnification (c) SEM image of the coating on a composite mesh sample (d) grit-blasted mild steel sample after coating at high magnification.

### 3.4. Solid particle erosion resistance of the different coatings and CFRP

In general, the ASTM G76 standard allows variations from the recommended conditions, as long as these are noted (section 12.3). Many testing conditions can influence the erosion behavior of the material, such as the velocity and feed rate of the erodent particles and also the distance between the nozzle and the sample. According to the ASTM G76 standard, the feed rate of the erodent particles should be 2 g/min, which in this experiment it was taken as 1 g/min, and also the distance between the nozzle and the sample should be 10 mm, but using the current setup it was taken as 20 mm. The reason for the increased working distance is practical. Extra space is required

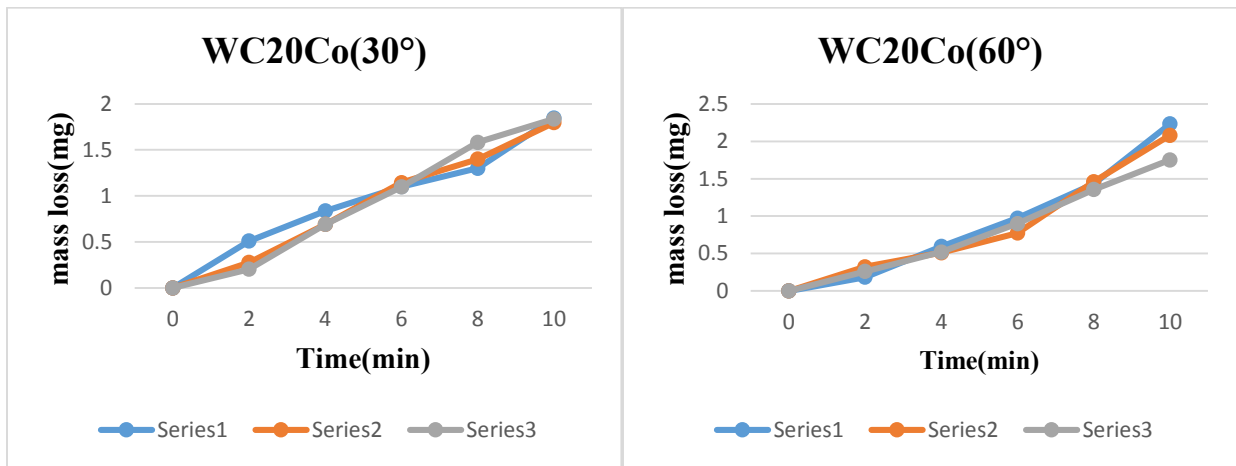
to have room for the shutter between the nozzle and the sample (especially at low impact angles). However, when the working distance is increased, better flow rates will create artificially low erosion rates. That being said, if the feed rate increases simultaneously with the working distance, then there is a better chance that incoming particles will actually collide with particles that are rebounding off of the surface. In order to approach the standard condition, the distance and feed rate were set in 20 mm and 1.0 g/min, respectively.

### **3.4.1. Investigation of tungsten carbide 20 wt. % cobalt erosion mechanism**

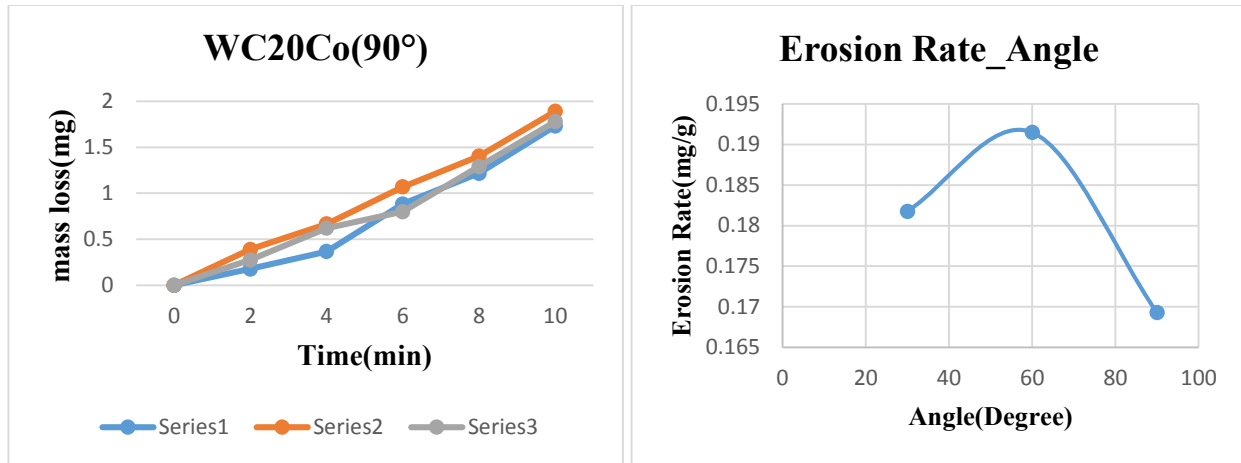
Results in a study carried out by Z. Geng et al. [79] indicate that the WC phase in low-pressure plasma spray WC12Co coating goes through decomposition, oxidation, and decarburization, which results in producing the brittle  $W_2C$  phases, W atoms, and CO/CO<sub>2</sub> gas. As discussed in the previous section, brittle W-rich binder phases will be formed by dissolving tungsten into the binder phase. Additionally, the cobalt binder phase will be melted and oxidized during spraying. Moreover, during the splats solidification process, the binder phase holding tungsten and cobalt may shift into the extensive amorphous phase because of the rapid solidification. Also, the CO/CO<sub>2</sub> gas could produce more pores and cracks in the structure of the coatings [79]. The existence of the pores will affect the erosion property in many ways, such as weakening the WCCo strength against plastic deformation or chipping due to the absence of mechanical support at the edge of the voids and also can become the center of the impact stress [80].

All the mentioned conditions will alter by expanding the quantity of the cobalt in the tungsten carbide compound. In the thermal spraying process of LPPS WC17Co coating, the higher amount of cobalt protects the WC phase in the powder against encountering more reaction. The coating structure of WC17Co is denser with fewer pores or cracks in comparison to the WC12Co structure coating. In fact, higher cobalt content of LPPS WC17Co coating resulted in having many larger WC particles with fewer brittle W-rich binder phases and less porosity and micro-cracks. Furthermore, the cobalt can reduce the rate of oxidation and retain the load-bearing capacity of the coating, which ultimately provides better hardness and toughness in the coating than that of the LPPS WC12Co coating. As a result, the wear resistance of tungsten carbide will grow with a higher number of cobalt in its structure [79]. So far, tungsten carbide powder with the highest amount of cobalt manufactured in the market is tungsten carbide with 20 wt. % cobalt, which apparently is an optimum combination of hardness and toughness of the cobalt binder [81].

To investigate the effectiveness of the coating on the polymer composites, erosion experiments were performed by hitting the samples at different angles. In Figure 3.10 (a) and (b) and in Figure 3.11 (a), the mass loss portion of WC20Co coating in 10-minute period is shown at three different angles 30°, 60° and 90°, respectively. The samples did not show any incubation (negative or zero mass loss) period, and the results of three repetitions are similar to each other within a small margin. After calculating weight loss per unit weight of erodent at each angle, the erosion rate was maximum at angle (60°) and it reduced at a low-impingement angle (30°) and perpendicular angle (90°) (Figure 3.11 (b)). Regardless of the type of thermal spray coating, WCCo coatings have demonstrated a brittle behavior in their structure. However, in this research, it seems that the erosion behavior of WC20Co is similar to semi-ductile materials. Comparing the results at (90°) and (30°) (E90/E30) is a good way to assess the erosion mechanism of materials. Regarding WC20Co, the ratio  $E_{90}/E_{30} < 1$  indicates the shear deformation by the particle impacts caused the formation of lips/protrusions at oblique angles such as (30°). In addition, the high percentage of cobalt in the coating provided enough ductility at 90-degree angle, which contributed to the reduction of its erosion rate compared to the erosion reported at 60° degrees.



**Figure 3.10:** Mass loss of CFRP samples coated with WC20Co tested at (a) 30° and (b) 60°.



**Figure 3.11:** (a) Mass loss of CFRP samples coated with WC20Co tested at 90° and (b) Erosion rate of WC20Co samples as a function of impingement angle.

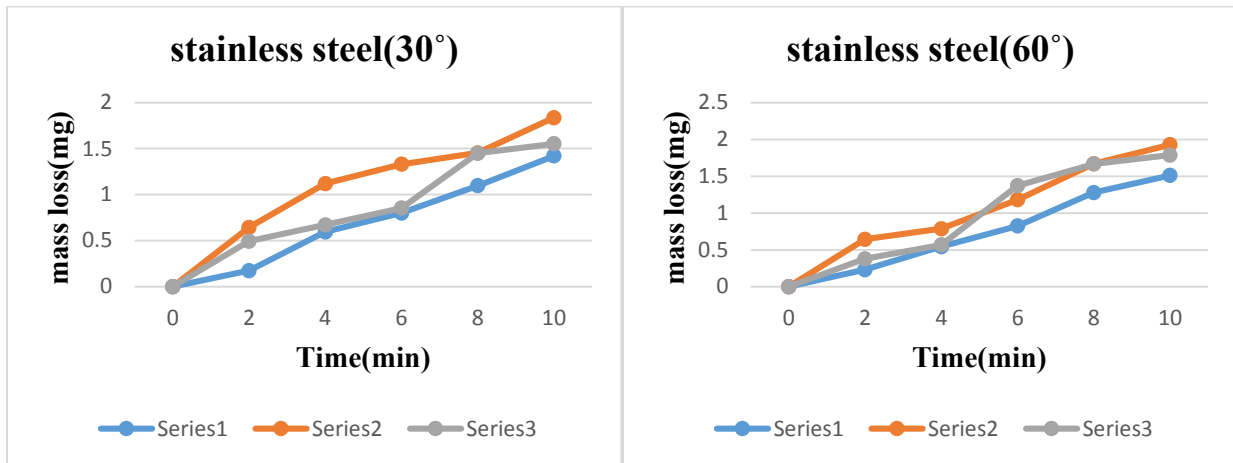
### 3.4.2. Investigation of martensitic stainless steel erosion mechanism

The Diamalloy 1002 powder used in this investigation has the same composition of 420 stainless steel, which is categorized in 400 Series martensitic stainless steels. On the other hand, 300 Series stainless steels are classified as austenitic stainless steels. The 400 series group of stainless steels has a range of 12-14 percent chromium and 1-percent of manganese, which 3 percent less and 1 percent above the 300 series group, respectively. The 400 series of stainless steels have martensitic crystalline structure due to higher carbon content in their structure, which provides higher strength and wear resistance. Martensitic stainless steels are not as corrosion resistant as the austenitic types and cannot maintain their strength at high temperatures. Diamalloy 1002 thermal spray coatings show similar properties, which make them advantageous for particle erosion resistance (at low temperature) and dimensional repair of steel parts like exhaust fans, hydroelectric valves [61]. Several studies related to dry or slurry erosion resistance of different metallic materials have been carried out before considering the erosion mechanism of this material and its performance. It was observed that at an impact angle of 30°, the AISI 410 martensitic stainless steel presents a higher rate of volumetric erosion and, conversely, a better resistance to jet slurry erosion at an impact angle of 90° with the compromise of a deeper eroded area [82]. In another study, a silicon carbide (SiC) particle erosion test was performed on different types of metals at four different incident angles (30°, 45°, 60°, 75°, and 90°). Wear mechanisms of two types of 300 grade (AISI 304, AISI 316) and one 400 grade (AISI 420) stainless steel were compared



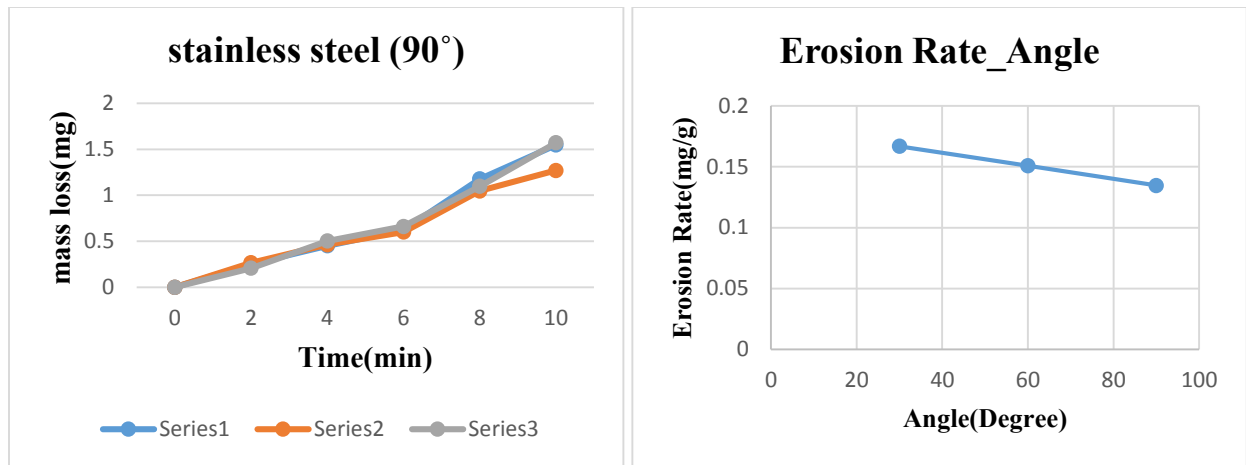
with each other, and it was found that AISI 420 stainless steel maintains higher resistance against particle impacts than that of the two other materials [27].

In Figure 3.12 (a) and (b) and in Figure 3.13 (a), the mass loss portion for martensitic stainless steel coating after 10 minutes is shown at three angles of 30°, 60° and 90°, respectively. As observed for the WC20Co coating, the stainless steel coated samples did not have any incubation (negative or zero mass loss) period. The results of three repetitions at 60° and 90° are similar to each other within a small margin. However, there is some dispersion in the results at 30°. The ratio of E90/E30 is less than 1 indicating a ductile behavior of the stainless steel coating as reported for bulk 420 stainless steel compound. The erosion rate was maximum at an oblique angle of 30° and it decreased with increasing the angle of impact. The minimum weight loss per unit weight of erodent occurred at 90° (Figure 3.13 (b)).



**Figure 3.12:** Mass loss of CFRP samples coated with martensitic stainless steel tested at (a) 30° and (b) 60°.



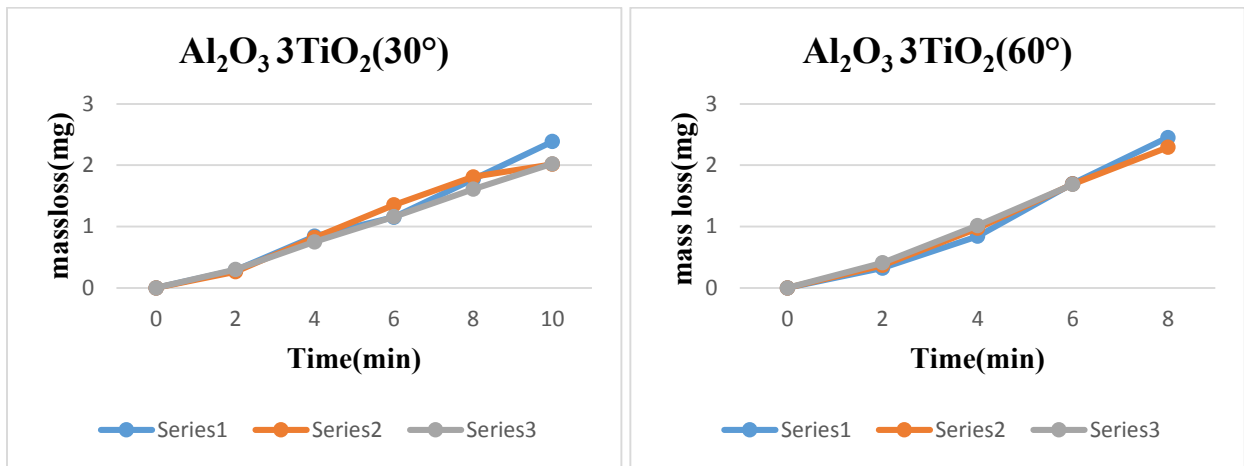


**Figure 3.13:** (a) Mass loss of CFRP samples coated with martensitic stainless steel tested at 90° and (b) Erosion rate of martensitic stainless steel samples as a function of impingement angle.

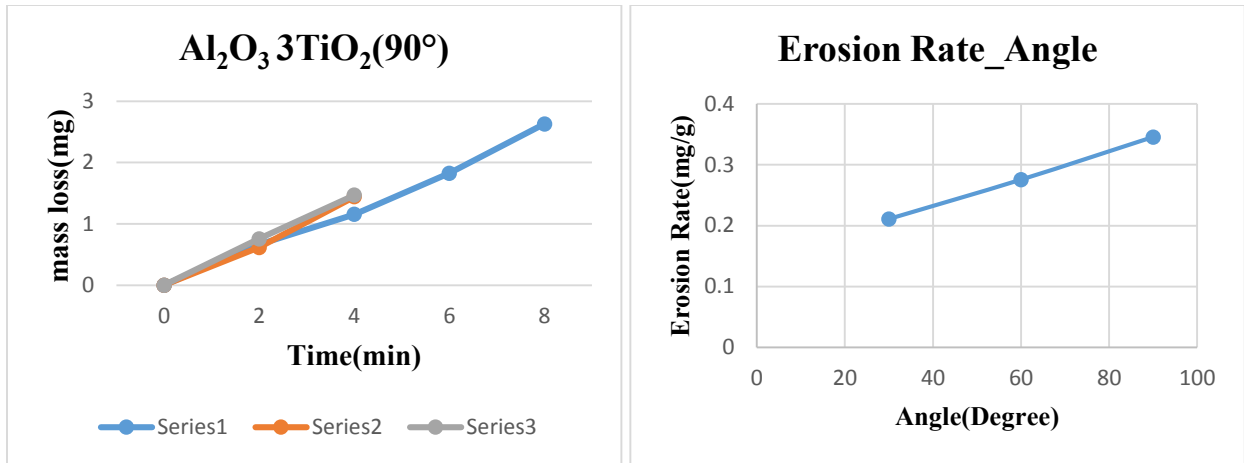
### 3.4.3. Investigation of alumina 3 wt. % titania erosion mechanism

Solid particle erosion behavior of materials is highly affected by many experimental factors like type, size, and velocity of particles, impact angle, surface characteristics, and materials properties. In general, the structure of thermal spray coatings has porosity. As mentioned before, many parameters such as the surface roughness of the substrate, spraying distance, initial temperature of the substrate, and coating thickness can alter the percentage of the porosity in the structure [83, 84]. Previous studies have shown that the porosity content goes up with increasing the amount of  $\text{TiO}_2$  [85] and will weaken the structure of the coating against erosion environment. For this reason,  $\text{Al}_2\text{O}_3$  with 3%  $\text{TiO}_2$  was chosen in this research to be coated as a ceramic material. The structure of ceramic plasma sprayed coating includes a large number of overlapped splats and the bonding strength is weaker at the lamellar interfaces. In plasma-sprayed ceramic coating, one of the main reasons for erosion is the failure of the individual splat boundaries [86,87]. Furthermore, both  $\text{Al}_2\text{O}_3$  and  $\text{TiO}_2$  are ceramic materials with brittle behavior. When the erodent particles impact with the surface of the  $\text{Al}_2\text{O}_3/3\text{TiO}_2$  coating, radial and central cracks will grow at the impact area. Upon rebounding of the impacting particles, lateral cracks grow parallelly to the surface and finally follow a curved path before propagating to the surface, which leads to chipping and loss of material. For that reason, the fracture of brittle ceramic splats is also contributing to the erosion of the plasma sprayed ceramic coating. The failure mode of plasma sprayed traditional ceramic coatings is dominated by spalling and fracture [88].

The same particle erosion process was applied on  $\text{Al}_2\text{O}_3\text{3TiO}_2$  coated samples at three angles, and the results are reported in Figure 3.14 (a) and (b) and in Figure 3.15 (a). Same observed with the other coatings,  $\text{Al}_2\text{O}_3\text{3TiO}_2$  coated samples did not show any incubation (negative or zero mass loss) period. The results of three times repetition at  $30^\circ$ ,  $60^\circ$  and  $90^\circ$  are similar to each other within a small margin. At 90 degrees, two samples failed and the coating was removed by the erodent particles after 4 minutes while the third sample resisted until 8 minutes. However, the erosion results of these three samples at a 90-degree angle are close to each other with a small margin. At 60 degrees, one sample failed after 6 minutes and the other two failed after 8 minutes. Again, the graph slopes of these three samples are very similar indicating a good reproducibility in the observed erosion rates. It is important to reposition correctly in the test chamber after each weight measurement. Otherwise, the erodent particles do not impact the same region on the sample surface and an accurate time of failure is not obtained. The difference between the times of failure of the  $\text{Al}_2\text{O}_3\text{3TiO}_2$  samples can be related to this issue. The ratio of  $E_{90}/E_{30}$  is higher than 1, which shows that the erosion failure mechanism is mainly brittle erosion for these alumina coatings. The erosion rate was minimum at an oblique angle of  $30^\circ$  and it increased with the increasing angle. The maximum weight loss per unit weight of erodent occurs is reached at an angle of  $90^\circ$  (Figure 3.15 (b)).



**Figure 3.14:** Mass loss of CFRP samples coated with alumina 3 wt. % titania tested at (a)  $30^\circ$  and (b)  $60^\circ$ .

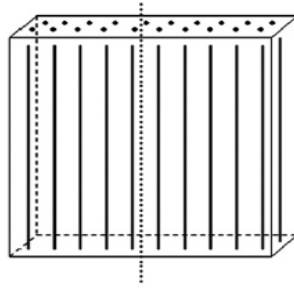


**Figure 3.15:** (a) Mass loss of CFRP samples coated with alumina 3 wt. % titania tested at 90° and (b) Erosion rate of alumina 3 wt. % titania samples as a function of the impingement angle.

### 3.4.4. Investigation of CFRP erosion mechanism

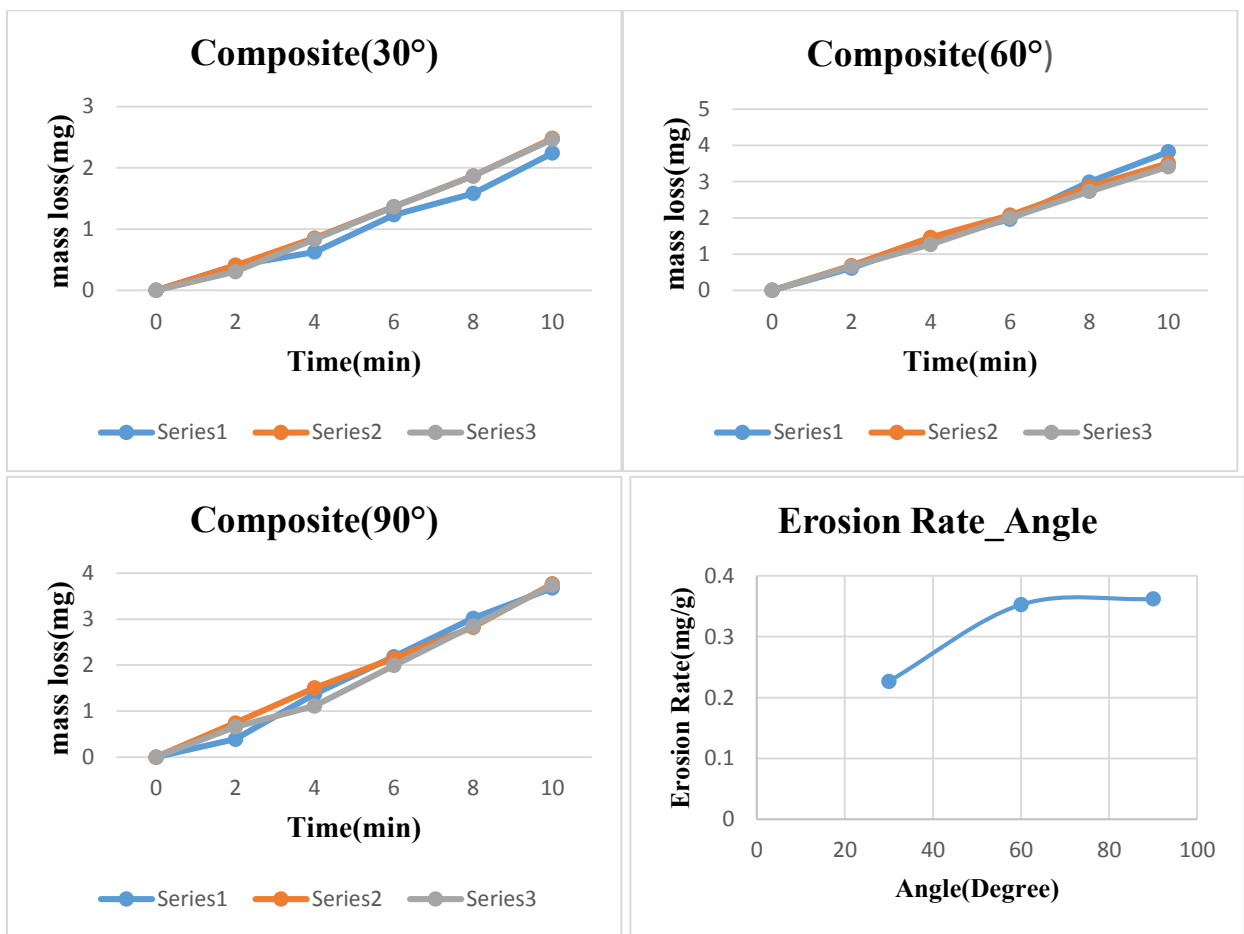
Unidirectional carbon fiber composite materials are more desirable for erosion resistance application compares to glass fiber composite materials [36]. Suresh et al. observed that the erosion rate at oblique impact angles would significantly be affected by the orientation of the fibers. They also showed that the erosion rate would increase when the particles impact perpendicularly compared to parallelly to the direction of the fibers [89]. For fabrics, two types of erosion mechanisms modify the arrangements of fibers in the warp and weft directions of the composite materials: (a) plowing along the impact direction, (b) shearing normal to the impact direction [90]. In fiber composite materials, fiber thinning, fiber detachment, and cavities due to fiber loss will occur because of sequential exposure of fibers to erodent particles at high impact angles [90].

In this study, the composite substrate was exposed to the erosion conditions in the perpendicular orientation of the carbon fibers (Figure 3.16). In Figure 3.17 (a), (b), and (c), the mass loss portion for carbon fiber reinforcement composites after 10 minutes is shown for at angles of 30°, 60° and 90°, respectively. The results of the three repetitions at all angles are similar to each other within a small margin.



**Figure 3.16:** Schematic diagram of the composite sample in perpendicular CFs orientation in the erosive wear tests.

The weight loss per unit weight of erodent was low at a low-impingement angle ( $30^\circ$ ) and high at an impingement angle ( $60^\circ$ ). The peak erosion rate took place at a high impingement angle ( $90^\circ$ ), which indicates a brittle erosion behavior (Figure 3.17 (d)) related to the presence of the brittle fibers in the PMC.



**Figure 3.17:** Mass loss of unidirectional CF/Epoxy samples tested at (a)  $30^\circ$  and (b)  $60^\circ$  (c)  $90^\circ$  (d) Erosion rate of CF/Epoxy samples as a function of impingement angle.

### 3.4.5. Comparison between the erosion resistance of different substrates

The influence of the impact angle on the solid particle erosion rates of the three coatings and composite substrate altogether is shown in Figure 3.18. Clearly, the coated surfaces were able to protect the composite substrate from getting damage and reduce significantly the erosion rate. However, between the coated surfaces, due to the large densities difference between the three coating materials and composite substrate, the mass loss data is not the best indicator for a comparative analysis of the performance of the different materials. To achieve this comparison, the volume loss within the wear scar was calculated by dividing the erosion rate of each surface per its density (Figure 3.19). This graph indicates that using the proposed manufacturing and processing method and application of either stainless steel or WC20Co coatings can improve the erosion resistance of polymer composites significantly. In order to understand the superiority performance of WC20Co and martensitic stainless steel coatings compared to the alumina coating and the bare composite sample, further investigation regarding the variables affecting the solid erosion test in ductile and brittle materials is necessary.

In solid particle erosion test, three different class of parameters influence the erosion rate (volume loss) of the materials, that is to say, elements related to the particle flow, erodent particles properties and substrate properties. The particle flow related elements are the particle velocity  $\omega_p$ , angle of impact  $\alpha$  and particle concentration. The main erodent particle properties are particle density  $\rho_p$ , particle shape, particle size  $R_p$ . Substrate properties include all coating and substrate mechanical properties such as Young's modulus  $E_t$  and Poisson's ratio  $\nu_t$ , hardness  $H_t$  and fracture toughness  $K_{Ct}$  [91]. The relations of the volume loss and the above-mentioned variables in brittle and ductile materials can be assessed by using various theoretical predictive methods. Primarily, it is essential to determine the true nature of each substrates. In many studies, the impact angle was identified as the most important parameter in identifying the erosion mechanism. In the previous section, it was shown that the alumina coating and uncoated CFRP had brittle behaviors. Stainless steel coating showed ductile behavior and WC20Co coating appears to have semi-ductile behavior. As the main phase in the WC20Co coating is WC which is a brittle material, the analysis of the volume loss of this coating as well as the alumina coating is done based of the following formula for brittle behavior [91]:

$$V \propto \omega_p^{e1} R_p^{e2} \rho_p^{e3} K_{It}^{e4} H_t^{e5} E^{e6} \quad (3.1)$$

where the  $K_{It}$  is the fracture toughness of the substrate,  $E$  is the elastic constants and the exponents  $e_i$  varies depending on the different theories. In all models,  $K_{It}$  is considered to be the most effective parameter among all the variables influencing the volume loss. The erosion mechanism of ductile materials is different from the erosion mechanism of brittle behavior. In brittle materials, erosion occurs due to cracking and chipping. Consequently, the erosion is significantly influenced by the toughness of the material. On the other hand, the hardness effect on amount of volume loss appears to be small in all models. In all models, Equation 3.1 predicts that the volume loss reduces with increasing the fracture toughness [91]. Typically, particles and test parameters are constant in each coating solid particle erosion experiment and that helps in clarifying the real influence of the materials properties. Between the uncoated composite substrate, alumina and WC with zero percent cobalt, the carbon fiber reinforcement composite has the smallest fracture toughness. Alumina coating with 3% TiO<sub>2</sub> also has a lower fracture toughness compared to tungsten carbide. By adding cobalt to the WC structure, the fracture toughness of the cermet starts to growth and its hardness starts to fall [92]. This can be one of the justifications of huge difference between the erosion rate of uncoated composites and the WC20Co coated samples.

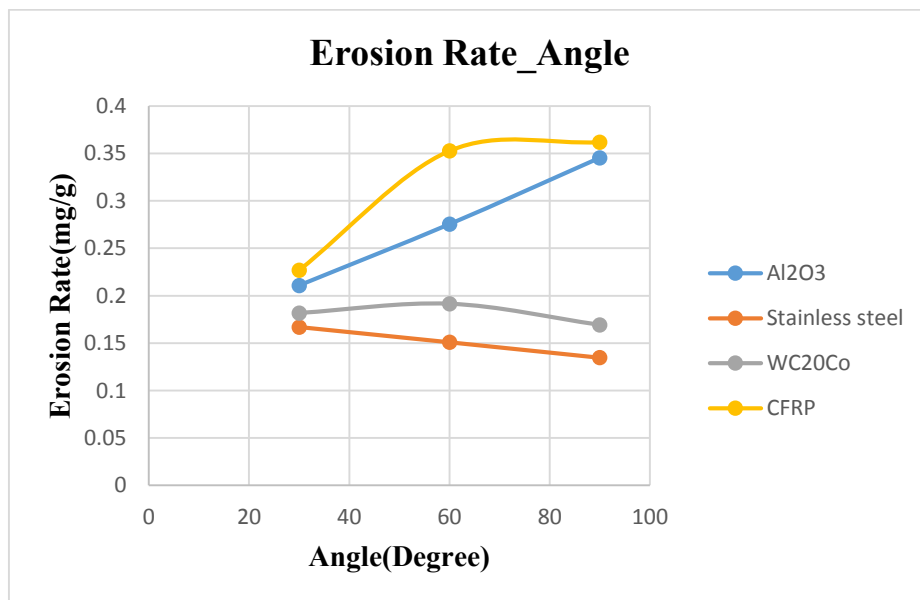
The erosion mechanisms of ductile materials comprise micro extrusion, forging, and fracture steps and among them, the most important mechanism is the plastic deformation. The Bitter (1963) model, which represents the total volume loss of material, is the summation of the plastic deformation material lost for  $V_D$  (the surface layer is destroyed after reaching the elastic limit of material and its fragments) and the cutting lost for  $V_C$  (the particle impact scratches out some parts of the material from the surface). In case of equality of the energy needed to remove a unit volume by cutting and the energy requires to remove a unit volume of material by means of plastic deformation, the total volume lost is given by Equation 3.2 [93]:

$$V_e = V_c + V_d = \left(\frac{M_p \omega_p^2}{2}\right) / F\Omega \quad (3.2)$$

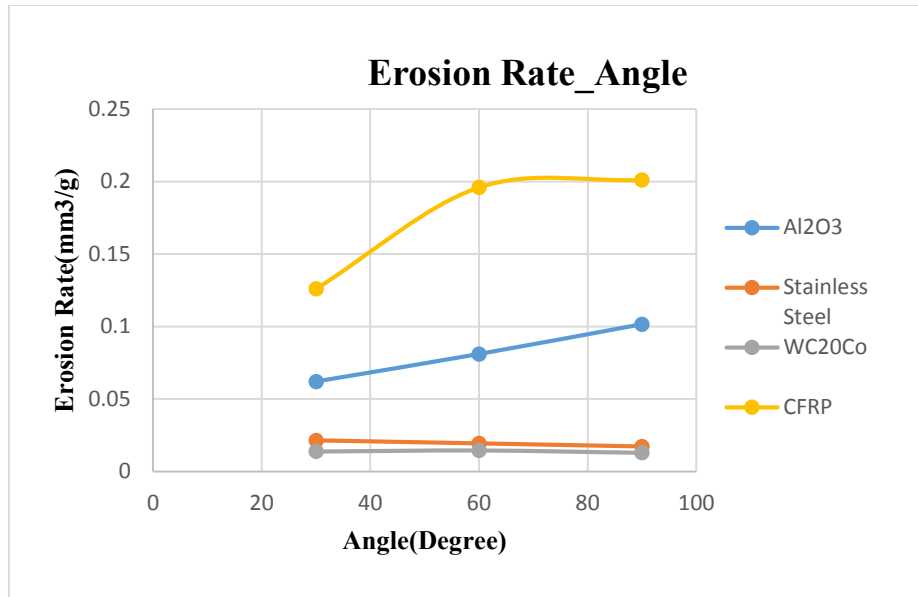
where  $M_p$  is particle mass and  $1/F$  is the fraction of the initial kinetic energy, which contributes to the erosion and  $\Omega$  is the energy requires to remove a unit volume of material by means of plastic deformation. In order to quantitatively obtain the volume lose, determination of  $F\Omega$  from the

erosion tests is needed. Equation 3.2 shows that the volume loss analysis of ductile materials depends on several constants, which need to be determined experimentally. In addition, the combination of  $F\Omega$  is influenced by the Poisson's ratio and Young's modulus of the substrate and coating materials [91]. As successfully illustrated in the previous section, martensitic stainless steel coating is considered to be a ductile material and, according to the above theory, its volume loss depends on the solid particle erosion conditions and coating properties. Martensitic stainless steel performed significantly well in this investigation and was able to compete with WC20Co due to the fact that erodent particles of our solid particle erosion test possess low mass and were applied at a relatively low velocity.

It appears that using the CFRP as a substrate compared to other hard substrates like metal or mild steel can be an important factor influencing the performance of these coatings against particles impact. For example, in brittle coatings like  $Al_2O_3TiO_2$ , in order to resist more against erosion, the support of the hard substrate is required which was not provided by this type of substrate. It is worth to note that the metal mesh is imbedded in a soft epoxy resin in the current investigation. Such an epoxy resin is expected to be too soft to provide a strong support to the alumina coating upon impact by the erodent particles.



**Figure 3.18:** Erosion rates (mg/g) of test samples as a function of the impingement angle



**Figure 3.19:** Volumetric erosion rates (mm<sup>3</sup>/g) of test samples as a function of the impingement angle

### 3.5. Results of hardness measurements

Results of surface micro-hardness measurements of the tested samples are listed in Table 3.2, with the average of five readings for each sample. In this table, the name of each sample is composed of two letters. The first letter identifies to coating material, and the second letter the substrate material. For example, A-S stands for Al<sub>2</sub>O<sub>3</sub>TiO<sub>2</sub> coating on mild steel substrate and C stands for composite. In order to better determine the hardness of each material and obtain more accurate data, the hardness of each coating was measured on mild steel substrate, and subsequently, results with less variability were conducted. The reason for the differences between the micro-hardness results on the composite substrate can be related to the presence of the wire mesh layer and resin with low stiffness.



**Table 3.2:** Results of micro-hardness measurement of different samples

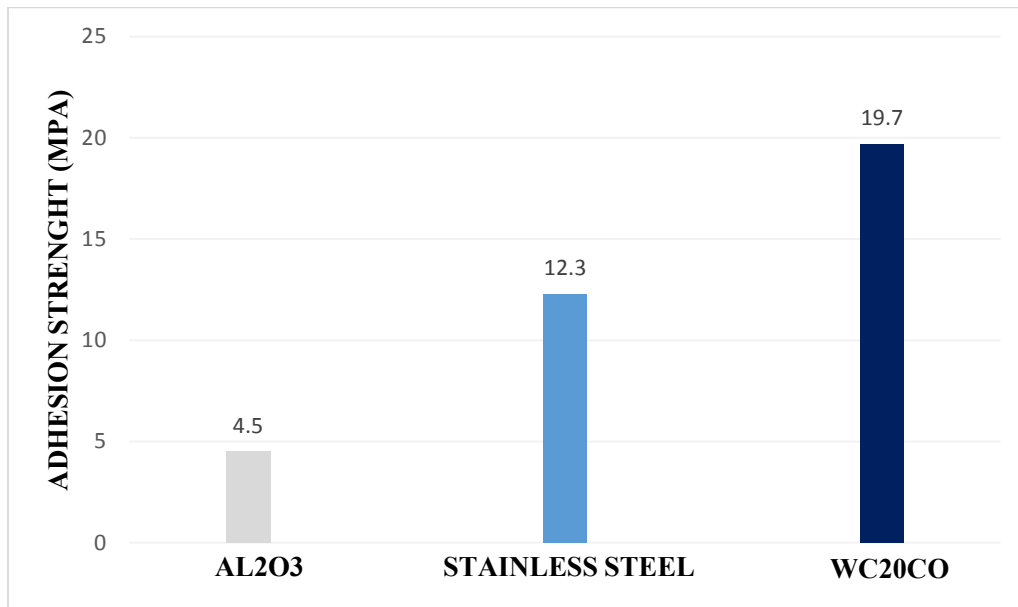
Sample Type	Surface Microhardnes (HV)					
	R1	R2	R3	R4	R5	Ave.
W-C	512.0	492.4	491.2	505.3	519.6	504± 6
W-S	583.2	547.9	551.9	555.4	548.4	557± 7
S-C	275.5	260.8	259.6	263.2	271.6	266± 4
S-S	299.9	293.2	312.2	305.2	301.7	302± 4
A-C	521.5	511.2	520.0	522.3	514.8	517± 2
A-S	515.3	515.4	510.3	513.9	519.1	514± 2

### 3.6. Adhesion strength

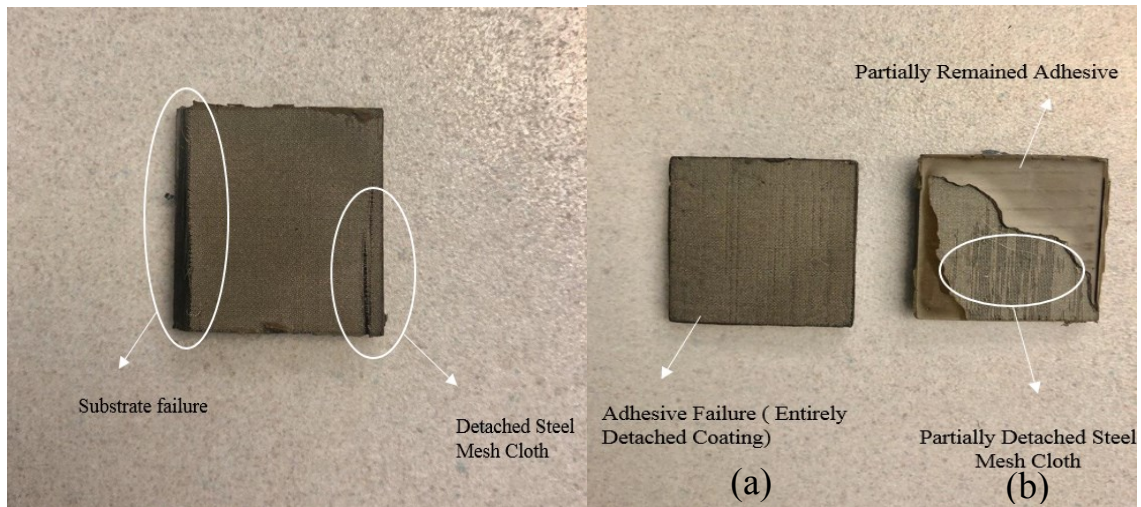
The bond strengths of the three types of coatings were measured. Flatwise tensile testing was performed to identify the failure characterization of each coating with respect to different adhesive and cohesive failures. According to ASTM C-633 standard, there are three types of failures in adhesion tests. If the failure occurs completely at the coating-substrate interface, the adhesion strength of the coating is measured. If a fracture happens within the coating layer, the cohesion strength of the coating is measured. The last failure is a combination of the mentioned failures, and, often time, no explanation of the initial cause can be given. In coating adhesion testing, substrate failure is not generally considered as a failure mechanism [94].

In a study carried out by Lima and Trevisan [95], the authors reported that the coating thickness and the number of coating passes could influence the adhesion strength of the coatings. In their observation, the adhesion strength tends to decrease by increasing the coating thickness and number of coating passes for the same thickness. The reason for this behavior can be related to the residual stresses, which can induce more driving force and facilitate the interface crack propagation in thicker coatings [95]. It was also reported by Khan et al. [96] that coating adhesion enhancement can take place by increasing the substrate roughness (or bond coat surface roughness for a ceramic top-coat) up to a certain point (about 5  $\mu\text{m}$  in their work) and then reduces.

The results of adhesion tests are illustrated in Figure 3.20. The tests were repeated three times to determine the reliability of the results. Three factors were mentioned as effective parameters in the adhesion property of the coating. The number of passes was the same for all three coatings. However, in the case of  $\text{Al}_2\text{O}_3\text{TiO}_2$  coating, the thickness was higher (average of  $115\ \mu\text{m}$ ), which could be one of the reasons for having a lower adhesion bonding compared to the other two coatings. The substrate roughness was increased due to the wire mesh utilization in the composite structure promoting a high coating adhesion. In this research, there was a noticeable time gap between the surface preparation of the samples and coating process, which is a disadvantage and reduced the freshness of the surface to bond strongly with the splats of the coatings. The samples were examined after failure to assess the failure mechanism. Different types of failure mechanisms are shown in Figure 3.21. The average adhesion strength of the  $\text{Al}_2\text{O}_3\text{TiO}_2$  coating was 4.5 MPa, which is a decent number for a ceramic coating without a bond coat [97]. WC20Co coating demonstrated the highest adhesion strength, which shows strong compatibility of this material with the wire mesh and the substrate. Results show that there is a good adhesion between the composite and the coating which is due to the presence of metal wire mesh.



**Figure 3.20:** Adhesion strength results of the coated samples.



**Figure 3.21:** Failure mechanism of the coated samples, left) substrate failure, right) (a) adhesive failure (b) adhesive and cohesive combination

## 4. Conclusions, contributions, and future work

### 4.1. Conclusions and contributions

The process development and fabrication of three metallic coating layers for erosion resistance application on polymer-based carbon composite materials was successfully performed. Atmospheric plasma spray was utilized to spray a uniform and high-quality coating layers on the top of a carbon fiber reinforced polymer CFRP sample without damaging or burning the composite part.

The following steps were taken to achieve these goals:

1. **Sample manufacturing and proper surface modification and preparation:** Composite panels with a metal mesh imbedded in their surfaces were manufactured using hand layup and autoclave curing. The steel wire mesh approach showed promising results in creating strong bonding with the composite substrate and the coating layer. It was shown that, without proper surface preparation, the steel wire mesh usage was ineffective due to the fact that the whole mesh is covered with epoxy of the composite substrate. A grit blasting procedure is thus necessary to expose the mesh surface and get it prepared to be coated. In addition, the roughness of the surface and the low free surface energy of the composites increased by adding an extra mesh layer to their structure, which was crucial to producing strong adhesion bonding with the coating.
2. **Optimizing the thermal spray parameters with respect to composite substrate vulnerability:** The composite materials, especially fibers, are sensitive to high-velocity particle impacts and they usually have low service temperature. In this research, the atmospheric plasma spray process was able to produce molten spray particles impinging on the composite substrates forming a uniform layer for all three powders without damaging the composite. However, spray parameters needed to be optimized to achieve such coatings. In this work, spray parameters for coating the composite substrates were selected based on the prevention of any damage to the substrate or the wire mesh and to reach an acceptable level of deposition efficiency. Setting an appropriate cooling system for managing the temperature of the composite substrates was applied. The microstructures of coatings sprayed on the mild steel and composite samples were compared and it was shown that they present similar behavior, which validates the usage of wire mesh in the composite structure.

3. **Cross-sectional examination and mechanical characterizations:** Cross-sectional micrograph analysis was performed to study the effect of metal mesh and the quality of different coatings. It was observed that the metal mesh is completely covered with resin after manufacturing and was partially removed during the grit blasting. Depending on the coating materials and process conditions, some pores in the coating were observed which is normal for these types of coatings. Micro-hardness test and flatwise tensile test were performed to evaluate the performance of the coatings on carbon fiber polymer composites. Hardness test indicates that a comparable hardness can be achieved in coatings sprayed on the composite or low-carbon steel substrates. Flatwise tensile test was performed to measure the adhesion between the composite substrate and coating. Samples were examined to identify the failure mechanism and to select the right experimental data for the analysis. The results of the coating adhesion test proved that the coating was well adhering to the wire mesh layer, especially in the case of WC20Co.
4. **Erosion performance:** The main objective was to improve the erosion resistance of carbon fiber reinforced polymer. Solid particle erosion resistance test was performed following ASTM G76 standard. All coatings were able to protect the composite during the solid particle erosion test and extend the lifetime of composites against erodent particles. The results indicate that WC20Co has the best results compared to Al<sub>2</sub>O<sub>3</sub>3TiO<sub>2</sub> and stainless steel. It was interesting to see semi ductile behavior in WC20Co coating, which can be related to the higher percentage of cobalt in WC20Co structure. With respect to existing theoretical models for volume loss prediction of ductile and brittle materials, the results of this investigation provide evidence of the good performance of the WC20Co compared to Al<sub>2</sub>O<sub>3</sub>3TiO<sub>2</sub> and carbon fiber reinforcement composite samples. Furthermore, the results showed a satisfactory performance of martensitic stainless steel coatings at low velocity impact with smaller erodent particles.

Finally, it can be concluded that for the proposed manufacturing and processing method and three types of coating materials, WC20Co is the best solution for improving the erosion resistance of polymer composites.

## 4.2. Future work

The findings achieved in this study suggest the following directions for future research:

1. Investigating the performance of using stainless steel mesh cloth to improve the coating deposition efficiency and adhesion of other types of coatings on polymeric materials.
2. Using other metallic coating materials to improve the tribology properties of carbon fiber-reinforced composite in elevated temperature applications.
3. Using other methods of preparation such as chemical treatment to preparing the composite substrates prior to coating deposition process.
4. Using other types of metallic mesh cloths with different materials and different mesh size to improve the coating adhesion strength.
5. Investigating the other applications of a WC<sub>20</sub>Co, stainless steel and Al<sub>2</sub>O<sub>3</sub>3TiO<sub>2</sub> coated carbon fiber reinforcement composites.
6. Investigating the performance of using stainless steel mesh cloth in carved carbon fiber reinforcement composite and evaluates the coating procedure of those structures.

## References

- [1] Handbook, A. S. M. "Volume 21: Composites." *USA: ASM International* (2001).
- [2] Ivosevic, M., et al. "Solid particle erosion resistance of thermally sprayed functionally graded coatings for polymer matrix composites." *Surface and Coatings Technology* 200.16-17 (2006): 5145-5151.
- [3] Pool, K. V., C. K. H. Dharan, and I. Finnie. "Erosive wear of composite materials." *Wear* 107.1 (1996): 1-12
- [4] Rahimi, Alireza. *Thermal Spray Coating of Polymeric Composite Materials for De-icing and Anti-icing Applications*. MSc Diss. Concordia University, 2019.
- [5] Holmberg, Kenneth, and Allan Matthews. *Coatings tribology: properties, mechanisms, techniques and applications in surface engineering*. Elsevier, 2009.
- [6] Williams, John A. "Wear and wear particles—some fundamentals." *Tribology International* 38.10 (2005): 863-870.
- [7] Bayer, Raymond J. *Mechanical Wear Fundamentals and Testing, revised and expanded*. CRC Press, 2004.
- [8] Hutchings, Ian, and Philip Shipway. *Tribology: friction and wear of engineering materials*. Butterworth-Heinemann, 2017.
- [9] Finnie, Iain. "The mechanism of erosion of ductile metals." *3rd US national congress of applied mechanics*. 1958.
- [10] Finnie, Iain. "Some reflections on the past and future of erosion." *Wear* 186 (1995): 1-10.
- [11] Lindsley, B. A., and A. R. Marder. "The effect of velocity on the solid particle erosion rate of alloys." *Wear* 225 (1999): 510-516.
- [12] Ruff, Arthur W., and S. M. Wiederhorn. *Erosion by solid particle impact*. No. NBSIR-78-1575. National Bureau of Standards, Gaithersburg, MD, National Measurement Lab. 1979.
- [13] Hansen, J. S. "Relative erosion resistance of several materials." *Erosion: Prevention and Useful Applications*. ASTM International, 1979.
- [14] Human, A. M., et al. "A Comparison Between Cemented Carbides Containing Cobalt- and Nickel-Based Binders." *Journal of Hard Materials(UK)* 2.3 (1991): 245-256.
- [15] Wittmann, Bernhard, Wolf-Dieter Schubert, and Benno Lux. "WC grain growth and grain growth inhibition in nickel and iron binder hardmetals." *International Journal of Refractory Metals and Hard Materials* 20.1 (2002): 51-60.
- [16] Tarragó, J. M., et al. "Mechanics and mechanisms of fatigue in a WC–Ni hardmetal and a comparative study with respect to WC–Co hardmetals." *International Journal of Fatigue* 70 (2015): 252-257.

- [17] Roebuck, B., et al. "Measurement good practice guide no. 20." *Mechanical Tests for Hardmetals, Centre for Materials, Measurement and Technology, National Physical Laboratory* © Crown Copyright (1999).
- [18] Lassner, Erik, and Wolf-Dieter Schubert. "Properties, chemistry, technology of the element, alloys, and chemical compounds." *Vienna University of Technology, Vienna, Austria, Kluwer* (1999): 124-125.
- [19] Carbide, Cemented. "Sandvik new developments and applications, Ref. no." *H-9116 ENG* (2005).
- [20] Somiya, Shigeyuki. *Handbook of advanced ceramics: materials, applications, processing, and properties*. Academic press, 2013.
- [21] Routbort, J. L., and R. O. Scattergood. "Erosion of ceramic materials." *Key engineering materials* 71 (1992): 23-50.
- [22] Ritter, J. E. "Strength degradation of ceramics due to solid-particle erosion." *Key Engineering Materials*. Vol. 71. Trans Tech Publications Ltd, 1992.
- [23] Sathiyakumar, M., and F. D. Gnanam. "Influence of MnO and TiO<sub>2</sub> additives on density, microstructure and mechanical properties of Al<sub>2</sub>O<sub>3</sub>." *Ceramics international* 28.2 (2002): 195-200.
- [24] KUMARI, SNEHLATA. "Effect of TiO<sub>2</sub> Addition in Al<sub>2</sub>O<sub>3</sub>: Phase Evolution, Densification, Microstructure and Mechanical Properties." *National Institute of Technology, Rourkela* (2013).
- [25] Toro, A., et al. "Corrosion–erosion of nitrogen bearing martensitic stainless steels in seawater–quartz slurry." *Wear* 251.1-12 (2001): 1257-1264.
- [26] Levy, Alan V., and Paul Yau. "Erosion of steels in liquid slurries." *Wear* 98 (1984): 163-182.
- [27] Laguna-Camacho, Juan R., et al. "Solid particle erosion on different metallic materials." *Tribology in engineering* 5 (2013): 63-78.
- [28] Verma, D., et al. "Bagasse fiber composites-A review." *J. Mater. Environ. Sci* 3.6 (2012): 1079-1092.
- [29] Tsuda, Ken, et al. "General method for predicting the sand erosion rate of GFRP." *Wear* 260.9-10 (2006): 1045-1052.
- [30] Ahmed, T. J., et al. "Improving erosion resistance of polymer reinforced composites." *Journal of Thermoplastic Composite Materials* 22.6 (2009): 703-725.
- [31] Harsha, A. P., and Sanjeev Kumar Jha. "Erosive wear studies of epoxy-based composites at normal incidence." *Wear* 265.7-8 (2008): 1129-1135.



- [32] Barkoula, N-M., and J. Karger-Kocsis. "Solid particle erosion of unidirectional GF reinforced EP composites with different fiber/matrix adhesion." *Journal of reinforced plastics and composites* 21.15 (2002): 1377-1388.
- [33] A. Häger, K. Friedrich, Y.A. Dzenis, S.A. Paipetis, Study of erosion wear of advanced polymer composites, in: K. Street, B.C. Whistler (Eds.), Proceedings of the ICCM-10, Canada Woodhead Publishing Ltd., Cambridge, 1995, pp. 155-162.
- [34] Tewari, U. S., et al. "Solid particle erosion of unidirectional carbon fibre reinforced polyetheretherketone composites." *Wear* 252.11-12 (2002): 992-1000.
- [35] Barkoula, N-M., G. C. Papanicolaou, and J. Karger-Kocsis. "Prediction of the residual tensile strengths of carbon-fiber/epoxy laminates with and without interleaves after solid particle erosion." *Composites science and technology* 62.1 (2002): 121-130.
- [36] Mendoza, JC Mendoza, et al. "Experimental study of temperature erosion tests on bidirectional coated and uncoated composites materials." *Materials Research Express* 7.1 (2020): 015338.
- [37] Sadeghi, Esmail, Nicolaie Markocsan, and Shrikant Joshi. "Advances in Corrosion-Resistant Thermal Spray Coatings for Renewable Energy Power Plants. Part I: Effect of Composition and Microstructure." *Journal of Thermal Spray Technology* (2019): 1-40.
- [38] Davis, Joseph R. *ASM Handbook, Volume 5A: Thermal Spray Technology*. In: Robert C, editor. Materials Park, OH, USA: ASM International; 2013
- [39] Liu, Aiguo, et al. "Arc sprayed erosion-resistant coating for carbon fiber reinforced polymer matrix composite substrates." *Surface and Coatings Technology* 200.9 (2006): 3073-3077.
- [40] Guan hong, Sun, et al. "Parametric study of Al and Al<sub>2</sub>O<sub>3</sub> ceramic coatings deposited by air plasma spray onto polymer substrate." *Applied Surface Science* 257.17 (2011): 7864-7870.
- [41] Ganesan, Amirthan, Motohiro Yamada, and Masahiro Fukumoto. "The effect of CFRP surface treatment on the splat morphology and coating adhesion strength." *Journal of thermal spray technology* 23.1-2 (2014): 236-244.
- [42] Njuhovic, Edin, et al. "Identification of interface failure mechanisms of metallized glass fibre reinforced composites using acoustic emission analysis." *Composites Part B: Engineering* 66 (2014): 443-452.
- [43] Pawlowski, Lech. *The science and engineering of thermal spray coatings*. John Wiley & Sons, 2008.
- [44] P. L. Fauchais, J. V. Heberlein, and M. I. Boulos, *Thermal spray fundamentals: from powder to part*. Springer Science & Business Media, 2014.
- [45] Dykhuizen, R. C., et al. "Impact of high velocity cold spray particles." *Journal of Thermal spray technology* 8.4 (1999): 559-564.

- [46] Assadi, Hamid, et al. "Bonding mechanism in cold gas spraying." *Acta Materialia* 51.15 (2003): 4379-4394.
- [47] T. Schimidt, H. Aassadi, F. Gartner, H. Richter, T. Stolenthoff, and H. Kreye, and T. Klaussen, From Particles Acceleration to Impact and Bonding in Cold Spraying, *J Therm. Spray Technol.*, Vol 18, 2009, p 488-494
- [48] Gonzalez, R., et al. "A review of thermal spray metallization of polymer-based structures." *Journal of Thermal Spray Technology* 25.5 (2016): 897-919.
- [49] Fukumoto, Masahiro, et al. "Deposition of copper fine particle by cold spray process." *Materials transactions* (2009): 0904200749-0904200749.
- [50] Che, Hanqing, Phuong Vo, and Stephen Yue. "Metallization of carbon fiber reinforced polymers by cold spray." *Surface and Coatings Technology* 313 (2017): 236-247.
- [51] Arizmendi-Morquecho, Ana, et al. "Microstructural characterization and wear properties of Fe-based amorphous-crystalline coating deposited by twin wire arc spraying." *Advances in materials science and engineering* 2014 (2014).
- [52] Schneider, Klaus Erich, et al. *Thermal spraying for power generation components*. John Wiley & Sons, 2006.
- [53] P. L. Fauchais, J. V. Heberlein, and M. I. Boulos, *Thermal spray fundamentals: from powder to part*. Springer Science & Business Media, 2014.
- [54] Fukumoto, Masahiro, Min Nie, and Toshiaki Yasui. "Preparation and evaluation of ordinary attritor milled Ti-Al powders and corresponding thermal sprayed coatings." *Materials transactions* 47.7 (2006): 1717-1722.
- [55] Affi, Jon, et al. "Fabrication of aluminum coating onto CFRP substrate by cold spray." *Materials Transactions* (2011): 1108081451-1108081451.
- [56] Hoa, Suong V. *Principles of the manufacturing of composite materials*. DEStech Publications, Inc, 2009.
- [57] "Woven Wire Mesh." <https://www.inoxia.co.uk/products/mesh/sheets/> (accessed May 10, 2019).
- [58] "Vacuum Bagging Equipment and Techniques for Room-Temp Applications." [https://www.fibreglast.com/product/vacuum-bagging-equipment-and-techniques-for-room-temp-applications/Learning\\_Center](https://www.fibreglast.com/product/vacuum-bagging-equipment-and-techniques-for-room-temp-applications/Learning_Center) (accessed April 10, 2019).
- [59] "Vacuum Bagging Equipment and Techniques for Room-Temp Applications." [https://www.fibreglast.com/product/vacuum-bagging-equipment-and-techniques-for-room-temp-applications/Learning\\_Center](https://www.fibreglast.com/product/vacuum-bagging-equipment-and-techniques-for-room-temp-applications/Learning_Center) (accessed April 10, 2019).
- [60] CYCOM® 977-2 AND 977-2A PREPREG <https://www.solvay.com/en/product/cycom-977-2> (accessed August 22, 2020).

- [61] <https://www.oerlikon.com/metco/en/products-services/coating-materials/coating-materials-thermal-spray/>(accessed August 22, 2020).
- [62] "3MB Plasma Spray Gun - Oerlikon Metco." <https://www.oerlikon.com/metco/en/products-services/coating-equipment/thermal-spray/spray-guns/coating-equipment-plasma/3mb/> (accessed August 22, 2020).
- [63] ASTM-G76, "Standard Test Method for Conducting Erosion Tests by Solid Particle Impingement Using Gas Jets." West Conshohocken, PA: ASTM International, 2007, p. 6.
- [64] Bousser, Etienne, L. Martinu, and J. E. Klemberg-Sapieha. "Solid particle erosion mechanisms of protective coatings for aerospace applications." *Surface and Coatings Technology* 257 (2014): 165-181.
- [65] Wiederhorn, S. M., and B. J. Hockey. "Effect of material parameters on the erosion resistance of brittle materials." *Journal of Materials Science* 18.3 (1983): 766-780.
- [66] Fischer-Cripps, Anthony C. "Nanoindentation Test Instruments." *Nanoindentation*. Springer, New York, NY, 2004. 178-194.
- [68] Jönsson, B., and S. Hogmark. "Hardness measurements of thin films." *Thin solid films* 114.3 (1984): 257-269.
- [69] Chicot, D., and J. Lesage. "Absolute hardness of films and coatings." *Thin Solid Films* 254.1-2 (1995): 123-130.
- [70] <https://www.technibond.co.uk/wp-content/uploads/2019/04/surface-energy-chart.pdf> (accessed August 22, 2020).
- [71] Yinglong, Wang. "Friction and wear performances of detonation-gun-and plasma-sprayed ceramic and cermet hard coatings under dry friction." *Wear* 161.1-2 (1993): 69-78.
- [72] Nieto, Andy, et al. "Elevated temperature wear behavior of thermally sprayed WC-Co/nanodiamond composite coatings." *Surface and Coatings Technology* 315 (2017): 283-293.
- [73] C. Verdon, A. Karimi, J.L. Martin, *Mater. Sci. Eng. A* 246 (1e2) (1998) 11.
- [74] P. Fauchais, A. Vardelle, B. Dussoubs, Quo vadis thermal spraying *J. Therm. Spray Technol.* 10 (2001) 44–66.
- [75] Bhat, H., and H. Herman. "Plasma-spray-quenched martensitic stainless steel coatings." *Thin Solid Films* 95.3 (1982): 227-235.
- [76] Olivio, Émillyn Ferreira Trevisani, et al. "Analysis of 410NiMo coating deposited by thermal spray in CA6NM martensitic stainless steel against erosion by cavitation." *The International Journal of Advanced Manufacturing Technology* 104.9-12 (2019): 4559-4569.

- [77] Sarikaya, Ozkan. "Effect of some parameters on microstructure and hardness of alumina coatings prepared by the air plasma spraying process." *Surface and Coatings Technology* 190.2-3 (2005): 388-393.
- [78] Bolelli, Giovanni, et al. "Wear behaviour of thermally sprayed ceramic oxide coatings." *Wear* 261.11-12 (2006): 1298-1315.
- [79] Geng, Zhe, et al. "Tribological behaviour of low-pressure plasma sprayed WC-Co coatings at elevated temperatures." *Industrial Lubrication and Tribology* (2019).
- [80] Branco, José Roberto Tavares, et al. "Solid particle erosion of plasma sprayed ceramic coatings." *Materials Research* 7.1 (2004): 147-153.
- [81] Wentzel, Eduard John, and C. Allen. "Erosion-corrosion resistance of tungsten carbide hard metals with different binder compositions." *Wear* 181 (1995): 63-69.
- [82] Santacruz, G., et al. "Experimental analysis of jet slurry erosion on martensitic stainless steel." *IOP Conference Series: Materials Science and Engineering*. Vol. 659. No. 1. IOP Publishing, 2019.
- [83] Fervel, V., B. Normand, and C. Coddet. "Tribological behavior of plasma sprayed Al<sub>2</sub>O<sub>3</sub>-based cermet coatings." *Wear* 230.1 (1999): 70-77.
- [84] Yin, Zhijian, et al. "Particle in-flight behavior and its influence on the microstructure and mechanical properties of plasma-sprayed Al<sub>2</sub>O<sub>3</sub> coatings." *Journal of the European Ceramic Society* 28.6 (2008): 1143-1148.
- [85] S. C. J. Li, W. Z. Wang, *Materials Science and Engineering A* 386, 10 (2004).
- [86] Li, Chang-Jiu, Guan-Jun Yang, and Akira Ohmori. "Relationship between particle erosion and lamellar microstructure for plasma-sprayed alumina coatings." *Wear* 260.11-12 (2006): 1166-1172.
- [87] Nicholls, J. R., M. J. Deakin, and D. S. Rickerby. "A comparison between the erosion behaviour of thermal spray and electron beam physical vapour deposition thermal barrier coatings." *Wear* 233 (1999): 352-361.

- [88] Guo, D. Z., and L. J. Wang. "Study of fracture and erosive wear of plasma sprayed coatings." *Journal of Thermal Spray Technology* 2.3 (1993): 257-263.
- [89] Arjula, Suresh, A. P. Harsha, and M. K. Ghosh. "Erosive wear of unidirectional carbon fiber reinforced polyetherimide composite." *Materials letters* 62.17-18 (2008): 3246-3249.
- [90] Cai, Feng, et al. "Solid particle erosion behaviors of carbon-fiber epoxy composite and pure titanium." *Journal of Materials Engineering and Performance* 25.1 (2016): 290-296.
- [91] Aquaro, Donato. "Erosion due to the impact of solid particles of materials resistant at high temperature." *Meccanica* 41.5 (2006): 539-551.
- [92] Savinykh, A. S., et al. "The influence of the cobalt content on the strength properties of tungsten carbide ceramics under dynamic loads." *Technical Physics* 63.3 (2018): 357-362.
- [93] Bitter, J. G. A. "A study of erosion phenomena: Part II." *Wear* 6.3 (1963): 169-190.
- [94] ASTM C 633 "Standard Test Method for Adhesion or Cohesion Strength of Thermal Spray Coatings" ASTM International, March 2001
- [95] Lima, C. R. C., and R-E. Trevisan. "Graded plasma spraying of premixed metalceramic powders on metallic substrates." *Journal of thermal spray technology* 6.2 (1997): 199-204.
- [96] Khan, A. Nusair, J. Lu, and H. Liao. "Effect of residual stresses on air plasma sprayed thermal barrier coatings." *Surface and Coatings Technology* 168.2-3 (2003): 291-299.
- [97] Mishra, S. C., et al. "Microstructure, Adhesion, and Erosion Wear of Plasma Sprayed Alumina–Titania Composite Coatings." (2008)